Studies on Electron Beam Vapor Generation in PVD Processes

By

BISWARANJAN DIKSHIT

(Enrollment No:- ENGG01200704030)

Bhabha Atomic Research Centre, Mumbai – 400 085 INDIA

A thesis submitted to the Board of Studies in Engineering Sciences

In partial fulfillment of requirements

For the Degree of

DOCTOR OF PHILOSOPHY

of

HOMI BHABHA NATIONAL INSTITUTE, MUMBAI

March, 2010

Homi Bhabha National Institute

Recommendations of the Viva Voce Board

As members of the Viva Voce Board, we certify that we have read the dissertation prepared by Biswaranjan Dikshit entitled "Studies on Electron Beam Vapor Generation in PVD Processes" and recommend that it may be accepted as fulfilling the dissertation requirement for the Degree of Doctor of Philosophy.

	Date: 2nd February, 2011	
Chairman:	**Prof. A. P. Tiwari**	
	Date: 2nd February, 2011	
Guide / Convener:	**Prof. M. S. Bhatia**	
	Date: 2nd February, 2011	
Member 1:	**Prof. K. V. Nagesh**	
	Date: 2nd February, 2011	
Member 2:	**Prof. D. N. Badodkar**	
	Date: 2nd February, 2011	
Examiner:	**Prof. Harishankar Ramachandran**	
	Date: 2nd February, 2011	
	(PROF. KALLOL ROY)	

Final approval and acceptance of this dissertation is contingent upon the candidate's submission of the final copies of the dissertation to HBNI.

I hereby certify that I have read this dissertation prepared under my direction and recommend that it may be accepted as fulfilling the dissertation requirement.

Date: 2nd February, 2011

Place: Mumbai

Guide: Prof. M. S. Bhatia

STATEMENT BY AUTHOR

This dissertation has been submitted in partial fulfillment of requirements for an advanced degree at Homi Bhabha National Institute (HBNI) and is deposited in the Library to be made available to borrowers under rules of the HBNI.

Brief quotations from this dissertation are allowable without special permission, provided that accurate acknowledgement of source is made. Requests for permission for extended quotation from or reproduction of this manuscript in whole or in part may be granted by the Competent Authority of HBNI when in his or her judgment the proposed use of the material is in the interests of scholarship. In all other instances, however, permission must be obtained from the author.

Biswaranjan Dikshit

DECLARATION

I hereby declare that the investigation presented in the thesis has been carried out by me. The work is original and has not been submitted earlier as a whole or in part for a degree/diploma at this or any other Institution / University.

Biswaranjan Dikshit

Biswaranjan Dikshit

DEDICATIONS

I dedicate this thesis to my Mother

Mrs. Shantilata Dikshit

ACKNOWLEDGEMENTS

I would like to express my deep sense of gratitude towards my guide Dr M S Bhatia for his valuable guidance, keen interest and encouragement during the course of this work. I am extremely grateful to Dr A P Tiwari, Dr S V G Ravindranath and Dr K V Nagesh for their constant encouragement and fruitful discussions during this work. I am indebted to Dr B M Suri, Dr V K Mago, Dr A K Das and Dr L M Gantayet for their support and detailed discussions on various aspects of the process.

My sincere thanks to my colleagues Mr G K Sahu, Mr G R Zende, Mr R C Das, Mr M L Shah, Mr A K Pulhani, Mr A Majumder, Dr Shailesh Kumar and Dr Vas Dev for their valuable suggestions and cooperation during the experiments and subsequent analysis.

I am grateful to my father Mr Ramesh Chandra Dikshit, mother Mrs Shantilata Dikshit, brothers (Mr Binaya Bhusana Dikshit and Mr Bijaya Ketan Dikshit), sisters (Mrs Shradhanjali Dikshit, Mrs. Sasmita Dikshit and Mrs. Subhalaxmi Dikshit), father-in-law, mother-in-law, brothers-in-law and sisters-in-law for their moral support and numerous blessings. I thank my wife (Mrs Madhumita Dikshit) and sons (Mr Jyoti Prakash Dikshit and Mr Ashutosh Dikshit) for the inspiration they provided.

Biswaranjan Dikshit

TABLE OF CONTENTS

LIST OF ABREVIATIONS

e-beam	-	Electron beam
e-gun	-	Electron gun
CEF	-	Concentrated energy flux
PVD	-	Physical vapor deposition
HVPS	-	High voltage power supply
SCP	-	Single color pyrometer
TCP	-	Two color pyrometer
PMT	-	Photo multiplier tube
HCDL	-	Hollow cathode discharge lamp

ABSTRACT

Generation of metal vapor by e-beam heating is a complex phenomenon that involves many linear, as well as non-linear physical and dynamical processes in response to the incidence of concentrated flux of energetic electrons on the target. These processes occurring at different stages need to be understood in details for optimization of the process and also for suitable tailoring for specific end uses. Working in this direction, detailed investigations were carried out on important aspects of the e-beam evaporation process. The electron optics as affected by bending of e-beam and geometrical errors of the magnetic lens, stability and controllability of electron emission current, process monitoring, convective heat transfer in melt pool on the target and physical processes occurring in the metal vapor and accompanying plasma emerging from the hot zone have been examined in detail.

For a realistic assessment of electron optics in e-gun used for evaporation, numerical simulation of the electron trajectories was carried out starting from the anode exit hole up-to the metal target placed in a water cooled crucible. As e-beam used for evaporation is generally bent by 45^0 to 270^0 to avoid transgress of vapor/ions into the cathode/anode region, the shape and size of the e-beam spot on the target deteriorate. In addition to this, presence of possible angular/positional misalignment of the e-beam axis with the axis of the focusing magnetic lens affects the characteristics of the e-beam power distribution. The dependence of the compactness, circular symmetry and shift of the e-beam spot from the expected position on the target are quantified in terms of above parameters and dominant factors are identified. Finally, a novel scheme for ideal distortion-less focusing of a bent non-paraxial e-beam is analytically derived. It was proved that the effect of bending on the size and shape of e-beam spot on the target can be completely eliminated (*theoretically made zero*) by choosing a radially decreasing magnetic field and also a *circularly asymmetric* radial velocity distribution for the beam electrons. In the paraxial case, elimination of the distortion due to bending is

possible by using a radially decreasing magnetic field and circularly symmetric radial velocity distribution, which is easily achieved by a coaxial thin magnetic lens. These conclusions are shown to be valid for any angle of bending of e-beam and are relativistically correct. Extension of this principle for ideal focusing of circulating charged particles in betatron type accelerators where kinetic energy gradually increases during the motion is also derived.

Investigations on the stability of the electron emission current was taken up next, which is a desirable feature in e-guns used for evaporation of metals. However, a region of instability (hysteresis in electron emission current) was observed. It was noted that in the forward direction of power change, the required filament-heating current for a specified e-beam current was significantly higher than the filament current required in the backward direction. By use of theoretical calculations and experimental validations, it was established that this hysteresis arises due to energetic metal ion bombardment on the electron-emitting area of filament in e-gun. A practical way to check this uncontrollability arising due to bombardment of ions is presented. In addition to this, ways for minimizing repeated electrical discharges occurring in e-guns and precautions to be taken for protection of the HVPS from transient over voltages/currents are also discussed.

One of the important process monitoring parameters in the e-beam evaporation is the temperature of hot zone created by impact of high power e-beam. Direct line of sight viewing of the hot zone for temperature measurement using an optical pyrometer on a continuous basis is ruled out in e-beam evaporators due to opacity introduced by coating of the vacuum windows within a short time span. Continuous visual monitoring conventionally relies on a periscopic arrangement that makes use of a process generated thin film mirror formed by deposition of evaporating metal atoms. However, it was found that this method introduces significant error in temperature as measured by optical pyrometer. The dominant factors viz. temperature and reactivity of evaporant metal which affect the measurement were

experimentally examined. A solution that bypasses this problem was proposed and it was shown through calculations that this novel method avoids errors associated with the periscopic method and yet extends the continuous monitoring time by a factor of ~1000 from few seconds to few hours. Finally our results on the measurement of other important parameters viz.. atomic vapor flux and (atomic) state resolved atom densities by use of piezoelectric sensor and spectroscopic absorption method respectively are presented.

During vacuum evaporation of metals by use of a concentrated energy flux such as e-beam, a liquid metal pool with a steep temperature gradient is formed around the hot zone. Due to temperature dependence of surface tension as well as density and depression of the evaporating surface caused by back-pressure of the emitted vapor in this molten pool, strong convective flow sets in the molten pool. It was proposed for the first time that this convection passes through three different stages as e-beam power is increased. This was experimentally confirmed by quantifying convective heat transfer in terms of dimensionless Nusselt number and by studying its evolution with power in experiments using aluminum, copper and zirconium as targets. Experimental values of Nusselt number were compared with the theoretically predicted values by earlier researchers to test the validity of assumptions made and to know the type of flow in the melt pool. Thus, conclusions about the evolution of convective heat transfer and physical characteristics of flow in the molten pool could be drawn by considering the roles of surface tension and depression on the evaporating surface.

In a few applications such as atomic vapor laser isotope separation, excitation temperature of the e-beam generated metal vapor needs to be known. As the excitation temperature may depart significantly from the equilibrium value, we have experimentally measured it in uranium vapor generated by e-beam heating. To understand the various processes affecting it, quantitative expressions were derived to estimate the effect of atom-atom and electron-atom collisions on the excitation temperature at different source

temperatures. This was compared with the experimental data recorded by spectroscopic absorption technique using a HCDL. It was concluded from analysis of experimental data that relaxation of the metastable atoms by collisions with low-energy plasma electrons was so large that it lowers the excitation temperature below the translational temperature of the vapor. So, with increase in atom density, frequent atom-atom collisions were expected to establish equilibrium between the excitation and translational temperatures resulting in increase of the excitation temperature (i.e. heating of vapor). From the observed excitation temperature at low e-beam power, total de-excitation cross section for relaxation of uranium atoms in 620 cm^{-1} state by interaction with low energy electrons was estimated to be ~10^{-14} cm^2. Finally using this value of cross section, extent of excitational cooling/heating by electron-atom and atom-atom collisions were estimated at higher e-beam powers.

During e-beam evaporation of metals, the generated atomic vapor is partially ionized due to Saha ionization and electron impact ionization that occurs by impact of the primary, backscattered and secondary electrons with the atomic vapor near the hot zone. Total ionization content of the vapor is generally in the range of ~0.2-0.5%. Thus, generation of plasma during e-beam evaporation of metals is an inherent phenomenon of the vapor generation process. The above-mentioned plasma is however a non-equilibrium one consisting of two different groups of electrons depending upon their origin (atom-atom or electron-atom collisions) and these groups are characterized by different energy spread or temperature. While this plasma expands with the metal vapor, thermodynamic equilibrium between these two groups of electrons is gradually established by electron-electron coulomb collisions and electron-atom inelastic collisions. Evolution of this two-temperature plasma was experimentally investigated by a disc type Langmuir probe during e-beam evaporation of zirconium. The method of interpretation of the V-I characteristics of the Langmuir probe for diagnostics of a *two-temperature plasma* is given in detail along with justification.

Mathematical expressions for the effect of different interactions on the evolution of electron temperatures of the plasma were derived and applied to our experimental situation. Taking the initial temperature of the plasma at the source of vapor, total cross section for electron-atom inelastic collisions was calculated, the order of which agreed well with the reported values. Thus, contribution of each type of interaction (electron-electron and electron-atom) on the cooling of high temperature group of electrons in plasma were quantified.

To summarize, important stages in the e-beam vapor generation process have been studied in this work starting from e-beam generation to the thermo-physical processes occurring in the atomic vapor. In many cases, novel propositions along with experimental or theoretical proof have been made for better understanding of the phenomena with an eye to solve the difficulties encountered in the process.

List of Figures

LIST OF TABLES

List of Publications

INTERNATIONAL JOURNALS

1. "Ideal distortion-less bending of a focused non-paraxial electron beam",
   Biswaranjan Dikshit and M. S. Bhatia
   Nuclear Instruments and Methods in Physics Research A 596, (2008) 300–304
2. "Hysteresis in electron-emission current of an axial electron gun used for evaporation of metals",
   Biswaranjan Dikshit and M. S. Bhatia
   IEEE transactions on Plasma Science, 35 (2), (2007) 396-401
3. "Effect of periscope reflecting mirror on uncertainty of measured temperature of an electron beam heated metal vapor source",
   B. Dikshit, G. R. Zende, M. S. Bhatia and B. M. Suri
   Measurement Science & Technology, 19 (2008) 511 – 516
4. "Convection in molten pool created by a concentrated energy flux on a solid metal target"
   B. Dikshit, G. R. Zende, M. S. Bhatia and B. M. Suri
   Physics of Fluids, 21, 084105 (2009)
5. "Collisional effects on metastable atom population in vapour generated by electron beam heating",
   B. Dikshit, A. Mazumder, M. S. Bhatia and V. K .Mago
   Journal of Physics D: Applied Physics, 41 (2008) 521 – 526
6. "Evolution of a two-temperature plasma expanding with metal vapor generated by electron beam heating",
   B. Dikshit, G. R. Zende, M. S. Bhatia and B. M. Suri
   IEEE transactions on Plasma Science, 37 (7), (2009) 1196-1202

7. "A Novel 270-degree Bent-Axial-Type Electron Gun and Positioning of Its Electron Beam Spot on the Target"

   Biswaranjan Dikshit and M. S. Bhatia

   IEEE Transactions on Electron Devices, 57 (4), (2010) 939-945

SYMPOSIUM

1. "Use of Langmuir probe for analysis of charged particles in metal vapour generated by electron beam heating",

   B Dikshit and M. S. Bhatia,

   International symposium on Vacuum Science and Technology, Nov 28-30, 2007,

   TIFR, Mumbai

   (also published in Journal of Physics: Conference series. **114,** 012030, 2008)

CHAPTER – 1

INTRODUCTION

1.1 General Considerations:

High power e-guns [1] with power ranging from 3 kW to 500 kW have found wide applications in research and industrial units especially in PVD systems. PVD is used for production of semiconductor devices, optical components, wear resistant hard coated cutting tools, thermal and chemical barrier coatings. Some other applications such as isotope separation in nuclear industry [2] also make use of PVD like conditions. The coating method involves physical processes such as high temperature vacuum evaporation by resistive or electron beam heating (EBPVD) or plasma sputter deposition. As compared to the sputter deposition, EBPVD offers high purity, structural and morphological control of films, very high range of deposition rate from 1 nm per minute to few micrometers per minute and also permits use of large substrates for coating. In this e-beam vapor generation process, it is possible to create temperatures in excess of 3000^0C in a small zone on the target which is sufficient to evaporate metals with high boiling point and even refractory materials at high thermal and material utilization efficiencies. As the metal target is placed in a water-cooled crucible and molten evaporating zone at the center of the target is contained with its own cooler skull, chemical reactivity problem between target material and crucible is averted and this results in purer deposits. E-beam vapor generation process has also recently found a major application in nuclear industry as high rate evaporation of reactive materials in vacuum is required for isotope separation process.

1.2 Basic Processes:

In e-guns used for vapor generation, the chamber is evacuated to a pressure of 10^{-5} mbar by an oil diffusion pump or turbo molecular pump backed by rotary pump. Electron emission occurs from a hot filament cathode made up of tantalum or tungsten by thermionic emission. The maximum value of electron emission current density from the filament is given by Richardson-Dushman equation,

$$J = AT^2 \, e^{-e\phi/kT} \qquad (1)$$

where, e = Electronic charge

A= Richardson constant of cathode material

ϕ = Work function of cathode material

k = Boltzmann constant

T = Absolute temperature of cathode

The filament is heated by passage of current in the range of 50 to 80A while keeping it at a negative bias of -10kV to -60kV. For high power guns, temperature limited mode of operation is used so that beam current can be easily controlled by varying the temperature of the filament. Electrons bombard the target with energy ~ 10-60 keV after escaping through the anode exit hole followed by passage through a focusing field. Very high power density (~ 20kW/cm^2) is attained on the target by tightly focusing the e-beam using magnetic lenses. Depending upon the focusing scheme, the e-gun can be axial type or transverse type as shown in Fig. 1. In axial e-gun, focusing is carried out by using a coaxial magnetic coil after the anode exit hole which makes the beam converging. In transverse e-gun, focusing is attained by applying a uniform transverse magnetic field and the beam is focused along one dimension after 90^0 or 270^0 rotation. Owing to high power density in these e-guns, vaporization of metals with high boiling point is possible. Temperature of a small zone on the surface of approximately the size of the e-beam spot rises to very high value (~3000^0C) leading to evaporation of the target material. The emerging vapor from the target is then collimated by

slits and deposited on substrates. In case of nuclear applications, a specific isotope in the atomic vapor can be selectively ionized by passing lasers of appropriate wavelength through this vapor and then collected on a plate maintained at negative potential. In coating applications, the substrate for deposition is normally kept hot so that the condensed atoms have enough kinetic energy and therefore surface mobility to jump across atomic steps and reach positions of a lower potential energy resulting in dense films along with good adhesive properties. The mechanism of formation of thin films can be understood as follows. At first the nucleation of single atoms on the surface occurs. If the time of atom migration on the surface is great enough to meet another atom before being re-evaporated these atoms coalesce to form an island. As the energy required for evaporation of one of the atoms of this pair is considerably higher than that needed for an isolated atom, stable islands (nuclei) begin to form on the surface. These islands coalesce and finally the continuous growth of the film takes place.

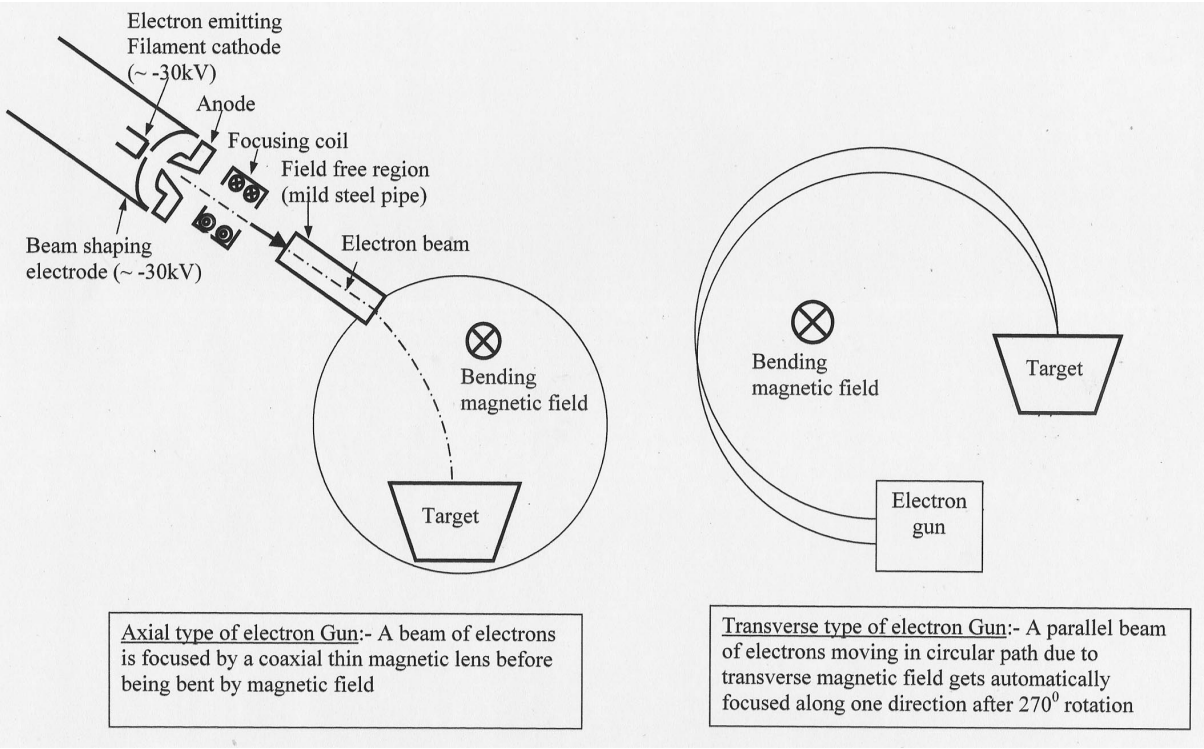

Figure 1 Types of electron gun – Axial type and Transverse type

1.3 Literature update and Directions:

In e-beam evaporation systems, the e-gun is so placed that it does not lye along the line-of-sight from vapor emitting zone (i.e. it is kept in geometrical shadow of the vapor source). This is done to avoid entry of metal vapor and ions (created by Saha ionization and electron impact ionization [3]) towards the cathode-anode region of the e-gun causing electrical discharges [1] or instabilities [4] or unwanted coatings on the high voltage components. Thus, bending of the e-beam becomes an absolute necessity. Care is also taken so that the beam hits the target at an angle of incidence of ~ 90^0 to ensure minimal backscattered e-beam power [1]. As the energy of electrons varies from few tens to ~80 keV and background pressure deteriorates by the generated vapor, bending and beam shaping within the vapor by electric field is not possible due to possibility of electrical discharges. Hence, bending of e-beam immersed in vapor is carried out by application of an external magnetic field after the focusing coil. This bending of e-beam however distorts the shape of the e-beam spot on the target. In addition to this, if there is an angular misalignment of the focusing coil axis with the axis of beam or if there is a positional offset between focus coil and e-beam in the case of axial e-gun, the spot quality (compactness, circular symmetry and position) on the target is affected. Further, as the focusing coil of the e-beam works on the principle of thin magnetic lens, finite size of the cross section of focusing coil also affects the compactness of e-beam spot. Considering the knowledgebase available in literature on electron optics [5-7], a detailed analysis of the above important aspect was carried out and possible solutions were explored, which are covered in chapter 2.

Very little work exists in literature on stability and controllability of e-beam evaporators, which are necessary to ensure quality of deposits in PVD plants as rate of deposition affects the morphology and surface texture. In our experiments, it was observed that some amount of instability in the form of hysteresis resulting in uncontrollability of the e-

beam existed in e-guns used for evaporation (especially in axial e-guns). Detailed quantitative analysis of this instability is not reported in the literature till date. Working towards the understanding of above phenomena and to find an appropriate solution, experiments along with detailed calculations were carried out in an indigenous 8kW axial e-gun. Identification of the dominant process responsible for the hysteresis effect out of various possibilities like deposition of kinetic energy of the ions on filament, secondary electron emission, field emission due to presence of ion cloud [8] and I^2R heating by extra current flowing through the filament for neutralization of impinging ions [8] was carried out. In addition to this, ways for minimizing repeated electrical discharges occurring in the electron guns used for evaporation of metals are identified and precautions to be taken for protection of the high voltage power supply from transient over voltages/currents are discussed. All these aspects are summarized in chapter 3.

Process monitoring is necessary in PVD to ensure that process parameters are maintained at the desired levels. Primary interest is in the vapor throughput, which depends upon the surface temperature of the vapor-emitting zone. So, it is desirable to keep the surface temperature of the hot zone at a predetermined value so as to ensure constant atomic vapor flux, high evaporation efficiency and also for ensuring process safety. Temperature is thus an extremely important process parameter which needs to be monitored on a continuous basis. This is usually done via non-contact optical radiation pyrometry by using a SCP or TCP. However, direct line of sight viewing of the hot zone for temperature measurement using an optical pyrometer on a continuous basis is ruled out due to opacity introduced by rapid coating of the vacuum windows within a short time span. Hence, continuous visual monitoring conventionally relies on a periscopic arrangement that makes use of a process generated thin film mirror formed by deposition of evaporating metal atoms [9-12, 2]. It was however learnt through our experiments that this method introduces significant error in the

temperature measured by optical pyrometer due to wavelength dependant reflectivity of the metal thin film mirror. To solve the above problem, alternative solutions are explored. Our studies in these areas are summarized in chapter 4. Our results on the measurement of the other important process parameters viz. atomic vapor flux and state sensitive densities by use of piezoelectric sensor and spectroscopic absorption method respectively are also presented.

Efficiency of the electron beam evaporation process at a specific e-beam power depends upon the maximum temperature created at the e-beam impact point on the metal target. However, as soon as the temperature of the target center exceeds the melting point of material, a molten pool is formed and in this liquid region, heat is transferred out from the e-beam spot by both convection and conduction. This increased heat transfer in the melt pool makes it difficult to maintain a steep temperature gradient in it. At higher beam power, this convective heat transfer becomes so dominant that we see an approach towards saturation in the temperature of e-beam spot with power [11]. Thus, convective heat transfer in the liquid metal pool created by the concentrated energy flux (CEF) needs to be understood for efficient design of the vapor source. The convection in the molten pool can be caused by surface tension (thermo-capillary) or gravity forces or both. To quantify the above convective heat transfer in terms of dimensionless Nusselt number, Karcher et al [13] have recently reported their results on turbulent flow in liquid iron at very high Marangoni numbers (~10^8). However, they have not reported the evolution of the convective heat transfer with e-beam power when flow inside the molten pool gradually gets converted from laminar to turbulent. In another report, theoretical work by Pumir et al [14] have led to expressions for Nusselt number both in laminar and turbulent regime, but of course with some simplifying assumptions such as the fluid surface being taken as perfectly flat. They have emphasized the need for experimental verification to test the validity of their assumptions. All these investigators [13-14] have not taken into consideration the *curvature of the evaporating*

surface caused by back-pressure of the emitted vapor from the hot zone. In our studies, we have included the effect of deformation of the evaporating surface and tried to understand the evolution of convection in melt pool as a function of e-beam power. Our results and inferences are detailed in chapter 5.

Although, in applications of e-beam evaporators related to thin films and coatings, knowledge of evaporation rate is sufficient, in other applications such as atomic vapor laser isotope separation [15-17] and atomic spectroscopy, knowledge of distribution of atomic populations in metastable states also becomes important as the wavelengths of the lasers need to be set accordingly for efficient photo-ionization of the vapor. The e-beam route to vapor generation presents an interesting situation where metastable atom population after free expansion of vapor can differ substantially from the thermal equilibrium value near the source due to the possibility of electron-atom and atom-atom collisions during propagation. This calls for experimental measurements which can be undertaken by using spectroscopic techniques such as atomic absorption or atomic fluorescence. Recent investigations of atom populations in e-beam generated Gd vapor have revealed substantially lower excitation temperature [18-19] (one fourth to one fifth of the surface temperature of e-beam spot). Similar results were reported for Nd metal by Chen [20] et al who have suggested that electron-atom relaxation by low energy electrons was more important than the atom-atom collisional relaxation for lower excitation temperature observed in their experiments. In our work, experimental observations and analysis of the dynamics of low-lying metastable atom populations in e-beam generated uranium vapor due to electron-atom and atom-atom interactions at different e-beam powers (or source temperatures) are presented. Spectroscopic absorption technique was utilized in our work for the measurement of state resolved atom densities (620 cm^{-1} and 0 cm^{-1}states) in the vapor column with a HCDL as an optical source. Measurements were carried out over a range of e-beam powers to ascertain the nature

(cooling or heating) and the relative extent of de-excitation/excitation of atoms by electron-atom and atom-atom collisions. Our work in this area is summarized in chapter 6.

Chapter 7 is devoted to studies of plasma accompanying vapor generation by e-beam heating. During e-beam evaporation of metals, the generated atomic vapor is partially ionized due to Saha ionization and electron impact ionization that occurs via collisions of the primary, backscattered and secondary electrons with the atomic vapor near the hot zone. Total ionization content of the vapor is normally of the order of ~0.2-0.5% [3, 18] though it could exceed ~1% in some cases. Thus, the generation of plasma during e-beam evaporation of metals is an inherent phenomenon of the vapor generation process. The above-mentioned plasma is however a non-equilibrium one which consists of two different groups of electrons depending upon their origin (atom-atom collisions or electron impact) and these groups are characterized by different energy spread or temperature. While this plasma expands along with the metal vapor, thermodynamic equilibrium between these two groups of electrons is gradually established by electron-electron coulomb collisions and electron-atom inelastic collisions. In this regard, Besuelle et al [21] have reported the observation of two groups of electrons in the plasma generated during e-beam heating (indicated by two slopes below plasma potential). However, they have not quantitatively studied the process of establishment of equilibrium between these two groups in the plasma. Many researchers [22-26] have investigated the two-temperature plasmas in other applications, but only by theory or numerical analysis.

In this work, we first experimentally investigate the process of attainment of thermodynamic equilibrium between the two groups of electrons in plasma generated by e-beam evaporation of Zirconium using a disc type Langmuir probe. The method of interpretation of the V-I characteristics of the Langmuir probe for diagnostics of a *two-temperature plasma* is given in detail along with the justification. Then, mathematical

expressions for the effect of different interactions on the evolution of electron temperatures of the plasma are derived and applied to our experimental observations. Taking the initial temperature of the plasma at the source of vapor, total cross section for electron-atom inelastic collisions is calculated and compared with the reported values. Finally, contributions of each type of interaction (electron-electron and electron-atom) on the cooling of high temperature group of electrons in plasma are quantified.

Above mentioned phenomena in the e-beam vapor generation process are explained in details in the following sections. In many cases, novel propositions are made along with experimental or theoretical justifications for improved understanding of the phenomena and also for providing solutions to the difficulties encountered in the process.

CHAPTER - 2

Electron optics in e-beam evaporation systems

2.1 Quality of e-beam spot

– dependence on bending and geometrical errors

As described earlier, an e-beam that is intended for use in evaporation of metals needs bending before hitting the target so as to keep the cathode-anode assembly in geometrical shadow region of the vapor. However, this bending distorts the shape of the e-beam spot on the target especially in case of axial e-gun where circular beam spot is expected. In addition to this, presence of a small angular misalignment of the focusing coil axis with the axis of beam or a positional offset between focus coil and e-beam degrades the e-beam spot qualities i.e. compactness, circular symmetry and position on the target. As the focusing action of the e-beam is based on the principle of thin magnetic lens, finite size of the cross section of the focusing coil may also affect the compactness of e-beam spot on the target. For study of the above effects, numerical modeling of the e-beam trajectory in a realistic spatially varying magnetic field was carried out for different non-ideal situations such as angular misalignment, positional offset, finite size of focus coil and bending of e-beam through a specified angle before hitting the target. In the above calculation, we have neglected the effect of space charge, as the required beam diameter for PVD applications is much more than the minimum possible diameter limited by space charge, which is quantitatively proved in section 2.2.

The geometry of the simulation is given in figure 2.1. As depicted in the figure, a parallel e-beam emerging from anode hole of a Pierce type e-gun is focused by a thin magnetic lens (or current carrying coil). There is an angle ‘δ’ between the axis of the beam and that of the magnetic lens. The center of the lens is also shifted vertically by a distance of *‘d’*. After passing through the focusing region it goes through the field free region of length L_2 and finally is bent by a uniform magnetic field before hitting the target. The strength of the

bending magnetic field is so chosen that electrons at the central axis of the beam hit the target at 90^0 incidence. The desired point of hitting is the centre of the target surface. The equations of motion of the electron in the spatially varying magnetic field are given by,

$$\begin{aligned}
\frac{d^2x}{dt^2} &= \frac{q}{m}\left(B_z\frac{dy}{dt} - B_y\frac{dz}{dt}\right) \\
\frac{d^2y}{dt^2} &= \frac{q}{m}\left(B_x\frac{dz}{dt} - B_z\frac{dx}{dt}\right) \\
\frac{d^2z}{dt^2} &= \frac{q}{m}\left(B_y\frac{dx}{dt} - B_x\frac{dy}{dt}\right)
\end{aligned} \tag{2.1}$$

Where q= charge of electron (-1.6×10^{-19} C) and m = mass of electron (9.1×10^{-31}kg)

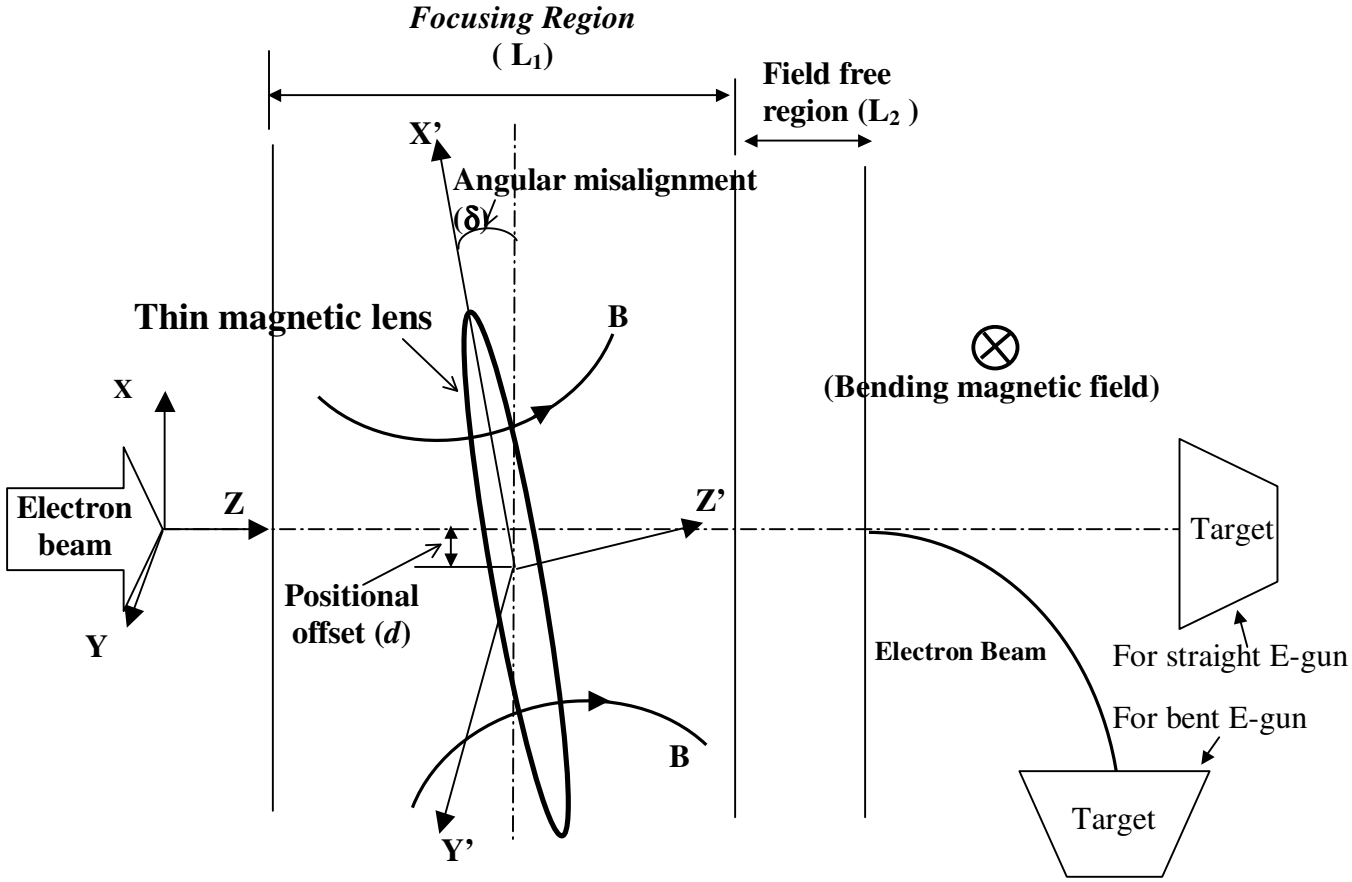

Figure 2.1 Geometry considered for simulation of e-beam spot on target

Above differential equations were numerically solved by using fourth order Runge-Kutte method and the program was written in 'C' language. The radial and axial focusing magnetic fields due to current carrying loop at any point ($r' \phi' z'$) in the frame of reference X'Y'Z' of the loop were calculated by,

$$B_{r'} = \frac{B_0 R^2 z'}{2\pi} \int_0^{2\pi} \frac{\cos\phi'}{\left(R^2 + r'^2 + z'^2 - 2Rr'\cos\phi'\right)^{3/2}} d\phi'$$

$$B_{z'} = \frac{B_0 R^2}{2\pi} \int_0^{2\pi} \frac{(\mathrm{R} - \mathrm{r}'\cos\phi')}{\left(R^2 + r'^2 + z'^2 - 2Rr'\cos\phi'\right)^{3/2}} d\phi' \qquad (2.2)$$

Where B_0= Magnetic field at the centre of wire loop

R= Radius of the current carrying wire loop

Above components of magnetic field were transformed into the components in the XYZ frame for use in Eq. (2.1) by appropriate coordinate transformation rules. Time step was taken to be 10^{-12} sec and total time of travel for electron was ~5 nano-seconds. By reducing the time step, change in results were found to be negligible (< 1%) and so, all the results were produced with time step of 10^{-12} sec. Finally, to test the effect of finite size of the coil on the compactness of e-beam spot, simulation of e-beam trajectory was carried out assuming the coil to consist of 49 conductors uniformly distributed in the cross section of coil (Coil radius=50mm and cross section is of square shape with thickness=25mm).

Figure 2.2 shows the movement of the e-beam spot about center of the target (0,0) with gradual increase in focusing magnetic field 'B' in case of only angular misalignment of ~5^0 of the axis of focus coil with respect to e-beam axis. Figure 2.3 shows the e-beam spot at different focusing magnetic fields in case of only positional offset of 10mm of the focus coil along-X-axis with respect to e-beam. Figure 2.4 gives the position and shape of e-beam spot on the target for the case when all the affecting parameters such as 90^0 bending of beam, 5^0 angular misalignment and 10mm positional offset of focus coil exist. It is clear in Fig. 2.4 that

the shift along X-axis due to angular misalignment is neutralized by opposite shift of positional offset as evident in Figs. 2.2 and 2.3. Figure 2.5 gives the position and shape of e-beam spot on the target for the case when all the conditions are same as in Fig. 2.4 except that the tilt of focus coil is in opposite direction. In this case of Fig.2.5 also, the beam is pulled towards X-axis due to opposing effects of angular misalignment and positional offset.

Radial shift of the e-beam spot with varying current in focusing coil is given in Fig. 2.6. It was found that the beam spot was significantly far away from the desired center of target in case of geometrical misalignment of the focus coil. To quantify the size and shape of e-beam spot on the target, an ellipse was fitted to the outermost electrons. Area of the spot is given by 'πab' where a is half major axis and b is half minor axis of ellipse. Shape (circular symmetry) of the spot is given by eccentricity, $e = b/a$. Area and circular symmetry of the e-beam spot calculated in this manner at varying focusing field are given in Fig.2.7 and 2.8 respectively. It is seen that although the area of e-beam spot for a bent beam is less, it is highly asymmetric which is undesirable in many e-beam evaporation and welding applications. Another point to be noted here is that the effect of finite size of the focus coil on the e-beam spot area is not significant. The reason for the spot area not becoming zero even for the case of thin coil without any geometrical errors is spherical aberration which focuses the peripheral electrons nearer to the magnetic lens as compared to the electrons close to central axis of beam. Effect of chromatic aberration does not appear here as we have taken all the electrons to be mono-energetic.

Finally, to quantify the compactness of e-beam spot, we have used the standard deviation of the electrons from the center of gravity (mean position) of spot on target as used by other researchers [27]. The standard deviation is a better parameter to indicate the compactness as the area cannot discriminate between a point and a straight line, as both have

zero area. Mathematically, if the target plane is considered as XY-plane, standard deviation σ of e-beam spot is given by,

$$\sigma = \sqrt{\frac{1}{n}\sum_{i=1}^{n}\left(x_i - x_0\right)^2 + \left(y_i - y_0\right)^2} \tag{2.3}$$

Where n = Total number of electrons considered,

(x_0, y_0) = Center of gravity of all electrons on the target, (x_i, y_i) = Position of i^{th} electron

The values of σ in different cases depending upon existence of bending and geometrical errors are given in figure 2.9. It was found that bending of the e-beam imposes the most significant limit in getting a compact spot as compared to geometrical errors such as finiteness of the coil, angular misalignment and positional offset. In this case also, the reason for non-zero σ for thin coil without any geometrical errors is spherical aberration.

To summarize, bending of the beam affects the shape and compactness of the e-beam spot where as geometrical errors such as angular misalignment and positional offset of the beam result in shift of the spot from center of the target.

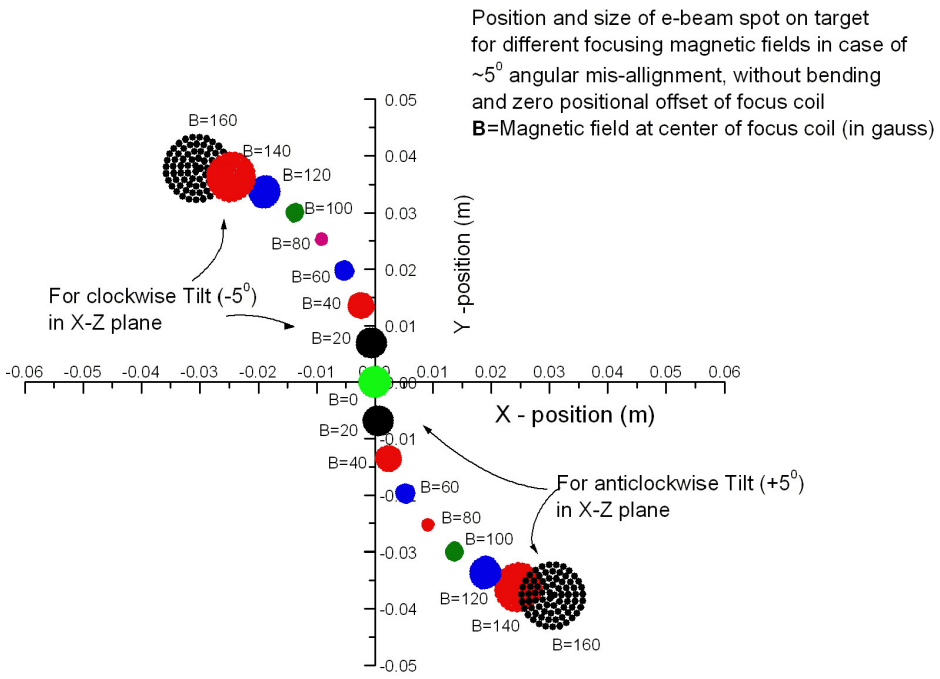

Figure 2.2 Position and size of e-beam spot on target at different focusing magnetic fields in the case of ~5^0 angular misalignment of focus coil, without positional offset of coil and without bending of e-beam

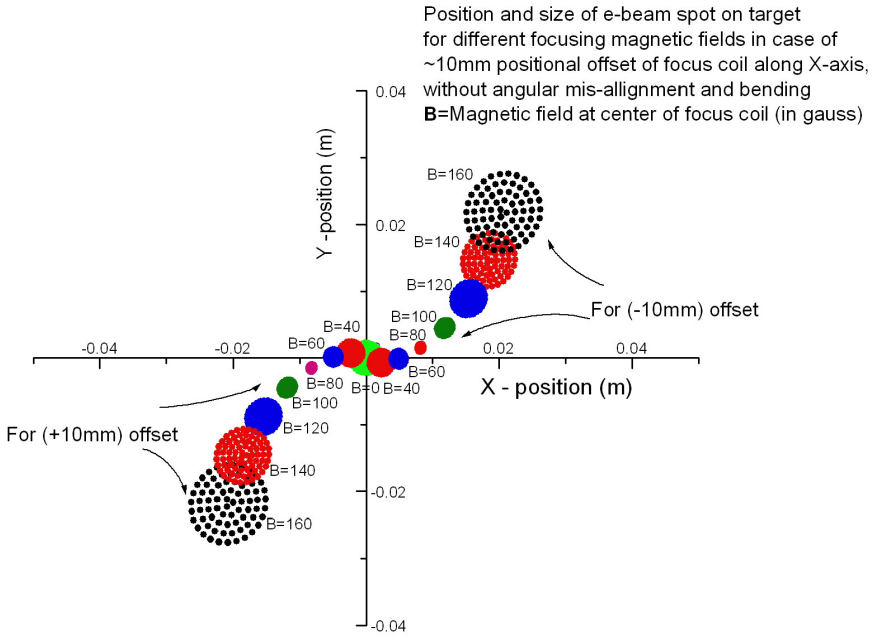

Figure 2.3 Position and size of e-beam spot on target at different focusing magnetic fields in case of without angular misalignment of focus coil, ~10mm positional offset of coil and without bending of e-beam

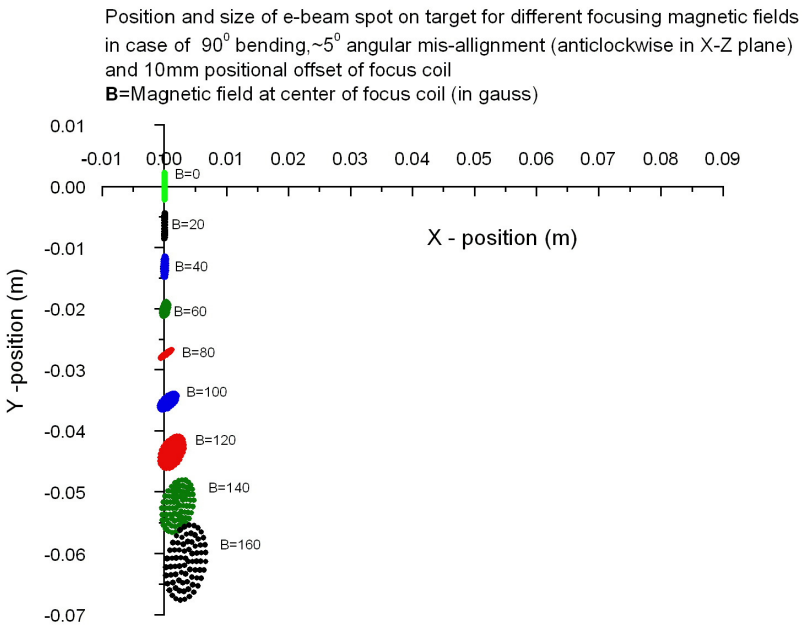

Figure 2.4 Position and size of e-beam spot on target at different focusing magnetic fields in case of 90^0 bending, ~5^0 angular misalignment (anticlockwise in XZ- plane) and 10mm positional offset of focus coil

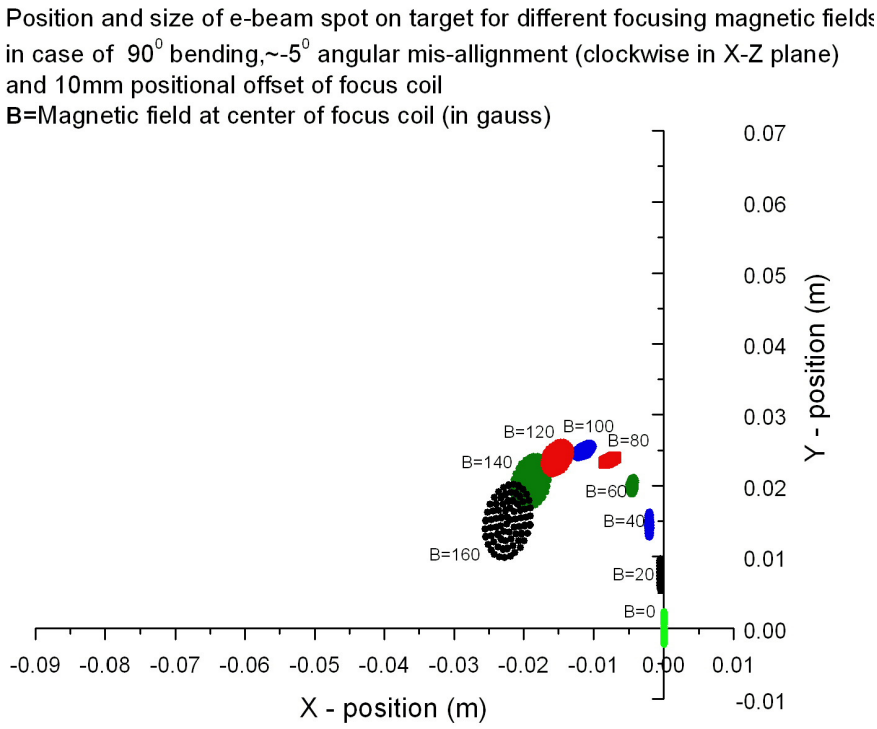

Figure 2.5 Position and size of e-beam spot on target at different focusing magnetic fields in case of 90^0 bending, ~ -5^0 angular misalignment (clockwise in XZ- plane) and 10mm positional offset of focus coil

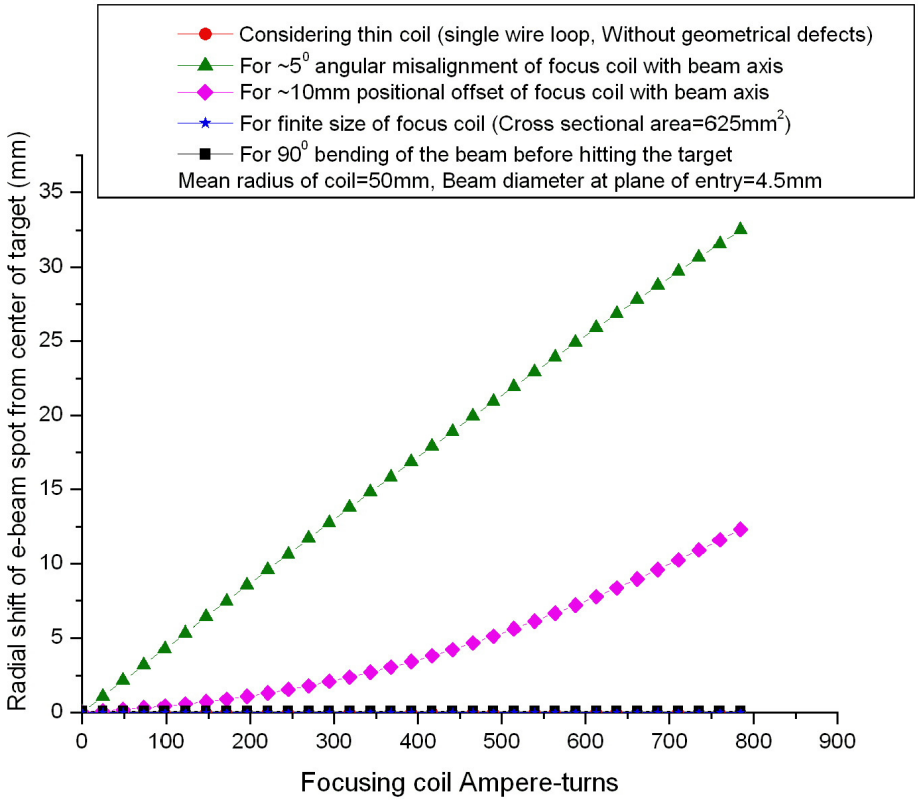

Figure 2.6 Comparison of radial shift of e-beam spot from center of target at different focusing coil currents for different cases such as (a) Thin coil, Zero geometrical errors, without bending of beam (b) Thin coil, ~5^0 angular misalignment , without bending of beam (c) Thin coil, 10mm positional offset, without bending of beam (d) Thick coil of finite cross section (square shape, thickness=25mm), Zero angular misalignment/positional offset, without bending of beam (e) Thin coil, Zero geometrical errors and 90^0 bending of beam

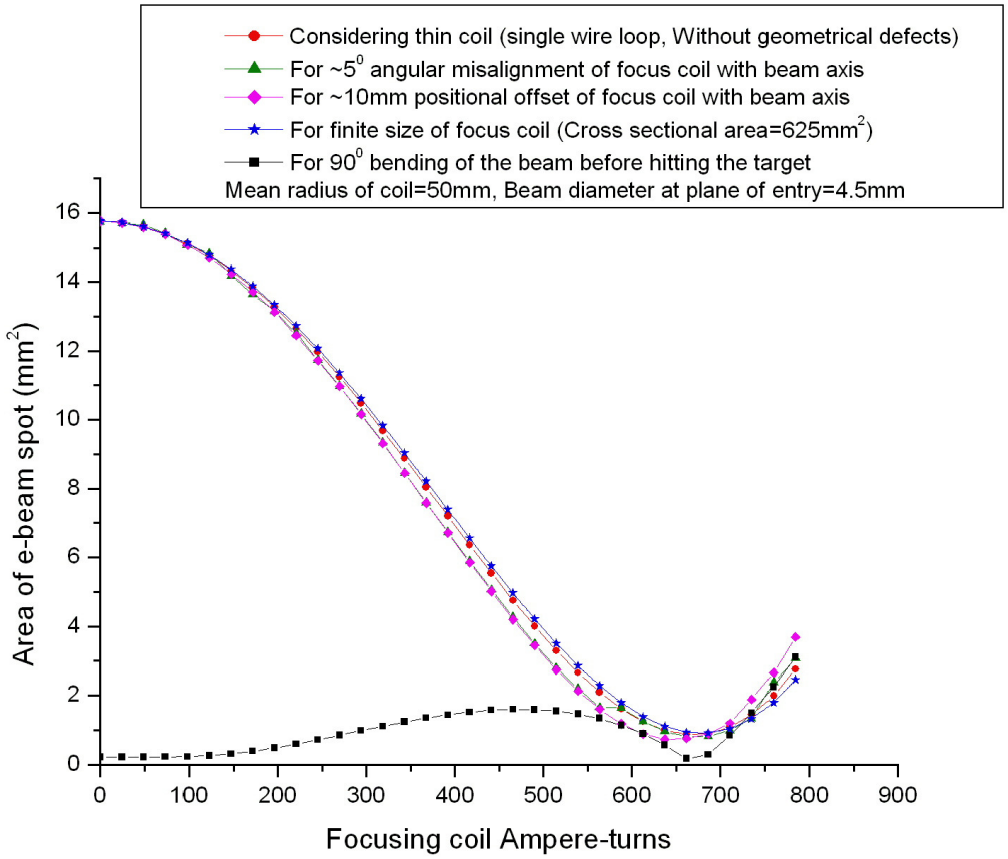

Figure 2.7 Comparison of area of e-beam spot on target at different focusing coil currents for different cases such as (a) Thin coil, Zero geometrical errors, without bending of beam (b) Thin coil, ~5^0 angular misalignment , without bending of beam (c) Thin coil, 10mm positional offset, without bending of beam (d) Thick coil of finite cross section (square shape, thickness=25mm), Zero angular misalignment/positional offset, without bending of beam
(e) Thin coil, Zero geometrical errors and 90^0 bending of beam

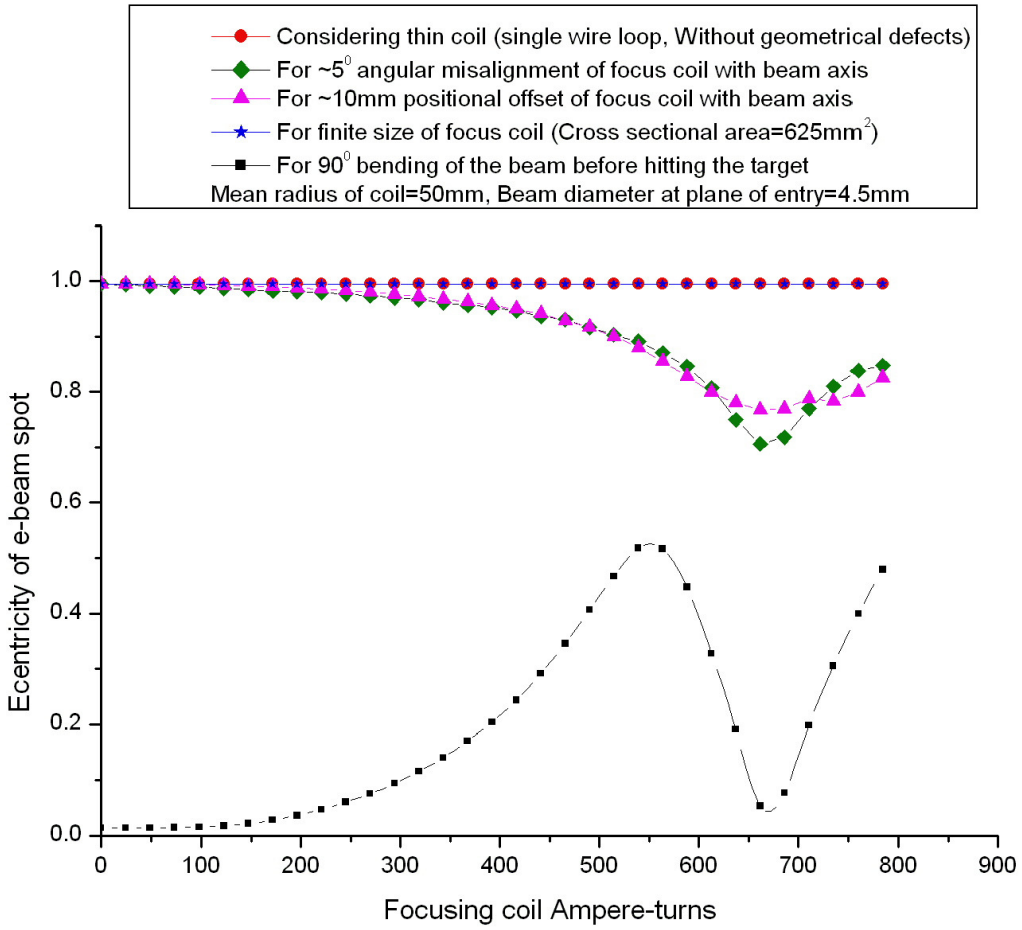

Figure 2.8 Comparison of circular symmetry of e-beam spot on target as indicated by eccentricity at different focusing coil currents for different cases such as (a) Thin coil, Zero geometrical errors, without bending of beam (b) Thin coil, ~5^0 angular misalignment , without bending of beam (c) Thin coil, 10mm positional offset, without bending of beam (d) Thick coil of finite cross section (square shape, thickness=25mm), Zero angular misalignment/positional offset, without bending of beam (e) Thin coil, Zero geometrical errors and 90^0 bending of beam

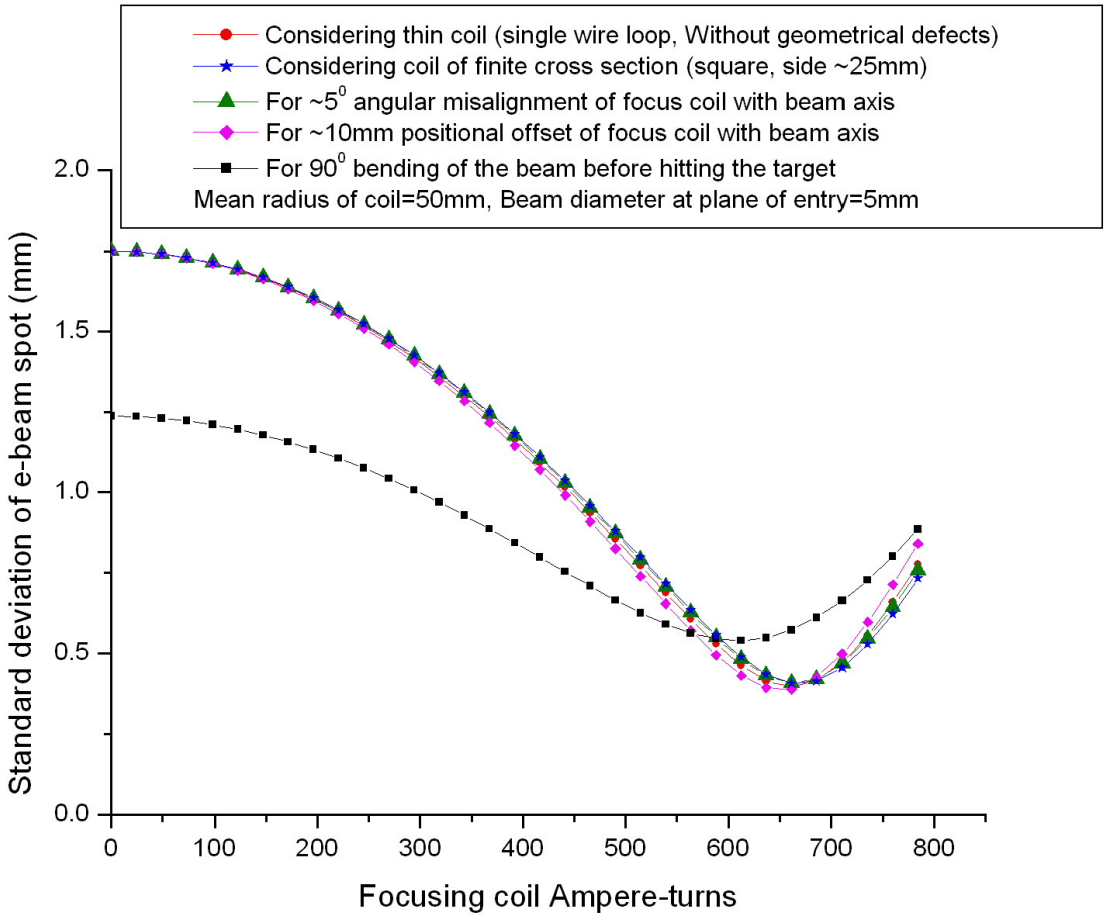

Figure 2.9 Comparison of compactness of e-beam spot on target at different focusing coil currents for different cases such as (a) Thin coil, Zero geometrical errors, without bending of beam (b) Thin coil, ~5^0 angular misalignment , without bending of beam (c) Thin coil, 10mm positional offset, without bending of beam (d) Thick coil of finite cross section (square shape, thickness=25mm), Zero angular misalignment/positional offset, without bending of beam (e) Thin coil, Zero geometrical errors and 90^0 bending of beam

2.2 A novel scheme for ideal distortion-less focusing of a bent electron beam

As described in earlier section, the e-beam is bent before hitting the target to avoid metal vapor and associated ions (created by Saha ionization and electron impact ionization [3]) which otherwise may proceed towards cathode-anode region of the e-gun causing electrical discharges [1], instabilities [4] and metallic coatings on the high voltage components and insulators.

In the currently used commercial transverse type e-guns, a transverse magnetic field is applied for bending of the e-beam by 90^0 or 270^0 and the e-beam is focused due to geometrical crossover at those angles. So, focusing occurs in a direction perpendicular to the direction of bending magnetic field. But, beam width along the direction of magnetic field remains same or becomes more as no focusing action occurs in this direction during bending. In other words, the beam spot on the target when focused becomes a straight line or an ellipse. On the other hand, in axial type of e-guns, even if a beam with circular cross section is initially made convergent by a coaxial magnetic lens, its focusing quality and circular symmetry is distorted by the bending magnetic field through which it has to pass before hitting the target. This is due to the fact that points of convergence along axis of the bent e-beam in two orthogonal axes are not coincident. Thus eventually, we again end up in getting an elliptical spot on the target.

However, to achieve very high power density especially as required by applications like PVD, welding etc., two dimensional focusing along two perpendicular directions on the target plane is desirable so that the required power density can be achieved at lower total e-beam power. In addition to this, circular symmetry of the e-beam spot on the target is beneficial for welding application and PVD processes where circularly symmetric vapor

density distribution is required. Therefore, ideally e-beam spot should converge to a point in spite of the bending in magnetic field.

For non-paraxial beams when beam diameter is comparable with the radius of curvature of bending, use of weak focusing schemes [28-30] (used in accelerators) cannot focus all the electrons into a single point on the target even if appropriate bending magnetic field is applied. This is due to the fact that weak focusing of a bent beam requires the beam width to be very small as compared to the radius of curvature of the beam. Again, weak focusing scheme acts just as a confinement exerting a restoring force on the electrons escaping vertically from the plane of rotation by interaction of the small radial magnetic field generated by increasing pole gap with the moving electrons. It is not capable of focusing all the electrons along two transverse directions into a single point after traversing a particular angular distance. In this work, we get rid of this limitation of the weak focusing scheme, viz. the inability to focus a non-paraxial bent e-beam to a single point on target using a unidirectional spatially varying magnetic field. By non-paraxial beam, we only mean that the beam width is comparable with the radius of bending, but of course the unidirectional magnetic field has to be defect less. Implementation of strong focusing scheme (alternating gradient magnetic field) in an e-beam evaporator or wielding machine is not possible due to space constraints, high temperature and presence of metallic vapor.

At first, we derive the theoretical conditions required for focusing a non-paraxial e-beam into a point on the target for any angle of bending in a magnetic field neglecting space charge. Although, the ultimate limit of the beam width at the focused point will be dominated by space charge effect, we try to eliminate the imperfections introduced due to bending of the e-beam of finite cross sectional width. In applications such as e-beam welding and evaporation systems, kinetic energy of the electrons has a range ~10 to 150kV while e-beam current has a range 0.01A to 1A. In these cases, distortion of the e-beam spot due to bending

of the beam dominants over the effect of space charge. This was confirmed by calculating the minimum achievable radius of the beam due to space charge effect using the following beam envelope equation as reported in references [31] and [32].

$$\frac{d^2r}{dz^2} = \frac{K}{r} \tag{2.4}$$

where, r = radius of the beam at any axial distance 'z' ,

Factor for Space charge effect, $K = \dfrac{eI}{2\pi\varepsilon_0 mc^3\left(\gamma^2 - 1\right)^{3/2}}$

I = Beam current, m = Rest mass of electron, e = Electronic charge

$\gamma = 1/\sqrt{1 - v^2/c^2}$, (v is axial velocity and c is velocity of light),

We have numerically solved the Equation 2.4. For a typical converging beam of initial radius ~5mm at the exit of thin magnetic lens and target at distance of 250mm, the beam waist radius comes out to be 0.04mm for a 100kV, 10kW welding machine and it is 1.3mm for a 60kV,10kW evaporation system. As the desired beam radius for welding and evaporation systems are more than these values (~1mm and ~3mm respectively), we can say that the above mentioned space charge effect do not impose significant limitation on the desired size of e-beam spot. Thus, the distortion due to bending of the beam can play a much more significant role in defocusing (and introducing asymmetry) and comes into picture well before the dominance of space charge effect. So, in this section, we analytically develop a method to completely eliminate the imperfections introduced due to bending of the e-beam.

In the next part of this section, we also modify the expression so that it is applicable for the case when kinetic energy of the electrons increases due to time-varying field during its motion through the bending magnetic field (for applications like betatrons). Finally, we evaluate the performance in a numerical model of e-gun.

2.2.1 Theory of the novel scheme for Ideal Focusing-Cum-Bending of e-beam:-

Let an e-beam that bends by an angle $\propto$ reach the target plane after passing through a magnetic field *B(r)* as shown in figure 2.10. The bending magnetic field *B(r)* is directed along Z-axis and it varies only with radial distance *R* from *O*.

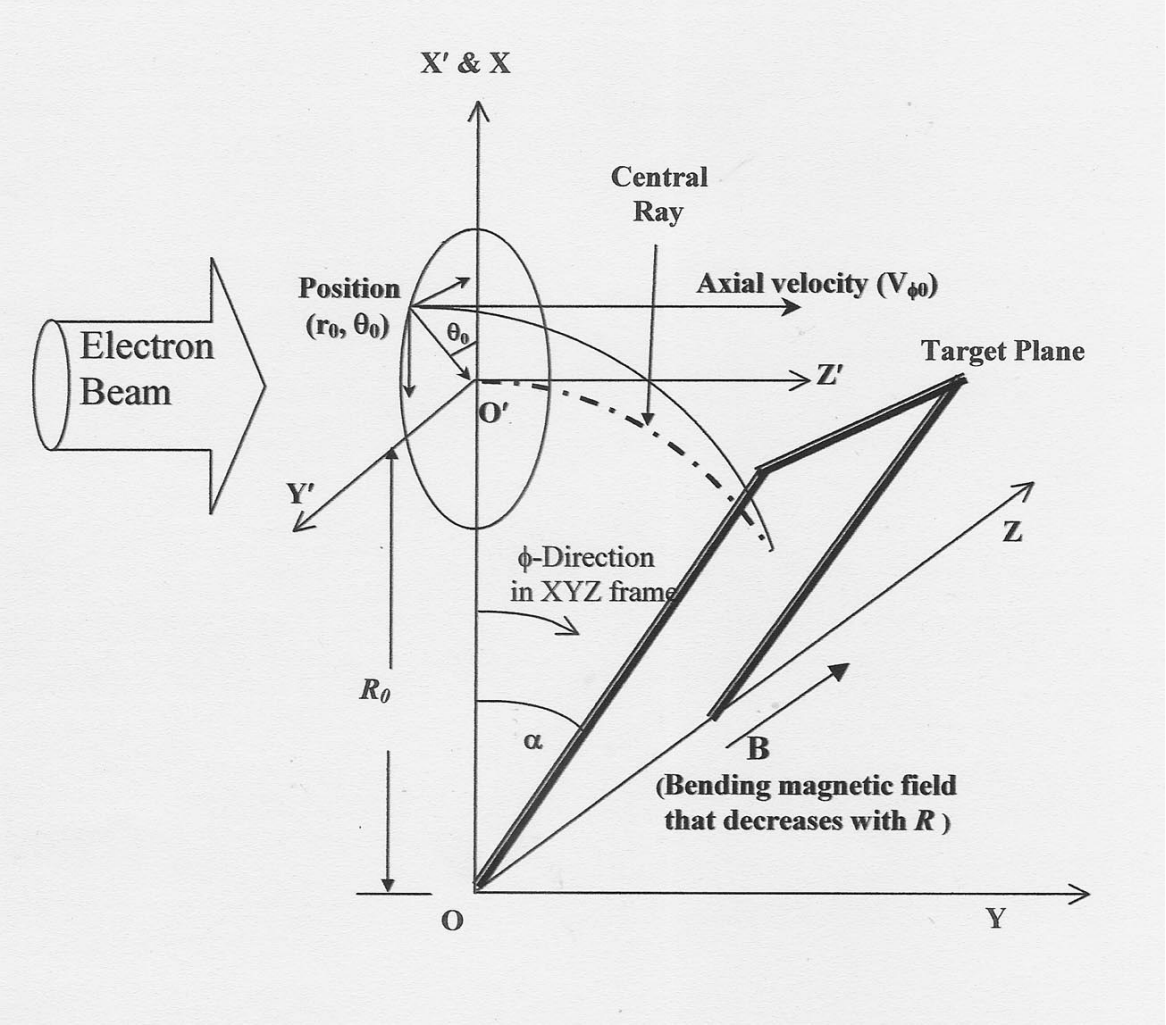

Figure 2.10 Three dimensional geometry of the e-beam for analytical solution

Relations between the two frames of references XYZ and X′Y′Z′ are,

$X = R0 + X'$; $Y = Z'$; $Z = -Y'$

Using the differential equation governing the motion of electron in magnetic field [5] radial acceleration in XYZ-frame is given by,

$$\frac{dV_R}{dt} = R\frac{d\phi}{dt}\left(\frac{d\phi}{dt} - \frac{Be}{m}\right)$$

Where, m is mass and e is charge of electron.

As $\frac{d\phi}{dt} = \frac{V_\varphi}{R}$, we get,

$$\frac{dV_R}{dt} = R\frac{d\phi}{dt}\left(\frac{V_\varphi}{R} - \frac{Be}{m}\right)$$

So, we see that radial velocity V_R of the electron will remain constant during its travel through the bending magnetic field i.e. dV_R/dt =0 only if centrifugal force is balanced by $\vec{v}\times\vec{B}$ force i.e. $\frac{mV_\varphi^2}{R} = BeV_\varphi$

or $$B = \frac{mV_\varphi}{eR}$$

If the above condition is satisfied, the electron moves with constant radial velocity towards O and it has already constant velocity along Z-axis (i.e. along magnetic field). If there is no external source of energy, its tangential velocity must also be same as the initial tangential velocity. Thus we get,

$$V_z = V_{z0} \ , \ V_R = V_{R0} \text{ and } V_\Phi = V_{\Phi 0} \qquad (2.5)$$

Putting Eq. (2.5) in expression for B, the required condition for constant radial velocity of electron is given by,

$$B = \frac{mV_{\varphi 0}}{eR} \qquad (2.6)$$

Thus, if all the electrons in the beam have same initial tangential velocity $V_{\Phi 0}$ and B is given by Eq. (2.6), then velocities of all the electrons in the cylindrical coordinate system-XYZ shown in Fig. 2.10 will be conserved. In case of electrons with very high energy (>400kV), the value of m in Eq. (2.6) should be taken as relativistic mass of electron instead of rest mass

(i.e. $m = m_0 / \sqrt{1 - v^2 / c^2}$ where m_0 is rest mass, v is speed of electron and c is velocity of light). Because the speed of electron v is constant (as there is no supply of external energy), m is also constant although it is different from rest mass m_0.

Let the height of central ray of e-beam from O be R_0 and an electron be initially at position M(r_0 , θ_0) on plane $X'Y'$. Projection of the trajectory of electron on the plane of curvature is shown in Fig. 2.11. Since radial velocity of the electron towards central ray of the beam V_r is a vector addition of V_R and V_z both of which are time invariant (equation 2.5), V_r will also remain same at its initial value V_{r0} . So the electron will converge to the central ray only if,

$$V_{r0}\ T = -r_0 \tag{2.7}$$

Where T is the total time of travel in magnetic field before hitting the target.

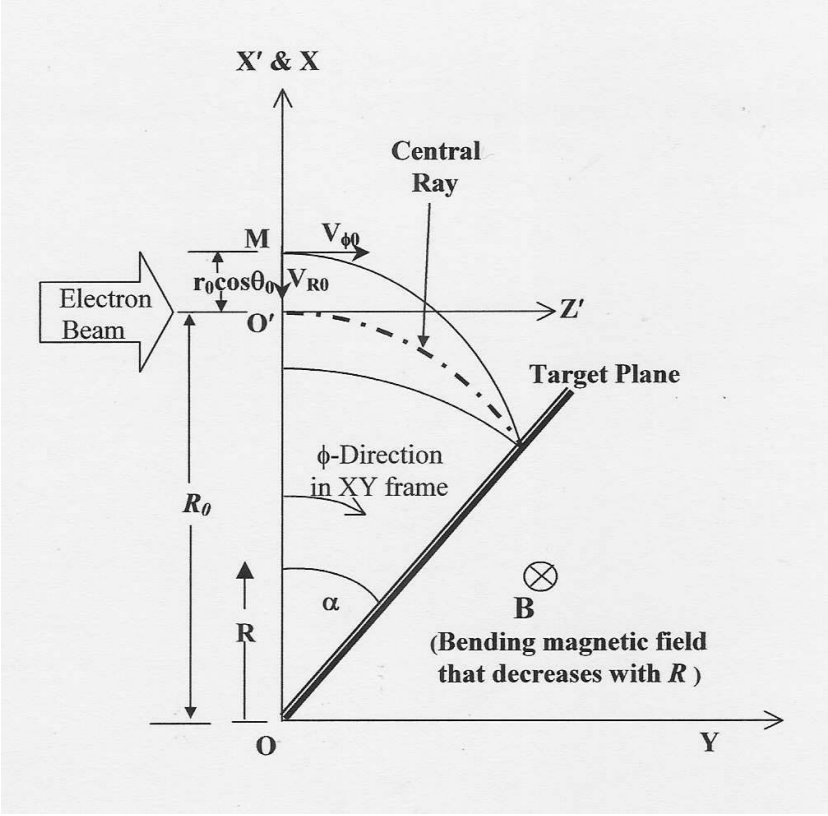

Figure 2.11 Projection of trajectory of motion on the plane of curvature of electrons

If the electrons have no initial tangential velocity about O' on plane X′Y′ i.e. $V_{\theta 0}$ = 0, then initial value of radial velocity V_R towards O in XYZ plane will be given by $V_{r0}\cos\theta_0$. As the radial velocity has been made constant, it must be equal to its initial value and so,

$$V_R = V_{r0}\cos\theta_0 \tag{2.8}$$

Now the time of travel of the electron can be calculated from following relation,

$$\alpha = \int_0^T \left(\frac{d\phi}{dt}\right) dt = \int_0^T \left(\frac{V_\phi}{R}\right) dt$$

As the radial distance from O at any instant of time is, $R = (R_0 + r_0\cos\theta_0) + V_R\, t$, and using Equation 2.5 and 2.8, we get,

$$\alpha = V_{\phi 0} \int_0^T \frac{dt}{\mathrm{R}_0 + r_0\cos\theta_0 + tV_{r0}\cos\theta_0} \tag{2.9}$$

or
$$T = \frac{R_0 + r_0\cos\theta_0}{V_{r0}\cos\theta_0}\left(e^{\frac{\alpha V_{r0}\cos\theta_0}{V_{\phi 0}}} - 1\right) \tag{2.10}$$

Eliminating T from Eq. (2.10) and Eq. (2.7), required initial radial velocity distribution of the electrons within the beam to make them focused after bending by an angle α is given by,

$$V_{r0} = \frac{-V_{\phi 0}}{\alpha\cos\theta_0}\ln\left(1 + \frac{r_0\cos\theta_0}{R_0}\right) \tag{2.11}$$

Along with the above condition, as stated earlier, initial axial velocity of the beam should be same for all electrons (i.e. $V_{\Phi 0}$ same for electrons), there should be no initial tangential velocity about O′ on X′Y′ plane (i.e. $V_{\theta 0}$ = 0), and Of course, magnetic field $\boldsymbol{B}$ should obey Eq. (2.6). In this way, the effect of beam bending on the quality of focusing can be completely eliminated for any angle of bending even if the beam is non-paraxial.

The radial velocity distribution given by Eq. (2.11) is circularly *asymmetric* about O′. This is also graphically shown in Figure 2.12 where variation of radial velocity of electron with initial angular position on X′Y′ plane at different radial distances from O′ are plotted (assumed value of R_0=10cm and $\propto=270^0$). We see that magnitude of inward radial velocity is highest at 180^0 position. This asymmetric property (θ_0 dependency) decreases as the radial distance becomes small compared to the bending radius of the beam. This type of distribution may be achieved by use of a circularly asymmetric segmented cathode having varying voltages among the segments for generation of electrons or a stigmator [6] or by use of circularly asymmetric multi-electrode electrostatic lens [7,33-34]. As the high voltage component is outside the region of vapor, problem of electrical discharges will not be there.

However, for paraxial beams where beam cross section is very small as compared to the bending radius of the beam i.e. $r_0 << R_0$, Eq. (2.11) reduces to,

$$V_{r0} = \frac{-V_{\phi 0} r_0}{\alpha R_0} \tag{2.12}$$

Thus, radial velocity requirement becomes independent of θ_0 i.e. required radial velocity distribution becomes circularly *symmetric* and it is directly proportional to the initial radial distance of the electron from the central ray. So, velocity distribution of Equation 2.12 is same as that required for focusing of a straight e-beam on target placed at a distance of '$\propto R_0$' from focus coil. This type distribution can be easily achieved by use of a coaxial magnetic lens [33]. Again due to paraxial nature of the beam, axial velocity of all the electrons remains approximately same. So, the paraxial beam gets focused to a point on the target after being bent by any angle due to presence of only spatially varying bending magnetic field.

Now, we modify the expressions so that they are applicable for betatrons, where kinetic energy of the electrons gradually increases during its motion through the bending magnetic field. For simplicity we will assume that tangential velocity of the electrons V_Φ increases linearly with time at a rate of *k* i.e. $V_\Phi = V_{\Phi 0} + k\,t$. Then for constancy of the radial velocity, B should also be increased as per following equation,

$$B = \frac{m(V_{\varphi 0} + kt)}{eR} \tag{2.13}$$

Here, electrons pass through the magnetic field in bunches so that at any time all the electrons have same tangential velocity. Although Equation 2.13 shows that B increases linearly with time at lower energy (<400keV), at higher energy relativistic mass of electron has to be taken for *m* (i.e. $m = m_0 / \sqrt{1 - v^2 / c^2}$ where m_0 is rest mass, *v* is speed of electron and *c* is velocity of light). In that case, B has to be increased nonlinearly so as to take care of the increase in *m* in Equation 2.13 as speed of electron *v* increases with time.

Velocity along Z-axis is not at all affected as the magnetic field is directed along this direction. So, Equation 2.9 will be valid in following modified form,

$$\alpha = \int_0^T \frac{(V_{\phi 0} + kt)dt}{\mathrm{R}_0 + r_0 \cos\theta_0 + tV_{r0} \cos\theta_0} \tag{2.14}$$

Integrating and using Eq. (2.7) to replace T (focusing condition),

$$\alpha = \left[\frac{k(R_0 + r_0 \cos\theta_0)}{V_{r0}^2 \cos^2\theta_0} - \frac{V_{\varphi 0}}{V_{r0} \cos\theta_0} \right] \ln\left(1 + \frac{r_0 \cos\theta_0}{R_0} \right) - \frac{kr_0}{V_{r0}^2 \cos\theta_0}$$

By solving the above quadratic equation we get the required initial velocity distribution as,

$$V_{r0} = -\frac{V_{\varphi 0}}{2\alpha \cos\theta_0}\ln\left(1+\frac{r_0\cos\theta_0}{R_0}\right) - \sqrt{\frac{V_{\phi 0}^2}{4\alpha^2\cos^2\theta_0}\left[\ln\left(1+\frac{r_0\cos\theta_0}{R_0}\right)\right]^2 + k\left[\left(\frac{R_0+r_0\cos\theta_0}{\alpha\cos^2\theta_0}\right)\ln\left(1+\frac{r_0\cos\theta_0}{R_0}\right)-\frac{r_0}{\alpha\cos\theta_0}\right]} \quad (2.15)$$

Although, achieving the above initial radial velocity distribution given by Eq. (2.15) may be practically difficult, we will gain in terms of the reduced complexity of the magnetic field design for perfect focusing of the non-paraxial beam of charge particles. It will be interesting to examine the form of Equation 2.15 when, $r_0 << R_0$ so that

$$\ln\left(1+\frac{r_0\cos\theta_0}{R_0}\right) \approx \frac{r_0\cos\theta_0}{R_0}.$$

So, we get,

$$V_{r0} = -\frac{V_{\varphi 0} r_0}{\alpha R_0}\left(\frac{1}{2}+\frac{1}{2}\sqrt{1+\frac{4k\alpha R_0}{V_{\phi 0}^2}}\right) \quad (2.16)$$

Thus, in case of paraxial beam required initial velocity distribution becomes circularly symmetric given by Equation 2.16 which can be easily realized through a thin magnetic or electrostatic lens.

2.2.2 Numerical model for performance evaluation:

A numerical model of e-gun was utilized to evaluate the advantages of above mentioned scheme. A computer code using 'C' language was made in-house to trace the electron trajectory in spatially varying magnetic field. We have solved the differential equation of motion using fourth order Runge-Kutta technique. In this model, an e-beam with circular cross section bends by an angle α during its passage through bending magnetic field to hit the target at 90^0. To evaluate the quality of focusing, we calculated the standard deviation 'σ' of their final positions on target from the mean position as used by other

researchers [27]. Ideally, a convergent beam without bending should be focused to a point and σ should be zero. Due to bending, non-uniform displacement of the beam along different directions makes the spot elliptical (or a straight line) thereby increasing the σ value. Thus, value of σ signifies how close the beam spot is to the desirable ideal case (i.e. a point). We started with about ~5000 electrons uniformly distributed on a circular area at the entry plane of bending magnetic field and the bending angle α was varied from 0^0 to 270^0. In each case, total path length of e-beam in magnetic field was held constant. The value of σ *vs.* α was simulated for three different cases viz.

a) Spatially *uniform* bending magnetic field ***B*** and circularly *symmetric* radial velocity of electrons as obtained from a coaxial magnetic lens in the form of Eq. (2.12) (i.e. conventional scheme)

b) Spatially *decreasing* ***B*** (Eq. (2)) and circularly *symmetric* radial velocity of electrons as obtained from a coaxial magnetic lens in the form of Eq. (2.12)(i.e. scheme for paraxial beam)

c) Spatially *decreasing* ***B*** (Eq. (2)) and circularly *Asymmetric* radial velocity of electrons in the form of Eq. (2.11) (i.e. exact scheme)

Fig. 2.13 shows the graph of σ vs. α for above three cases for a beam of cross sectional radius ~5 mm and path length of ~100mm. It was found that σ increases very sharply to a maximum of about ~2.8mm with bending of the beam in case of conventional scheme (case-a) where uniform magnetic field is used. The peak near $\propto = 160^0$ is due to the fact that two initially parallel electrons moving in proximity and circular paths become farthest from each other after 180^0 rotation. In case of exact scheme (case-c), σ is zero for all angles of bending as expected (actually it is $\sim 10^{-5}$ due to digital error of computation). However, by use of scheme for paraxial beam (case-b) i.e. decreasing B and symmetric focusing, σ was found to be much lower than the case-a which is very good in view of the fact that complexity of cathode or stigmator or asymmetric electrostatic focusing is avoided.

To get an idea about the shape of e-beam spot on the target, the simulated e-beam spots on the target for 270^0 bent beam for the three cases (a, b, and c) are given in Fig. 2.14. It is clear that shape of the e-beam spot in case of 'b' and 'c' are much better than the shape in conventional case.

2.2.3 Conclusions:

It was concluded that the effect of bending on the size and shape of e-beam spot on the target can be completely eliminated (theoretically made zero) by choosing a radially decreasing magnetic field from the centre of curvature along with a *circularly asymmetric* radial velocity distribution when paraxial condition is not valid. In the paraxial case, elimination of the bending effect is possible by using the radially decreasing magnetic field and *circularly symmetric* radial velocity distribution that is easily achieved by a coaxial thin magnetic lens. These conclusions are valid for any angle of bending of the e-beam. The principle can be used in applications like e-beam evaporation and e-beam welding. The scheme can also be extended to applications like betatrons where kinetic energy of the particles increases with time during bending. The radially decreasing flux can be obtained by linearly increasing the air gap between the two pole faces. By carrying out this type of modification in the bent beam e-guns, two-dimensional focusing of the e-beam can be achieved leading to a circular e-beam spot with high power density along with the advantage of keeping e-gun in geometrical shadow region of vapor.

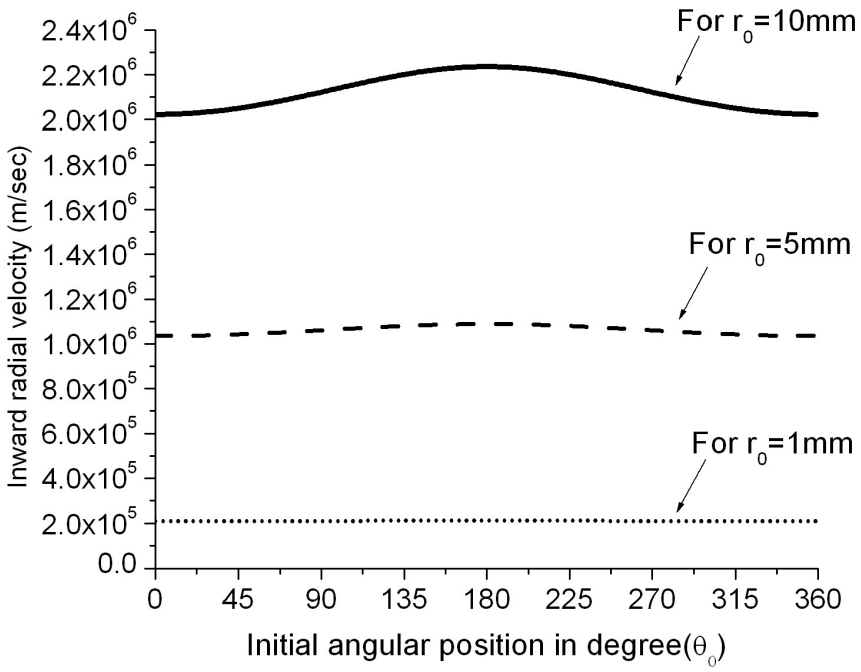

Figure 2.12 Variation of radial velocity of electron with initial angular position on X′Y′ plane

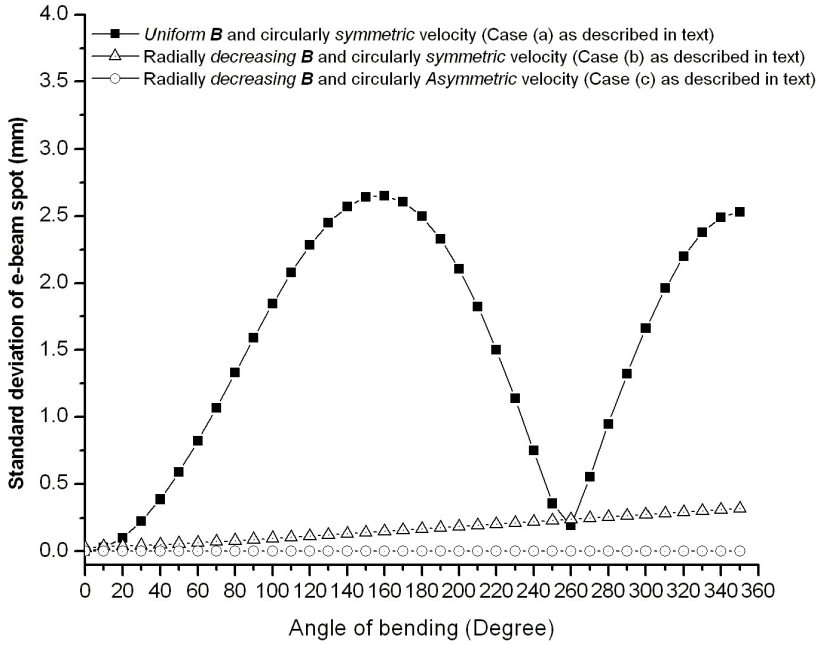

Figure 2.13 Variation of standard deviation of e-beam spot with angle of bending for three different cases (a), (b) and (c)

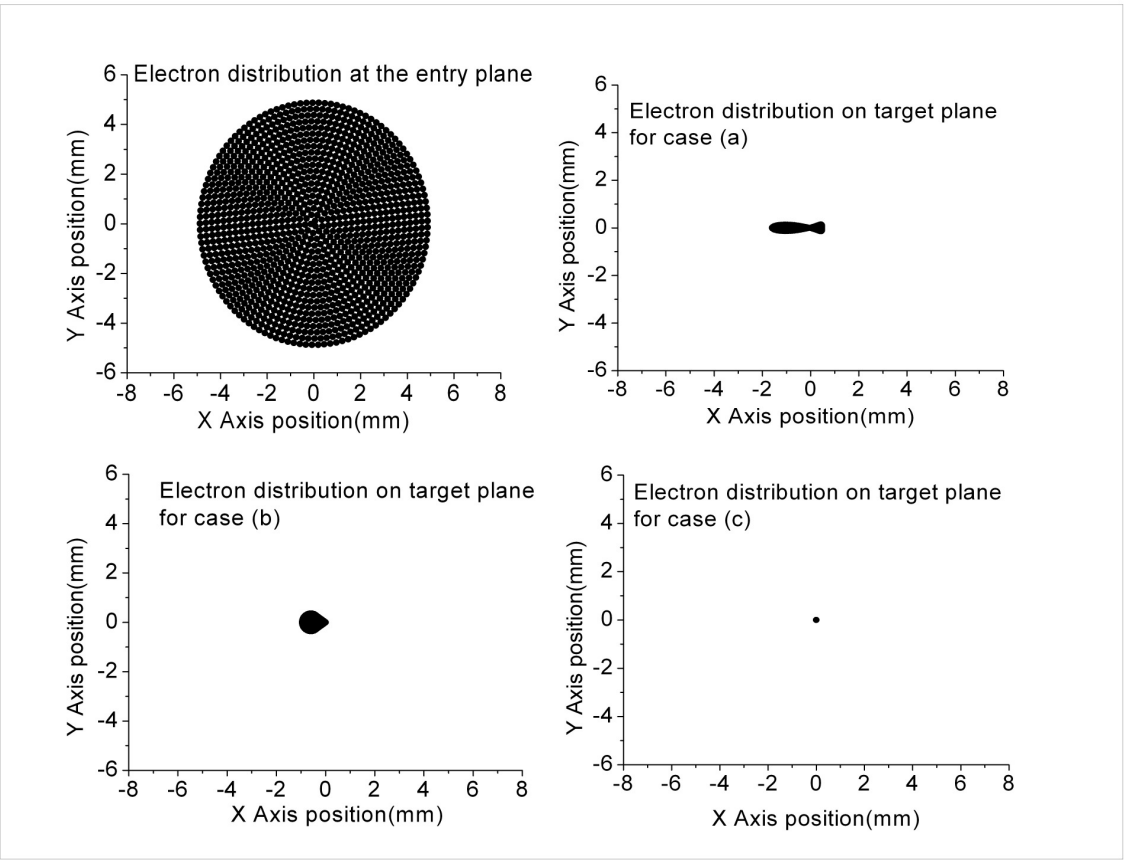

Figure 2.14 Variation of size and shape of e-beam spot on target for 270^0 bending from the initial spot size for three different cases (a), (b) and (c)

CHAPTER – 3

Instability of beam current in e-beam evaporation system

3.1 Hysteresis in electron emission current

Stability of the electron emission current is a desirable feature in e-guns used for evaporation of metals. However, a region of instability in the form of hysteresis in electron emission current from cathode was observed. This coincided with the point where evaporation of the metal target starts. It was found that in the upward direction of power change, the required filament-heating current for a specified e-beam current was significantly higher than the filament current required in the downward direction. The detailed observation and theoretical analysis for understanding the above phenomena are given below.

3.1.1 Factors affecting electron emission process

The source of electrons in an e-gun is usually a thin filament in the shape of a wire or tape made up of refractory metals like tantalum or tungsten. For thermionic emission of electrons from the filament, its temperature is raised to about 2500 K. As the electrons are emitted from a very small area of the thin filament, the heating power required in this small area to maintain itself at elevated temperature is usually small (~20W for a 10 kW e-gun). So, any minute thermal disturbance on the filament coming from the evaporation process can alter the thermodynamic equilibrium of the filament. One such process is ion bombardment on the electron-emitting filament during evaporation. Although, majority of the e-beam generated metal ions co-propagate with the neutral atoms and undergo processes like diffusion and expansion in field free region to end up on walls, some of the ions are trapped in the negative potential well created by the non-neutral e-beam. These ions initially of thermal energy (~ 0.26eV, corresponding to a temperature of 3000 K of the target), thus drift in a direction opposite to the propagation of e-beam. Finally, in the electron acceleration region of the e-gun

i.e. cathode-anode gap, they bombard the e-gun filament cathode at a kinetic energy that corresponds to the full potential of the cathode (~ tens of keV). This bombardment of ions leads to an increase in temperature of the electron-emitting filament. As the e-guns are normally operated in temperature limited mode, the aforesaid ion bombardment ultimately results in an increase in e-beam current in spite of constancy of the external heating power input to the filament. In principle, an increase in e-beam current can also take place by means of secondary electron emission, field emission due to presence of ion cloud and I^2R heating by ion current during the process of ion bombardment on cathode. Thus, experiments have to be designed so as to produce results that will identify the dominant factors affecting the electron emission process and that will also show a direction to the probable solution. The subsequent sections explain the experiment carried out by us and also the analysis of the results so obtained.

3.1.2 Experimental observation

The experimental system (figure 3.1) consists of a vacuum chamber in which background pressure is maintained at ~10^{-5} mbar and the metal target to be heated by e-beam is placed in a water-cooled copper crucible. The e-gun assembly (32kV, 250mA) that makes an angle of 45^0 with the horizontal plane consists of a square sized (area~2.6mm×2.6mm) directly heated tantalum strip cathode and a copper anode with a distance of about ~9mm between them. The cathode which is a 0.1 mm thick tantalum filament biased at ~ -30kV to –32kV DC voltage acts as an electron emitting surface. A hemispherical grid-cup (Whenelt electrode) kept at the same voltage as cathode, encircles the filament for beam shaping. A maximum rms ac current of 60 Amp can be passed through the filament for raising its temperature to enable thermionic electron emission to occur. The size of the anode hole at the e-beam entry is ~5mm and size at exit side is 10mm.

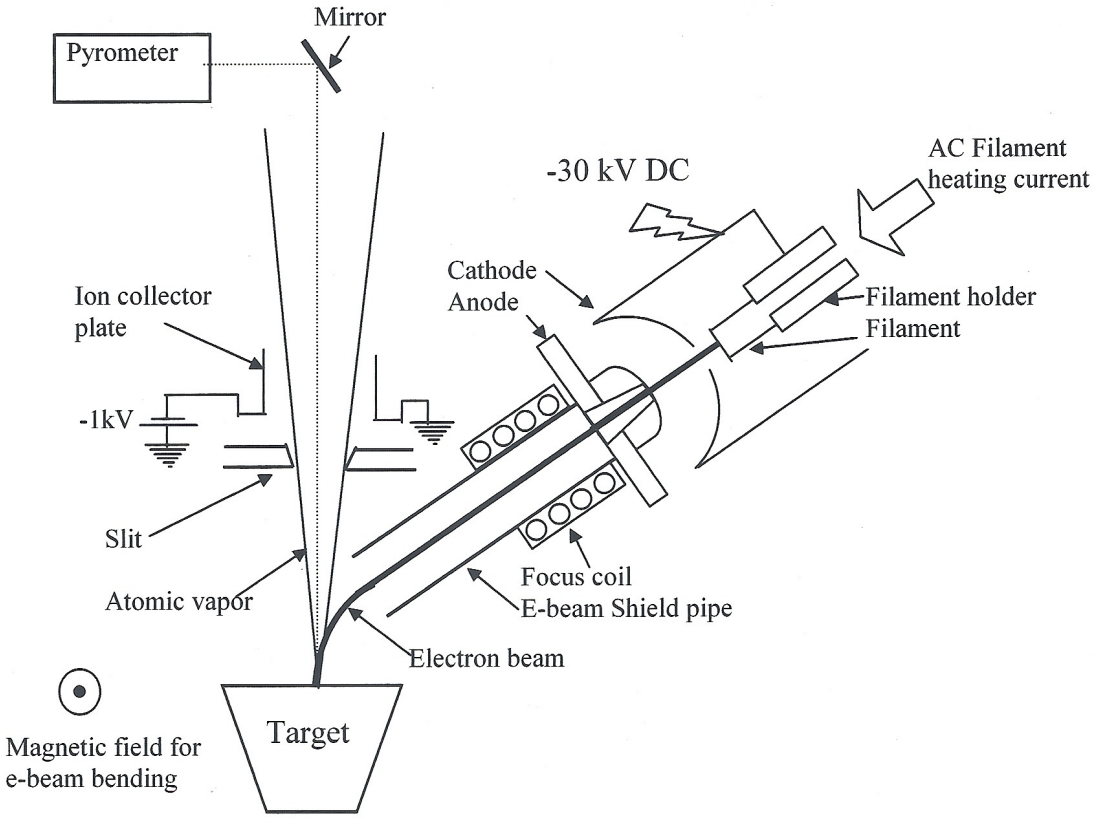

Figure 3.1 Experimental set-up of e-beam evaporation system

The e-beam produced by the e-gun is focused by a co-axial magnetic field generated by a short focusing coil. On emerging from the focusing coil region, the e-beam moves in a straight line through a mild steel pipe, which shields the e-beam from any external magnetic field. Finally, near the target, the e-beam turns by an angle of 45^0 by externally applied bending magnetic field so that it hits the target at 90^0 incidence angle. The hot zone created at the e-beam spot region gives rise to evaporation of target material. The temperature of the e-beam spot was measured by a two-color pyrometer (TCP) that sees the e-beam spot through a periscope arrangement. The generated metal vapor passes through a collimating slit of size 100mm × 5mm and an ion collection region as shown in figure 3.1. A DC electric field (~ 200 V/cm) is applied between the two parallel plates and the negatively biased plate collects ions from the metal vapor.

With uranium as target in the crucible, the electron emission current of the e-gun was gradually increased by varying the filament heating current. We increased the e-beam current very slowly, waiting for about 8-10 min at every step of ~10-15mA, so that outgassing from the target does not significantly increase the pressure in vacuum chamber. We were certain that steady state temperature was reached by the filament at every step because e-beam current which depends on temperature of the filament increased within few seconds of increase in filament heating current. In the next section, it is analytically shown that the time required for attainment of equilibrium temperature by the electron-emitting area of the filament (square sized area ~2.6mm×2.6 mm) is of the order of ~0.1s and thus, the wait period of 8-10 minutes at each step was much more than that required for equilibrium. During this process, the voltage of the cathode was held constant at -28 kV. The e-beam current (I_b) extracted from the cathode was recorded with increase in filament-heating current (I_f) and is shown in figure 3.2. At values I_b ~190mA, the filament current was again reduced gradually and the corresponding e-beam currents were recorded. The record of the e-beam current during this cycle showed a pronounced hysteresis effect. After several evaporation cycles, the tantalum filament was examined and was found to possess an elliptical hole of size (~0.2mm×0.6mm) at its center indicating that ion bombardment had eroded this part of the filament.

To test the hypothesis that the ion bombardment might be responsible for the observed hysteresis effect, a small hole (of area ~1mm^2) was drilled at the center of filament so that majority of the incoming ions could pass through the filament without hitting it. In this case, the hysteresis effect was found to be significantly reduced (see figure 3.3). Similarly, when e-beam was defocused on the target by changing the focusing current so that no evaporation occurs, the hysteresis effect was not observed despite of maximum e-beam power.

For analysis of the above observations, current on the negatively biased (-1 kV) ion collector plate was recorded at different e-beam currents and is shown in figure 3.4. Similarly, the temperature of the e-beam spot area was measured by a TCP at different e-beam powers and is shown in figure 3.5. The plate currents and temperatures showed dependence on e-beam current (or power) only and were independent of the use of a filament with or without a hole.

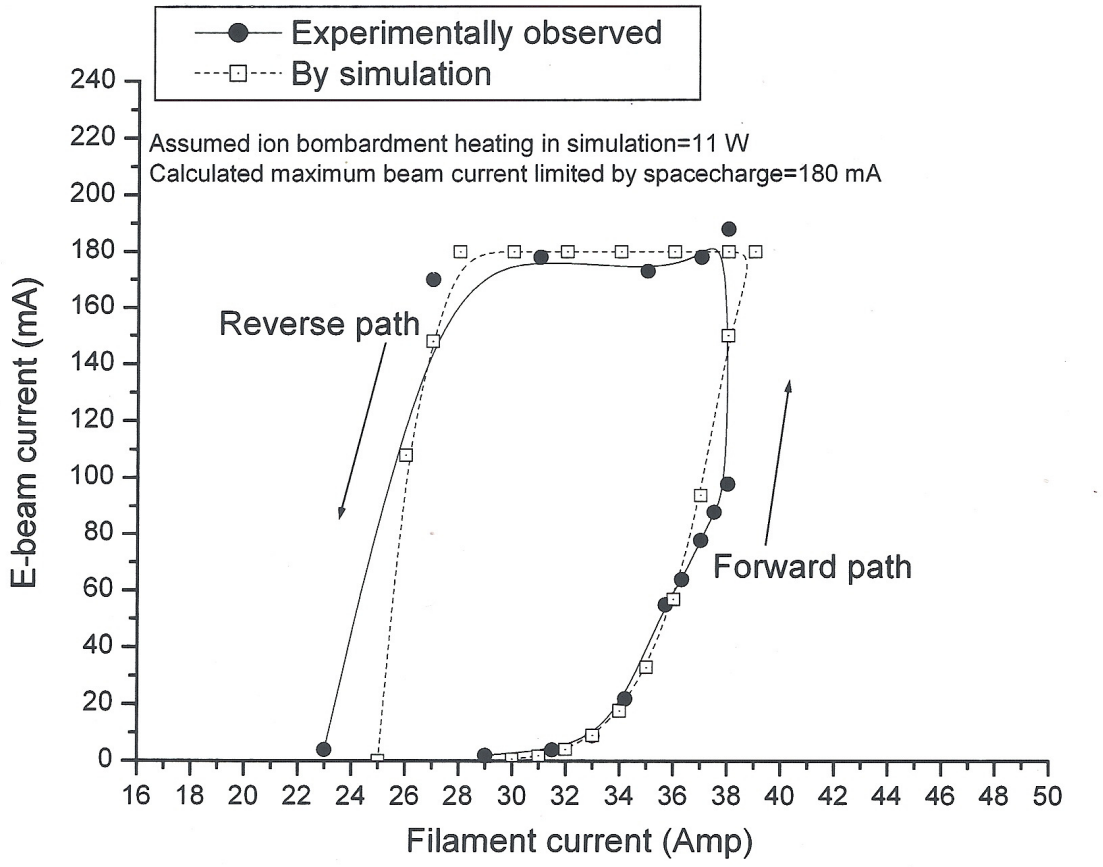

Figure 3.2 Experimental and computer simulated e-beam current with filament heating current when filament without hole was used

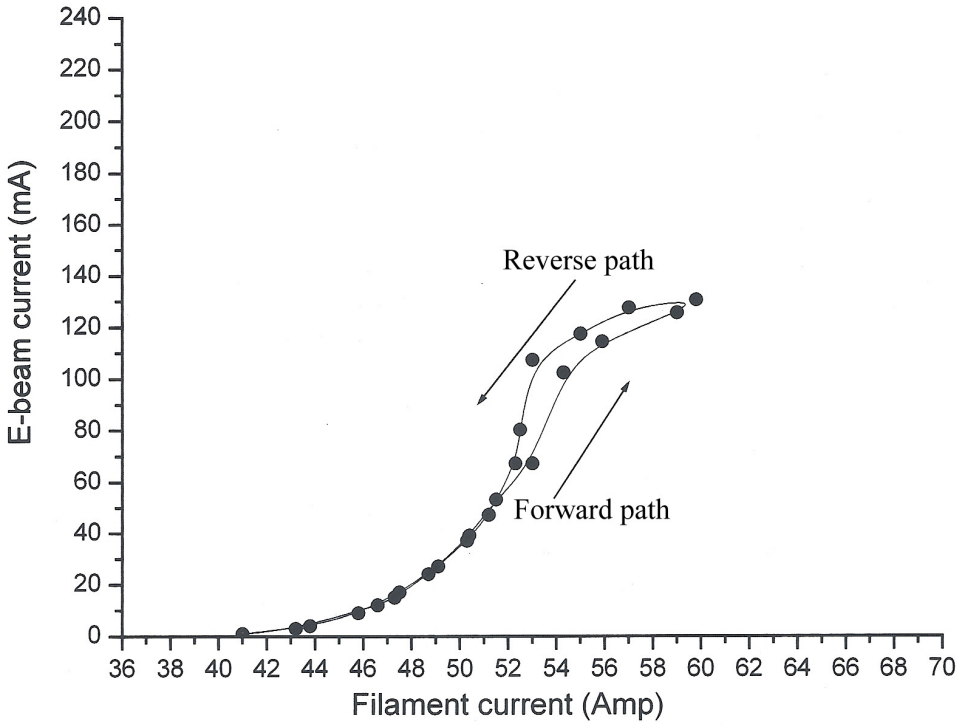

Figure 3.3 Experimentally observed e-beam current with filament heating current when filament with hole was used

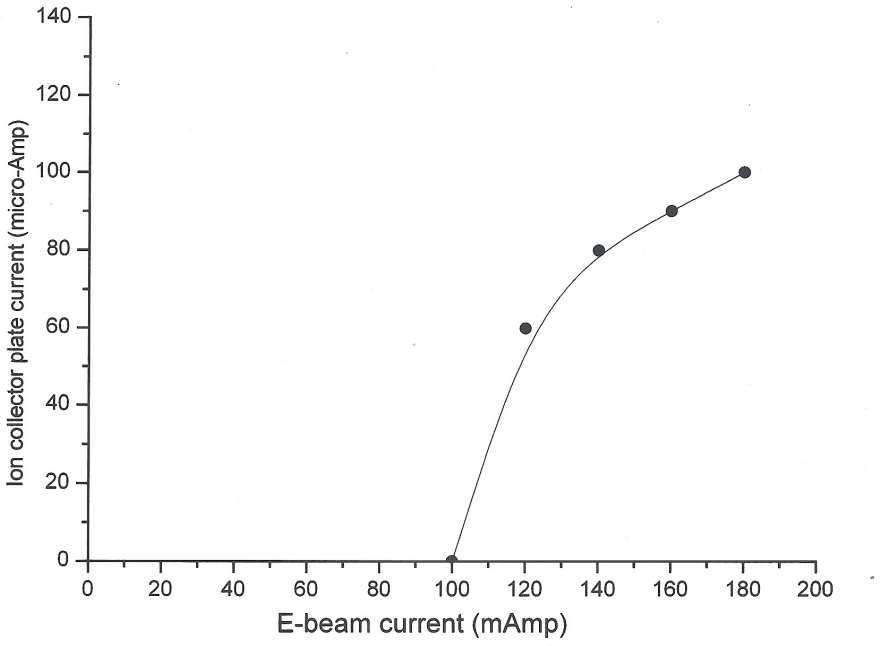

Figure 3.4 Ion collector plate current with e-beam current (plate voltage= -1kV)

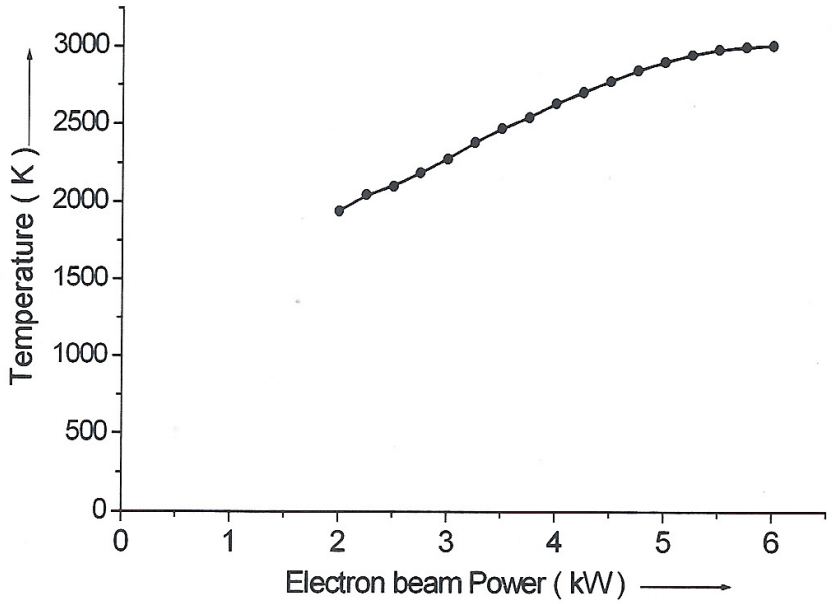

Figure 3.5 Temperature of the hot zone (e-beam spot) vs. e-beam power

3.1.3 Discussions

The first point we need to ensure is attainment of equilibrium temperatures at all the data points of e-beam current vs. filament heating current curve (figure 3.2). Take for example the case of increasing filament heating current from 36 A to 37 A when the e-beam current was experimentally found to be increased from 55mA to 80 mA. At filament heating current ~36A, the heat loss by radiation from the square sized electron-emitting area (~2.6mm×2.6 mm) of filament at temperature ~2450K (calculated from Richardson-Dushman equation for 55mA e-beam current) was ~ 8 W. This is comparable to the rate of ohmic heat generation ~11 W inside the 0.1mm thick filament. So, conduction loss from this small part of the thin filament to supporting structures can be neglected for approximate analysis. Then, the time required for thermodynamic equilibrium of this effective area of filament (i.e. electron emitting region) at any new value of filament heating current, is decided by the additional rate

of ohmic heat generation and its own thermal mass (i.e. mass × specific heat ~ 1.5×10^{-3} J/K). In the case of filament heating current changing from 36A to 37A and for a corresponding increase of e-beam current from 55mA to 80mA, the temperature of the filament needs an increase of ~ 40 K (calculated from Richardson-Dushman equation). The required increase in stored heat content of the effective area of filament is ~0.06 J. This increase in heat content can be achieved in ~0.1s as the extra heat generation rate (ΔI^2R) comes out to be ~ 0.66 W. Thus, the time required for thermodynamic equilibrium of electron-emitting area of filament was of the order of fraction of a second whereas the time provided during experiment to achieve steady state at each step of e-beam current was few minutes. During the reverse direction of change in e-beam current (i.e. from high value of 190mA to 0mA) the speed of change was also slow as the wait period in intermediate steps was also in minutes. Thus, for all the data points, temperature equilibrium of the electron-emitting area of the filament was ensured.

Although thermodynamic equilibrium is achieved in the electron emitting region of filament, if the process of evaporation of metal and subsequent generation of ions (which comes into picture only after ~100mA e-beam current as evident from the detection of ions in collector plates) introduces some extra source for heating of filament, then a completely new equilibrium situation for heat balance in the electron-emitting filament is established. The absence or presence of this extra heating component depending upon direction of change of power (forward or backward) along with inherent space charge characteristics of the e-gun can lead to a bi-stable mode of operation or hysteresis behavior of the e-beam current. To begin the discussion in this line, we first undertake a qualitative discussion of the experimental observations and then proceed to the quantitative analysis of the assumed phenomena.

In the forward direction of e-beam power (figure 3.2), it is seen that the e-beam current increases sharply once it reaches a value of about ~100mA. This is also the e-beam current at which the ion current in the thermal ion collector circuit becomes detectable (figure 3.4). This indicated that the sudden increase in e-beam current is related to generation of ions. Thus, we were led to hypothesize that the ions generated along with the vapor may be moving towards the filament cathode causing additional heating of it and thereby, generating a positive feedback loop. However, the e-beam current did not increase beyond ~190mA as the e-gun goes into space-charge limited mode of operation which was experimentally confirmed by the fact that the beam current remained constant even if filament current was increased and also by the fact that when we increased the voltage, the current increased. To ascertain this quantitatively, space charge limited current was calculated for our geometry using Child-Langmuir law for electron flow between spherical electrodes [35] and it was found to be ~180mA which is close to the experimentally observed saturation beam current in the gun.

In the backward direction of power, as evaporation is already present, the filament has got an additional source of heat (ion bombardment) over and above I^2R heating. Hence, even on decrease of externally supplied filament heating current, temperature remains sufficiently high so that beam current is limited by Child-Langmuir current and not by thermionic emission current. This explains the flat portion of beam current in the backward direction. If we decrease the filament current below a certain limit (I_f =27A), both the modes of heating (I^2R heating and ion bombardment) together are incapable to sustain the thermionic emission current above space charge limited current. So, the gun comes into temperature limited mode and beam current decreases from the saturation value. This in turn reduces the e-beam power on the uranium target and consequently, the vapor flux (or ion flux going towards the cathode). Thus, the ion bombardment on filament also decreases and beam current emitted from cathode further reduces. In this state, as the externally supplied filament current (I_f

=27A) is much below the value needed to maintain same beam current in absence of ion bombardment (i.e. 38A seen from forward path), the ion bombardment contributes a major part in total heating of the filament. So, heating of filament by the ions affects the electron emission from cathode in a very sensitive manner. Hence, the reduction of beam current becomes cumulative and the beam current finally decreases to zero value. This is clearly seen in our experimental observations.

For quantitative confirmation of the above-mentioned phenomena, thermal modeling of the electron-emitting filament was carried out numerically using finite difference method. As the filament was very thin (0.1mm) as compared to its other dimensions, temperature variation along the thickness was neglected. The geometry of the filament used is shown in figure 3.6.

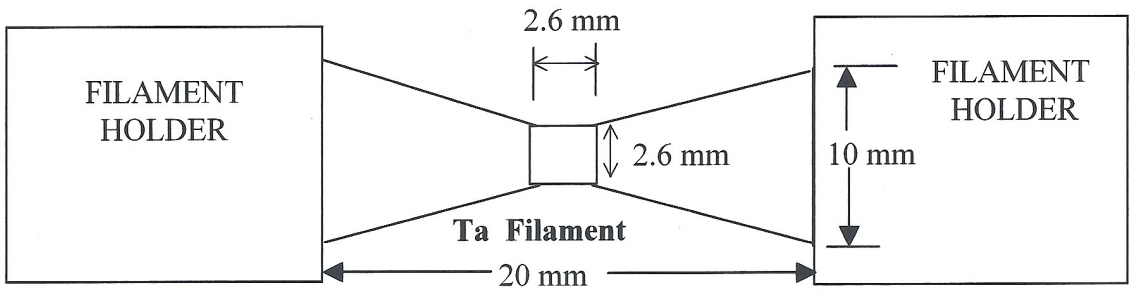

Figure 3.6. Geometry of the electron-emitting filament considered for computer simulation

As a hole on the filament almost eliminated the ion bombardment effect, the area of the hole (~1mm^2) was taken as the area over which bombarding of ions occurs. This area is small owing to focusing action of radially converging electric lines of force from anode to cathode. The temperatures at the two extreme ends of the filament were assumed to be same as the temperature of the filament holder. The total heat input to any small element of the filament was taken to be both due to I^2R heating by filament heating current and ion bombardment depending on its location. Heat loss mechanism from a small element of filament was taken to

be both by conduction to the adjacent elements and also by radiation to the surroundings. Work function [36-37] for tantalum was taken to be 4.35eV and temperature dependant expressions for resistivity [38] and emissivity [38] of tantalum were taken as below,

$\rho = 4.43633 \times 10^{-6} + 4.19442 \times 10^{-8} T - 2.322 \times 10^{-12} T^2$

$\varepsilon = 4.18 \times 10^{-2} + 6.8552 \times 10^{-5} T + 1.32584 \times 10^{-8} T^2$

In the forward direction of e-beam power before evaporation starts, the thermionic emission current calculated in this manner was in very good agreement with the observed beam current (see figure 3.2). This confirmed the correctness of the computer program used for the calculation.

Now, using the thermal model of the filament, the unknown value of heating due to ion bombardment was estimated. As the e-beam current was experimentally found to fall from 180mA to zero at filament current $I_f = 27A$, following condition must hold good so that any decrease in filament current will lead to cumulative reduction of the ion bombardment and consequently the beam to zero value as explained earlier. The condition can be stated as :

Thermionic current from filament at (I_f =27A) due to (I^2R heating + heating by ion bombardment) is just less than the space charge limited current.

The value of heating by ion bombardment which satisfied above condition in the thermal model of filament was found to be about ~ 11 W.

In backward direction, with I_f >28A when ions are generated, the numerically calculated thermionic electron current taking ~11W power addition by ions on filament was found to be much more than the analytically calculated space charge limited current. So, the beam current remains constant at ~180mA in this region (i.e. space charge value). Thus, by using the value of about ~11W power addition to the filament by ion bombardment during evaporation, all the regions of experimental curve could be reproduced theoretically.

To see the possibility of ~11W power addition by ion bombardment in presence of 180mA e-beam current, total number of ions entering the e-beam shielding pipe was estimated. From the temperature vs. e-beam power curve (figure 3.5), it is seen that at I_b~180mA (or power = 5 kW), the temperature is about ~2900K. Using vapor pressure data available in literature [39], atom density ($n = P/kT$) near the source is 2.5×10^{15} no/cm^3. Assuming $1/r^2$ law for variation of atomic flux with distance and cos θ angular distribution, the atomic flux at the entry level of shielding pipe comes out to be ~1.8×10^{17} atoms/cm^2/sec, calculated after taking into account the geometry of shield pipe, temperature and size of hot zone on the target (~7mm diameter). As per published reports [3,4], about ~0.2 % of the e-beam generated uranium vapor is normally ionized. So, ion flux at the entry level of shield pipe is ~60 micro-Amp/cm^2. Multiplying this to cross sectional area (20 cm^2) of the pipe, total ion current entering the pipe was ~1.2mA. An enhanced entry of ions through the anode hole as compared to the probability decided by its geometry is expected due to leakage of the electric field lines of force from cathode through the anode hole and a negative potential well formed by e-beam (whose potential at center comes out to be about ~200 V for a current density of 0.1A/cm^2 at 28keV energy). So, to get an idea about the order of the heat addition, a 2-D plasma simulation by particle-in-cell (PIC) method [40] was carried out which predicted that for a geometrically equivalent 2-D situation, about 30% of the ions that have entered the e-beam shielding pipe passes through the anode hole and rest is collected on the walls of the shielding pipe. Thus, the heat addition due to ion bombardment is given by,

$$Q = 30\% \times \text{Ion current at entry of pipe} \times \text{Energy gain between cathode and anode gap}$$

$$= 0.3 \times 1.2 \text{ mA} \times 28 \text{ kV} \approx 10 \text{ W}$$

As this estimated value of heat addition is of the same order as the amount of extra heat indicated in the experimental observations, it was concluded that the amount of ion bombardment indicated by the experiment was indeed possible.

Finally, other effects that might contribute for enhanced electron emission were investigated. For instance, when ions bombard the filament cathode, an image current of electrons [8] come to the surface for neutralization of ions by which I^2R heating of the filament might increase. But, we have seen the ion current hitting the cathode is about ~0.3×1.2=0.36mA where as the heating current of the filament is about 40A. So this effect can well be neglected.

Similarly, during bombardment of ions at 30keV energy on the filament, secondary electrons are released. However as the secondary electron yield from tantalum [41] for heavy ion bombardment is less than 0.5, the extra current due to this process for an ion bombardment current of 0.36mA will be less than 0.2mA. So, e-beam current enhancement due to this was neglected.

We also examined the possibility of thermo-field emission [42] (Schottkey effect) in electron current enhancement due to presence of an ion cloud in front of the cathode while using a filament without hole. The maximum possible additional electron emission due to thermo-field effect was calculated for the case when ~0.36mA ion current hit the cathode at 28kV energy concentrated on an area of ~1mm^2 on the basis of which experimental observations had been explained. When uranium ions bombard on the surface of tantalum filament, some of the atoms of tantalum are sputtered. Using the values of sputtering yield ~5 available in literature [38] for the case when heavy ions bombard tantalum surface, tantalum atomic flux comes out to be ~ 1.1×10^{18} atoms/cm^2/sec or atomic density is ~ 3.3×10^{12} atoms/cm^3 assuming energy of sputtered atoms [43] is 10eV. As the heat transfer model of the filament had revealed that the temperature at the point of ion bombardment within the range of variation of filament current, was much less than the temperature for melting of tantalum, thermal evaporation of tantalum is negligible. To calculate the upper limit of electric field, we assumed that all the sputtered atoms are ionized by the accelerated thermionic electrons

(~90% ionization reported in literature [8]).This occurs at a distance of 50 micro-meter as at this distance in our case, kinetic energy of the thermionic electrons reaches ~100eV at which ionization cross section is maximum [8]. Thus, we see a tantalum ion cloud being generated at a distance of ~50 micro-meter with density ~3.3×10^{12} ions/cm^3. As the ions return back to the cathode with more and more velocity, their density will decrease to ~1×10^{12} ions/cm^3 when kinetic energy is 100eV. Thus the average tantalum ion density is ~2.2×10^{12} ions/cm^3 over a thickness of 50 micro-meter. The calculated incident uranium ion density ~10^{10} ions/cm^3 in front the cathode is negligible as compared to average tantalum ion density ~2.2×10^{12} ions/cm^3. Thus, the additional electric field due to tantalum ion cloud whose thickness is small as compared to the other dimensions of the cathode can be found out by using the Gauss's Law of electrostatics for the case of sheet of charge in front of a conducting plane i.e.

$$E = \text{Charge density per unit area}/ (2\varepsilon_0)$$

$$= \text{Ion density} \times \text{thickness} \times e / (2\varepsilon_0)$$

$$= 1\times 10^6 \text{ V/m}$$

Where e= electronic charge, ε_0 = Permitivity of space.

As this calculated electric field is much lower than the required [1,8] value of electric field ~10^7-10^8 V/m when thermo-field effect (or Schottkey effect) becomes detectable, the possibility of field emission effect is ruled out.

3.1.4 Conclusion :

Deposition of heat by ion bombardment on the filament was the sole effective reason for the observed hysteresis effect of e-beam current. By making a hole of area ~ 1 mm^2 on the filament, collision of the ions with the filament was avoided at least at the center and hysteresis effect could be reduced significantly which is clear from figure 3.3.

3.2 Electrical Discharges and protection:

Although high vacuum of the order of ~10^{-5} mbar or better is normally maintained in e-beam evaporation systems, due to local outgassing of trapped gases from the metallic components, insulators and the target being melted, the pressure in the cathode-anode gap (~1cm) may temporarily reach a value of ~10^{-3} mbar for a few milliseconds. At this pressure, breakdown strength of the gap becomes minimum as observed from Paschen curve resulting in electrical discharge between the cathode and anode. To take care of the above difficulty, the HVDC power supply used for e-guns needs a very sensitive protection circuit, which can detect a spark and immediately reduce the voltage so that damages to the cathode, anode and power supply are avoided. Spark detection is normally achieved by continually monitoring the rate of rise of current from the power supply. In addition to this, during the mechanical design of e-gun, care is taken so that sufficient pumping paths are available in all directions and insulators are of superior quality having minimum outgassing properties. In the initial run, temperature of the target is increased very slowly because maximum outgassing occurs during melting of the target for the first time.

In addition to this, some important modifications had to be carried out in the harmonics filter circuit of power supply to protect it from transients. After analysis we concluded that there should be no inductor L_2 after the capacitor as shown in figure 3.7. Although this inductor appears to limit the transient discharge current, this can cause serious problem during quenching of the discharge. As generally the discharges occur during short local outburst of gases, the pressure can improve suddenly to 10^{-5} mbar due to high pumping speed of the vacuum systems. Thus discharge is quenched immediately. However, by this time the inductor already carries current of $I=V/R$ (where V is operating voltage) storing energy given by $E=(1/2)L_2I^2$. Upon quenching of discharge current, this energy is transferred

to the capacitance given by series combination of capacitance between cathode and anode C_p and C. Thus, maximum value of transient voltage across cathode-anode gap is calculated by,

Energy stored in inductor during maximum discharge current

= Energy stored in capacitors after quenching of discharge

$$\frac{1}{2}L_2\left(\frac{V}{R}\right)^2 = \frac{1}{2}\left(\frac{CC_p}{C+C_p}\right)\left(\frac{C+C_p}{C}\right)^2 V_p^2 \qquad [\ V_p \text{ is voltage across } C_p\ ]$$

$$V_p = \sqrt{\frac{L_2 C}{C_p(C+C_p)}} \cdot \left(\frac{V}{R}\right)$$

Or $$V_p \approx \sqrt{\frac{L_2}{C_p}} \cdot \left(\frac{V}{R}\right) \qquad (\text{as } C_p << C \text{ by about five orders of magnitude})$$

Putting typical values V=30kV, R=1000 Ohm, L_2= 50mH, C=1 microfarad and $C_p = \varepsilon A/d$ = 1 Pico-farad (assuming cathode and beam shaping electrode area as 10cm^2 and cathode-anode gap of 1cm), we get, V_p = 6.7 MV

Thus, very high transient voltages are generated which can be transmitted to the power supply control circuit through the feedback and in some cases as EMI (Electro Magnetic Interference). Considering the above phenomena, we have carefully selected the filter components in the power supply of e-gun.

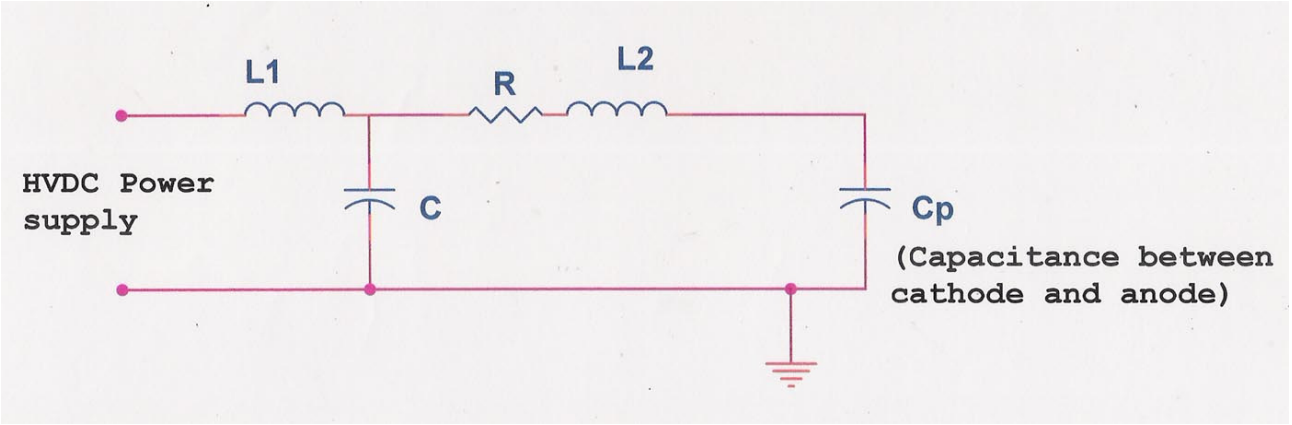

Figure 3.7 Conventional harmonics filter and current limiting circuit of e-gun power supply

CHAPTER – 4

Process Monitoring

4.1 Difficulties in temperature measurement of a vapor source and A novel solution

In e-beam evaporation process, temperature of the hot zone created by the e-beam is normally measured by optical pyrometry using a SCP or TCP. Whatever be the selected pyrometer, the change of spectral emissivity of the source with temperature [44] and transmission of the optical path have to be taken into account which otherwise can lead to large errors in the measured temperatures. The pyrometer view path can be direct [45] through a glass window in the vacuum chamber or indirect [9-12] through a periscope like arrangement, which employs a process-generated mirror that forms on an inclined glass slide by deposition of metal vapor. The direct view method does not permit continuous monitoring as the glass window becomes opaque due to coating of metal vapor on it within few seconds of observation. A shutter is often used to record a few samples of temperature data during the evaporation process, but it does not permit continuous monitoring. However, periscopic method offers continuous monitoring. In this arrangement, if a SCP is used as temperature sensor, correction has to be applied to the measured temperature taking into account both the absolute value of emmisivity of source and reflectivity of the dynamically generated thin film mirror. Although temperature dependant emissivity of source may be found experimentally or from literature [46-47] at some temperatures and wavelengths, absolute value of reflectivity of the thin film mirror is problematic due to its dynamic and system specific nature depending upon the extent of surface oxidation (pressure level), rate of deposition and thickness. But, if a TCP is used as temperature sensor in the periscopic arrangement and if (at least for some metals) the ratio of spectral reflectivities of the thin film mirror at monitor wavelengths is one

despite of dynamically changing absolute value of reflectivity, then the contribution of error from thin film mirror can be avoided. So, to quantify the sources of error in measured temperature of the vapor source generated by e-beam heating in periscope method, we have recorded the data using both the methods viz. direct view method and periscopic method for different materials viz. Cu, Al and Zr. The directions of errors (+ve or –ve) are understood from the spectral properties of process generated thin film mirror. Finally, a novel method is proposed in which additional error introduced by the periscopic method can be avoided and yet, continuous monitoring of the temperature of e-beam spot can carried out for hours.

4.1.1 Experiment for recording the temperature of e-beam spot:

The experimental system (figure 4.1) consists of a vacuum chamber in which background pressure is maintained at a level better than ~10^{-5} mbar through out the process. A transverse type e-gun (10 kV, 0.8 A) was used to bombard the metal target placed in a water-cooled copper crucible. The e-beam power was varied by changing the filament heating current to meet the power requirements for different target materials. Depending on the thermo-physical properties of the chosen target, temperature of the e-beam spot at the centre of target surface can reach a value up-to 3500 ^{0}C. Diameter of the target surface is 60 mm and e-beam spot is an elliptical area of 10 mm × 6 mm. Due to presence of the water cooled copper crucible within which the target is placed, the outer portion of the target remains solid and acts as a skull surrounding the liquid metal pool at the center. The temperature gradually decreases from the boundary of the e-beam spot to the boundary of melt pool whose diameter is approximately ~30 mm to 40 mm depending upon material of the target.

To monitor this temperature, both a direct view port through a glass window and a periscope arrangement using a process generated thin film mirror were installed. The temperature-measuring device was a commercial TCP (Model PZ40, Keller GMBH,

Germany) with a range of 800 ^{0}C to 3500 ^{0}C. The monitor wavelengths of the pyrometer are 950 nm and 1050 nm and as per the technical specification of the manufacturer, the accuracy of instrument is 1% for a black body or gray body source within the above mentioned temperature range. Spectral bandwidth at lower monitor wavelength is from 780 nm to 1060 nm and at higher monitor wavelength is 985 nm to 1100 nm. The distance ratio of the pyrometer was 150 :1 and so by keeping the pyrometer at a distance of 800 mm from source, the viewing zone of the pyrometer could well be filled completely by the e-beam spot area where temperature is reasonably uniform. The pyrometer was connected to personal computer for data storage and analysis.

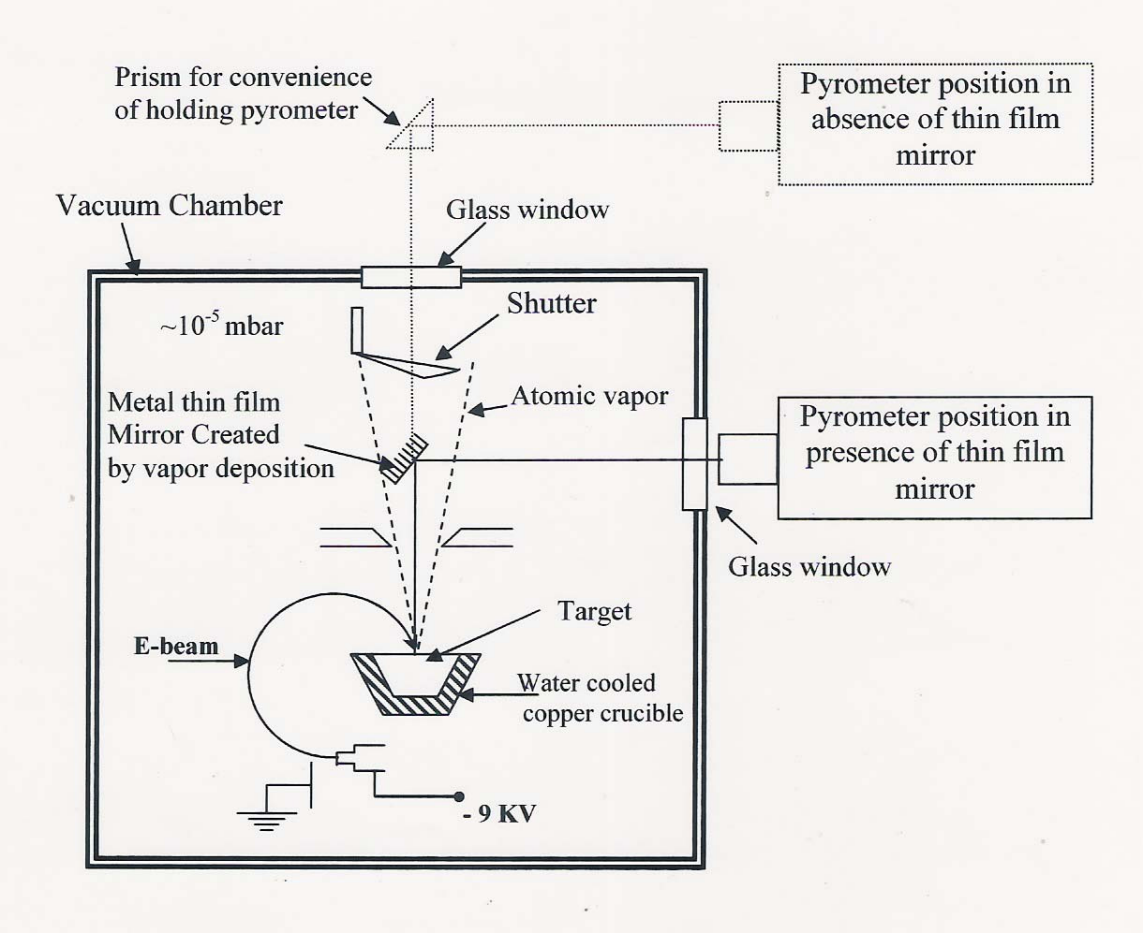

Figure 4.1 Schematic of the experimental Set-up for monitoring of temperature

To begin with, Zr was chosen as the evaporant and temperature vs. e-beam power data was taken through the periscopic arrangement. The periscope arrangement was then removed and the same exercise was done by directly viewing the source through a quartz glass window. For, convenience, a quartz prism was placed outside the direct-view window to turn the light beam along horizontal direction so that the horizontally placed pyrometer can receive the light. A shutter was used to minimize the exposure time of the glass window to the atomic vapor beam. Typical exposure time for a single observation of temperature was less than ~5 sec. Due to observation of temperatures at 5 to 6 different e-beam powers, the total thickness of the deposited layer on the quartz window was expected to be in the range of ~0.5nm to ~1nm. To verify that this layer does not affect temperature measurement, the transmitivity through this coated window was measured by a spectrophotometer in the wavelength range that contains both the monitor wavelengths of the two-color pyrometer. It was experimentally confirmed that the attenuation of light by the extremely thin coating on the direct view port was less than ~1% and this should not affect the temperature readings obtained. The same procedure was repeated for two more metals; Al and Cu.

For the three metals i.e. Zr, Al and Cu, the temperature vs. e-beam power as recorded by direct view and periscopic method are shown in figure 4.2, 4.3 and 4.4 respectively. To understand the discrepancies in temperature readings, we removed the thin film mirrors in all the three cases and obtained their spectral reflectivity in the wavelength range that contains both the monitor wavelengths of the TCP by a spectro-photometer while ensuring that the incidence angle of light at the thin film mirror is 45^0 as in our experimental set-up. This information is given in figure 4.5.

The bars in the temperature data shown in the figure 4.2, 4.3 and 4.4 are the online fluctuations in temperature as recorded by the computer. The fluctuations shown in figures are not statistical uncertainty of measurement but they are the actual temperature variations of e-

beam generated vapor source due to its own inherent nature [48]. Existence of high rate of convection current [49] and turbulent flow [50] within the melt pool of the target causes the variation in source temperature by random mixing of the hot fluid at the center with the colder fluid coming from peripheral region of the melt pool. These fluctuations in temperatures were there in all the four set of measurement data we have taken. The error due to absorption and emission of light by the vapor is negligible as the density of vapor is low (vapor pressure ~ 5 mbar) and as seen from literature [51], these atoms don't have any strong absorption /emission frequencies near the pyrometer monitor wavelengths.

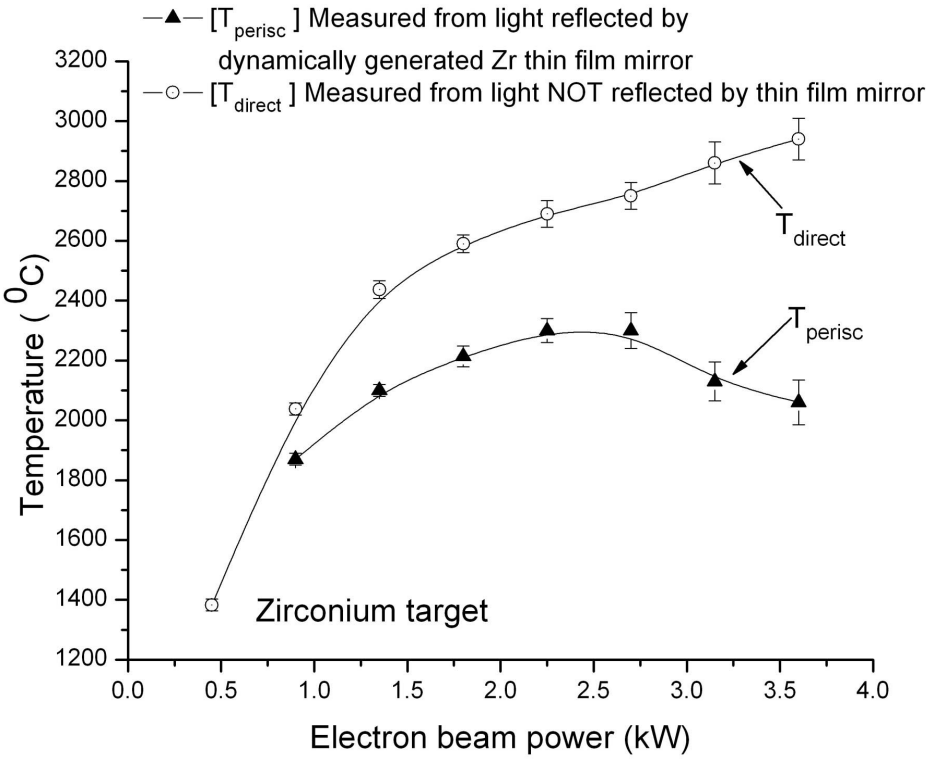

Figure 4.2. Temperature of e-beam heated Zr vapor source as measured by periscopic method and direct viewing method

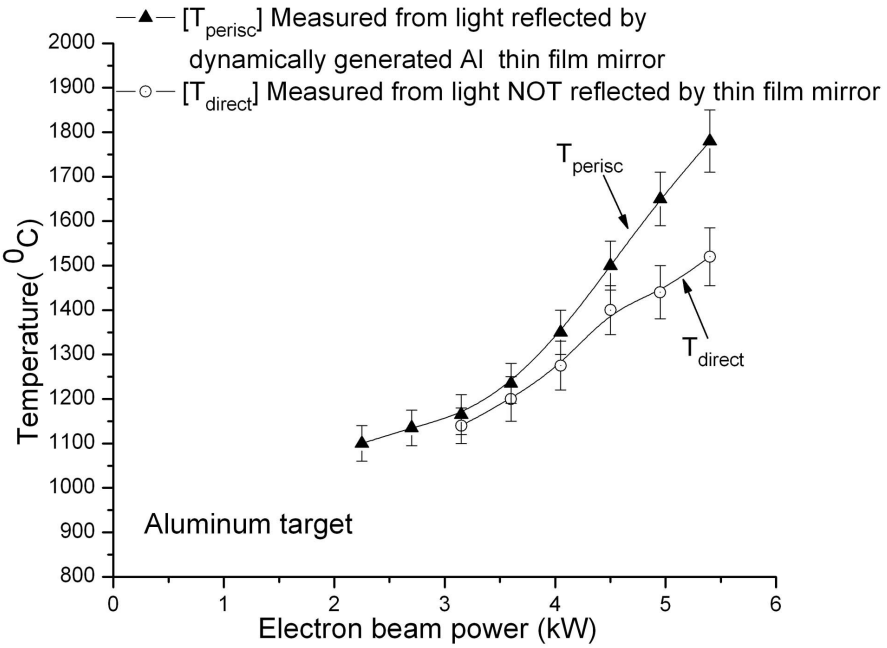

Figure 4.3. Temperature of e-beam heated Al vapor source as measured by periscopic method and direct viewing method

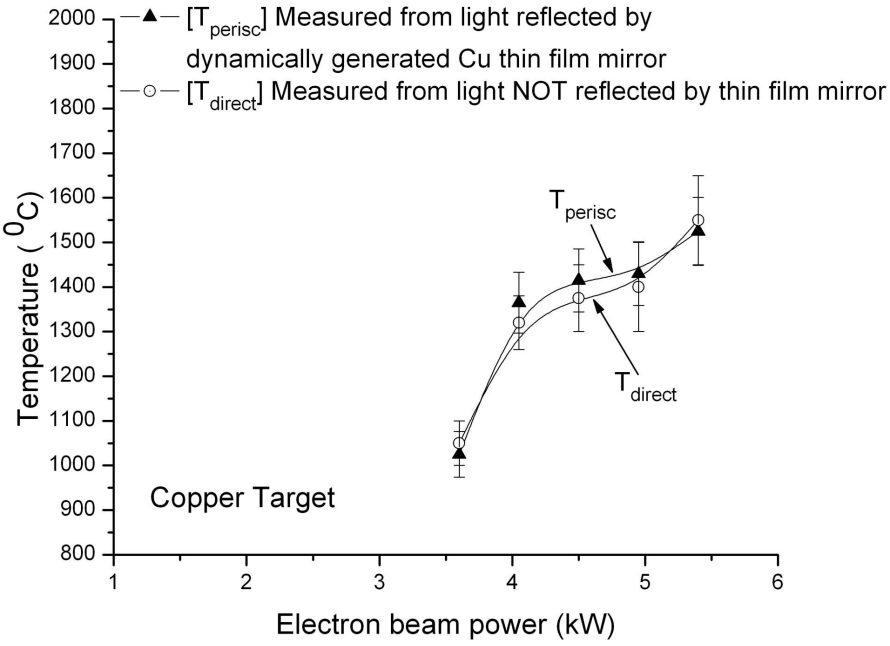

Figure 4.4. Temperature of e-beam heated Cu vapor source as measured by periscopic method and direct viewing method

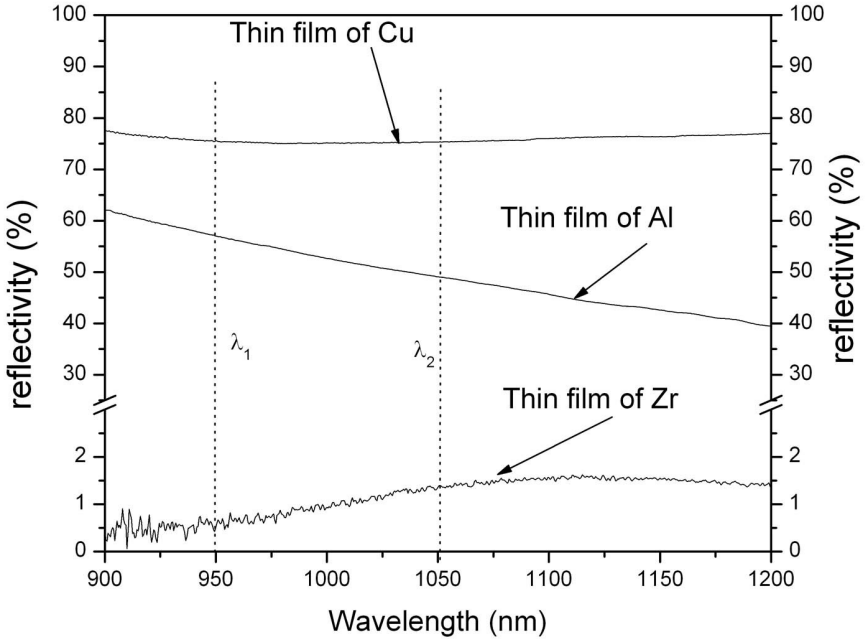

Figure 4.5 Reflectivity of process generated thin film mirrors measured by spectro-photometer

4.1.2 Results and Discussions :

In periscopic method, the optical property of the process generated thin film mirror in the transmission path of light can have profound effect on the measured temperature. The reflectivity of the metal thin films are expected to change during vacuum deposition due to partial oxidation as the thin films of metals like Zr and Al are oxidized up-to a thickness of few atomic layers at pressure ~10^{-5} mbar in ~5-10 minutes [52-56] which is of the same order as the time elapsed during our experimental measurements. Although in-situ reflectivity of process generated thin films with partial oxidation presents a complex dynamically changing scenario that depends on several parameters viz. thermo-physical properties, oxygen partial pressure, oxidation kinetics and properties of resulting oxides etc., we tried to correlate the observed trends in our experimental data for different metals.

From the figure 4.2 to 4.4, it was found that the difference between the temperature readings of direct view method and periscopic method were higher for Zr and Al and it was very much less for Cu. Another salient point is that temperature measured by periscopic method is underestimated for Zr ($T_{perisc} < T_{direct}$) and overestimated for Al ($T_{perisc} > T_{direct}$) as compared to the temperature recorded by direct view method. This indicates that the process generated thin film mirror can introduce error in both the directions depending upon the slope of the reflectivity curve. To ascertain the above facts in our experimental data, we begin with the Wien's expression (neglecting '1' in Planks's law) that is used by the digital circuit of the TCP to calculate the true temperature 'T_{true}',

$$\frac{V_1}{V_2} = \frac{S_1\ \varepsilon_1(T_{true})\ R_1}{S_2\ \varepsilon_2(T_{true})\ R_2}\left(\frac{\lambda_2}{\lambda_1}\right)^5 e^{\frac{c_2}{T_{true}}\left(\frac{\lambda_1-\lambda_2}{\lambda_1\lambda_2}\right)} \tag{4.1}$$

where, V_1 *and* V_2 = Detector output voltages at monitor wavelengths λ_1 and λ_2

S_1 *and* S_2 = Detector sensitivities including the effects of filters and internal optics of the pyrometer at wavelengths λ_1 and λ_2

$\varepsilon_1(T_{true})$ *and* $\varepsilon_2(T_{true})$ = Spectral emissivity of the source at wavelengths λ_1 and λ_2 at source temperature 'T_{true}'

R_1 *and* R_2 = Reflectivity of process generated thin film mirror at wavelengths λ_1 and λ_2

C_2 = Plank's second constant $=1.4387752 \times 10^{-2}$ m-K.

The pyrometer sends the digital signals of detectors V_1 and V_2 to the computer and the computer program (supplied by manufacturer) can calculate the true temperature by solving Eq. (4.1) using these values and $\left(\frac{S_1}{S_2}\right)$ as set during calibration of the instrument provided the user feeds the correct value of $\left(\frac{\varepsilon_1 R_1}{\varepsilon_2 R_2}\right)$ to it. However, if we incorrectly provide the

pyrometer program a value of '1' for the term $\left(\frac{\varepsilon_1 R_1}{\varepsilon_2 R_2}\right)$, the pyrometer program will use the same detector output voltages but will give us the incorrect temperature 'T_{perisc}' given by,

$$\frac{V_1}{V_2} = \frac{S_1}{S_2}\left(\frac{\lambda_2}{\lambda_1}\right)^5 e^{\frac{c_2}{T_{perisc}}\left(\frac{\lambda_1-\lambda_2}{\lambda_1\lambda_2}\right)} \tag{4.2}$$

Dividing Eq. (4.1) and (4.2), we get the relation between temperature T_{perisc} and T_{true} as,

$$\frac{1}{T_{true}} = \frac{1}{T_{perisc}} + \frac{\lambda_1\lambda_2}{c_2(\lambda_1-\lambda_2)}\left[\ln\left(\frac{\varepsilon_2(T_{true})}{\varepsilon_1(T_{true})}\right) + \ln\left(\frac{R_2}{R_1}\right)\right] \tag{4.3}$$

We see that two additional correction terms needs to be added to know the true temperature of the source. Similarly in case of direct view method, the form of correction equation will be same except that term $\left(\frac{R_2}{R_1}\right)$ will not be there. So,

$$\frac{1}{T_{true}} = \frac{1}{T_{direct}} + \frac{\lambda_1\lambda_2}{c_2(\lambda_1-\lambda_2)}\left[\ln\left(\frac{\varepsilon_2(T_{true})}{\varepsilon_1(T_{true})}\right)\right] \tag{4.4}$$

Subtracting Eq. (4.4) from Eq. (4.3) and simplifying,

$$T_{perisc} - T_{direct} = \frac{\lambda_1\lambda_2 T_{perisc} T_{direct}}{c_2(\lambda_1-\lambda_2)}\left[\ln\left(\frac{R_2}{R_1}\right)\right] \tag{4.5}$$

It is to be noted here that R_1 and R_2 are reflectivity of thin film mirrors during the process of evaporation while they are inside the vacuum chamber. However, the reflectivitiy vs. wavelength characteristics shown in figure 4.5 is the thin film property after exposing the vacuum deposited film to normal atmosphere for measurement by the spectro-photometer. It is for this reason that we don't attempt exact quantitative estimation of the reflectivity but predict only about the expected slope of reflectivity curve from measured temperature data.

Now we put numerical values λ_1=950 nm and λ_2 = 1050 nm in Eq. (4.5).

For the case of Zr from figure 4.2, $T_{perisc} < T_{direct}$. So, left hand side of Eq. (4.5) becomes negative resulting in, $R_2 > R_1$. This predicts a positive slope of reflectivity curve for the process generated Zr thin film mirror. Our experimentally observed reflectivity curve (figure 4.5) agrees well with this prediction. Similarly, as $T_{perisc} > T_{direct}$ in case of Al (from figure 4.3), Eq. (4.5) results in, $R_2 < R_1$. This predicts a negative slope of reflectivity curve for the process generated Al thin film mirror. Our experimentally observed reflectivity curve (figure 4.5) also agrees with this prediction. In case of copper (figure 4.4) $T_{perisc} = T_{direct}$ and so, R_2 is expected to be nearly equal to R_1 which is again clear in figure 4.5.

The fact that the difference between the temperature measured by periscopic method and direct method, increases monotonically with the temperature of the source in case of both Zr and Al (figure 4.2 and 4.3) can be understood by analyzing the Eq. (4.5) where we see that the difference is directly proportional to the product of two temperatures and logarithm of ratio of reflectivities. So, the difference should increase with source temperature which we clearly find in our results. In addition to this, the larger error in temperature for Zr as compared to Al at their highest e-beam powers (3.6kW and 5.6kW respectively) can be understood by considering the fact that at those powers, Zr target was at much higher temperature than that of Al target (about 2 times).

One of the possible reasons for non-zero slope of the reflectivity curve for metals like Zr and Al might be their capability to form oxides in high vacuum environment and thin films of metal oxides normally show this type of behavior. During oxidation by one mole of O_2, the change in Gibb's free energy for copper is ~256 kJ which is much less than that for Al and Zr i.e. ~1055 kJ and ~1100 kJ respectively [57-58]. Thus, Zr and Al are much more reactive than Cu. This explains the increasing/decreasing reflectivity curve for Zr and Al and relatively flat curve for Cu in figure 4.5.

4.1.3 A novel method for Continuous and accurate Monitoring of temperature:

To summarize, the direct view method, though can be made accurate, does not afford continuous measurement and periscopic method, though continuous, suffers from an additional error in cases where the metals are reactive. This made us look for a solution that offers both accuracy and continuity. In an effort to find such a solution, the root cause of the problem was analyzed. Since, the atomic vapor co-propagates along with the light, during measurement of temperature by directly viewing, this vapor gets coated on the glass window causing opacity. Both the light photons and atoms being electrically neutral, there is no electrical or magnetic method to collect only the photons while rejecting the atoms. Separation is however possible on account of vast difference in the velocity of propagation of atoms and light. So, a rotating cylindrical fin structure (as shown in figure 4.6) was proposed

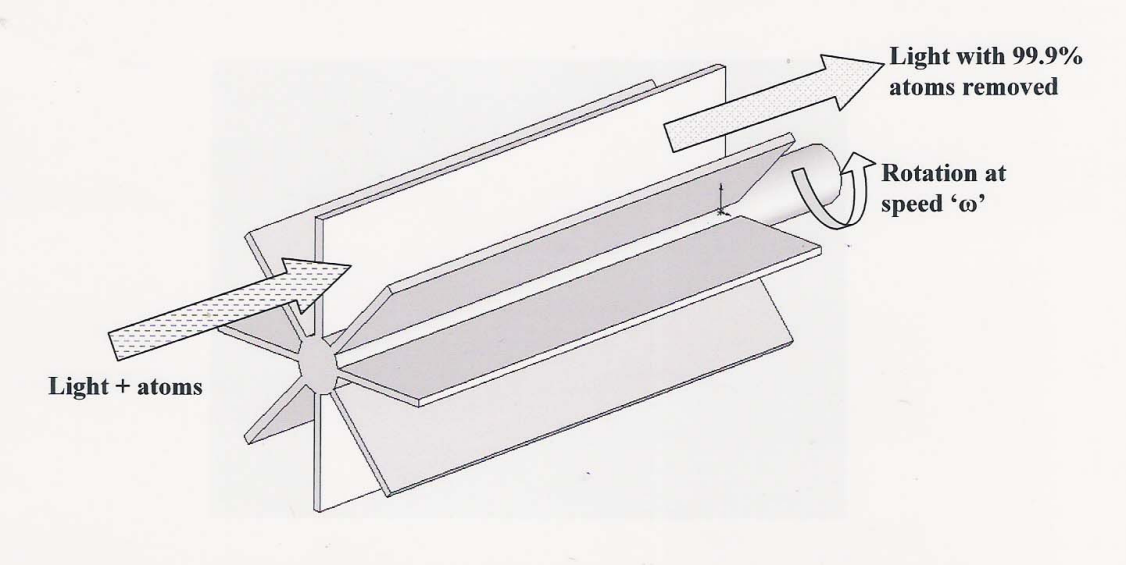

Figure 4.6 Schematic of rotating fin structure for removal of atomic vapor from incoming light being monitored

which can remove 99.9% atoms while reducing the intensity of the incoming light by less than 10%. As we are measuring the temperature by two color pyrometer, this reduction in

intensity will not affect the ratio of intensities and hence, the measured temperature of the vapor source. In this scheme, the rotating cylindrical fin structure is placed in the path of light coming from the vapor source. Due to high speed of the rotating fins that is comparable with the speed of atoms, these atoms are collected on the fins (assuming sticking coefficient to be unity) where as photons of the light escape with negligible reduction (velocity of light is larger by a factor of ~3×10^5). An estimate of the required angular speed of rotor to do this can be found as follows;

Let L = Length of the fins in mm, N = Number of fins, d = Thickness of each fin mm,

R = Distance of the light/atom beam from axis of rotation in mm

ω = Rotating speed of the cylinder in rps, v = Velocity of atoms in m/sec

Average distance between vapor column and nearby advancing fin

$$= \frac{Gap\ between\ two\ adjacent\ fins}{2} = \frac{2\pi R - Nd}{2N}$$

Average time required by the fin to collide with atoms in vapor column

$$t_s = \frac{Average\ distance\ from\ vapor\ column}{Linear\ speed\ of\ fin} = \frac{2\pi R - Nd}{2N\omega R}$$

Transit time of the atoms with velocity 'v' through the fins is, $t_t = \frac{L}{v}$

So, all the atoms for which transit time 't_t' is more than 't_s' will be collected by the fins.

i.e. $t_t > t_s$ => $\frac{L}{v} > \frac{2\pi R - Nd}{2N\omega \mathrm{R}}$

$$\Rightarrow \quad v < \frac{2N\omega RL}{2\pi R - Nd} \tag{4.6}$$

Thus, all the atoms which satisfy above relation given by Eq. (4.6) are removed from the view path. Assuming Maxwell- Boltzmann distribution for atoms at temperature 'T' of the vapor source, percentage of the atoms collected by the fins is given by,

$$\eta = 100 \times \frac{\int_0^{\frac{2N\omega RL}{2\pi R - Nd}} v^2 e^{-mv^2/2kT} dv}{\int_0^{\infty} v^2 e^{-mv^2/2kT} dv} \quad \% \qquad (4.7)$$

For Zr vapor source at temperature = 3000 K, putting typical values normally possible to achieve in a laboratory, i.e. L=100 mm, ω=833rps (50000rpm), R=50 mm, N=70, d=0.5 mm, we get from Eq. (4.7), η= 99.9%.

We see that it is possible to remove 99.9% atoms from the light coming from the vapor source as a result of which vapor coating can be avoided in the intermediate vacuum window. In this way, the time period of temperature measurement by directly viewing the e-beam spot can be increased by 1000 times or in other words, from few seconds to few hours.

4.1.4 Conclusion:

It was experimentally found that errors in temperature measured in periscopic method can be as high as 35% especially for reactive metals and it can be in both directions (positive or negative). The direction of errors could be theoretically explained. Finally, for continuous and accurate measurement of temperature of hot zone, a novel method was proposed and it was mathematically proved that this method can avoid errors experienced in the periscopic method and yet can extend the continuous monitoring time by a factor of ~1000 from few seconds to few hours.

4.2 Monitoring of evaporation rate and atom density:

Rate of evaporation from the target during e-beam heating needs to be monitored for controlled deposition of thin films. Although for thick films, off-line method such as deposition on a sample of substrate for a specified time can be useful, for production of thin films of accurate thickness, on line method of monitoring the vapor flux is essential. One such online method is quartz crystal thickness monitor and another is spectroscopic absorption technique. These online signals for atom density or flux can serve as a feedback signal for control of heating current of the electron emitting filament and thus ultimately controlling the e-beam current and rate of evaporation of target material. Details of these techniques are given in the following sections.

4.2.1 Quartz crystal thickness monitor

In a quartz crystal thickness monitor, thickness is calculated on line by finding the resonant frequency of vibration of piezoelectric crystal through RF electrical circuit. We have used such a thickness monitor to measure the rate of evaporation at different e-beam powers while using Al, Cu and Zr as targets. The results are given in figure 4.7.

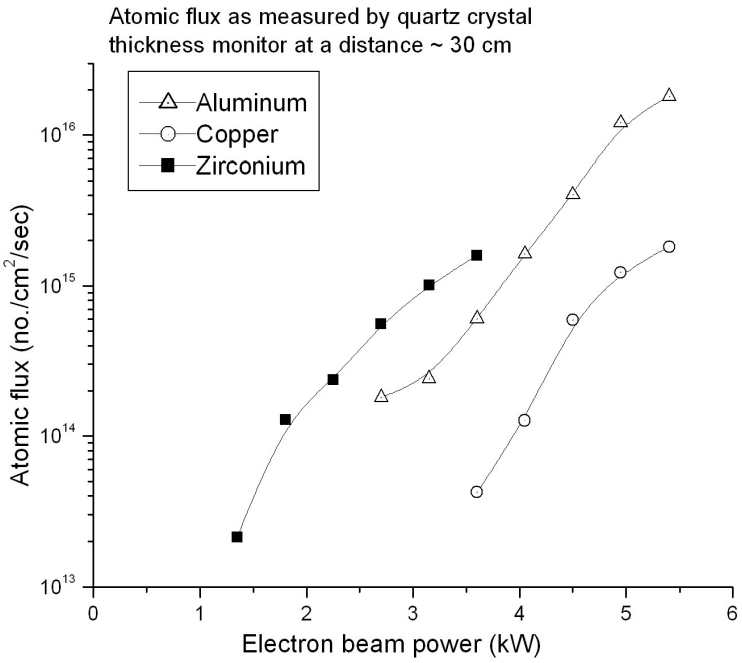

Figure 4.7 Atomic vapor flux of Al, Cu ad Zr as measured by aquartz crystal thickness monitor

4.2.2 Spectroscopic absorption technique:

The spectroscopic absorption technique is another on-line method for measurement atom density, which has more advantages over the piezoelectric sensor. These are,

a) It is non-intrusive i.e. measurement setup can be kept outside the vacuum chamber only a with facility for passage of light through the vapor
b) It can work for indefinite time as the problems like overloading of the sensor due to vapor deposition does not arise in this case.
c) It can be used for atomic state sensitive measurement populations such as density in ground state and metastable states

We have used such a spectroscopic absorption technique for measurement of atom density of uranium in ground and higher metastable states like 620cm^{-1} and 3800cm^{-1}. In this experiment (figure 4.8), a HCDL was used as light source for absorption spectroscopy. The light from the

lamp was collimated with the help of lenses. Two collinear circular apertures (diameter~5mm) were used for adjusting the diameter and path of this light. The transmitted light through the vapor column was focused onto the slit of the monochromator by another lens. For recording the absorption signals at emission lines of the uranium HCDL (as given in table 1), the monochromator was tuned to a wavelength and signal intensity was measured with and without the atomic beam in optical path between the lamp and the monochromator. The emission lines at the above mentioned wavelengths were chosen because they had relatively higher cross section for interaction with the vapor. Further, the magnitude of background signal was estimated by scanning the monochromator on either side of emission line. On subtraction of the background signal from the signal intensities in each case, actual signals of the emission lines were determined.

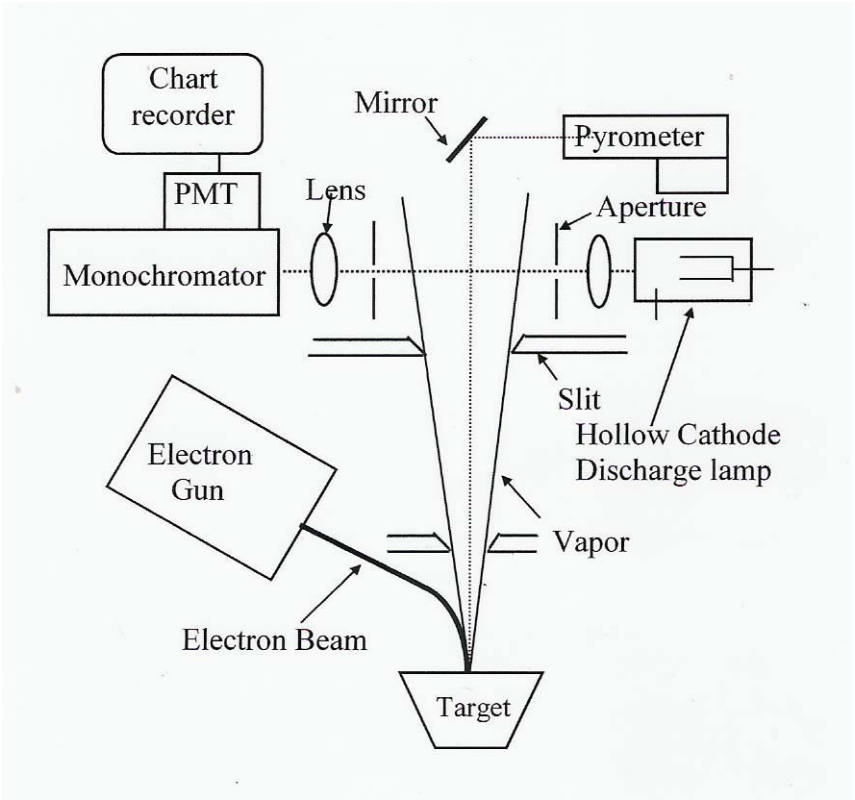

Figure 4.8 Schematic diagram of experimental set-up for monitoring of atom density by absorption spectroscopy

The atom density was calculated from the ratio of transmitted signal to the incident signal by applying Lambert-Beer's Law and using the broad band cross section [59-60] assuming Doppler broadening dominates both within the source and the absorber.

Mathematically, $I_t / I_0 = e^{-n\sigma l}$ (4.8)

where, I_t = Transmitted light intensity,

I_0 = Incident light intensity, n = Atom density in no./cc, l = Thickness of the absorber,

σ = Broad band cross section = $2.493 \times 10^{-2} \times f / \sqrt{\Delta\nu_a^{\,2} + \Delta\nu_s^{\,2}}$

(where $\Delta\nu_a$ = Line width of Atomic beam, $\Delta\nu_s$ = Line width of source (hollow cathode),

f = Oscillator strength)

We have utilized the experimentally measured source line width at 591.5nm, for calculating the $\Delta\nu_s$ at other emission lines. From the emission line profile at 591.5nm of the HCDL as recorded by Febry-Perot interferometer, value of line width was found to be 0.9 GHz. Assuming Doppler broadening predominates inside hollow cathode, the full width at half maximum (FWHM) is given by [61],

$$\Delta\nu_s = 7.16 \times 10^{-7}\, \nu_0 \sqrt{T_e / M} \quad (4.9)$$

Now, from above expression emission temperature "T_e" of hollow cathode discharge lamp was estimated using the measured line width (0.9GHz) and then, this temperature was used for calculating the source line width '$\Delta\nu_s$' at other wavelengths.

To calculate the absorption line width "$\Delta\nu_a$" of uranium atomic beam at resonance frequencies, we have used following expression in which collimation effect [61] due to presence of the slit has been taken care of by the multiplying factor $\sin\phi$,

$$\Delta\nu_a = [\sin\phi] \times 7.16 \times 10^{-7}\, \nu_0 \sqrt{T / M}$$

where $\phi = \tan^{-1} a/b$,

('*a*' and '*b*' are the half of slit length and slit height from the e-beam spot respectively).

T = Temperature of the e-beam spot as recorded by two colour pyrometer

We calculated the cross section using the oscillator strengths as reported by Klose and Voigt [62] who had determined the "*f*" values by electronic excitation and method of delayed coincidence. Maximum error in these reported "*f*" values is 20%. We have avoided using the "*f*" values reported by Corliss et al. [63] who had determined "f" values from fluorescence intensities of arc spectra as we found numerous instances in the literature [19,64] where authors had expressed disagreement with the results derived from arc spectra.

At an e-beam power of ~6kW, absorption signals were recorded at a number of transitions to find the atom densities in ground state (0 cm^{-1}) and low-lying metastable states (620 cm^{-1} and 3800 cm^{-1}). The calculated results are given in table 1. By finding the population in a particular state using many transitions and taking their average, the scatter in calculation of atom density owing to imprecise knowledge (or error) of cross section and uncertainties of our measurements was reduced. The average values are shown in table-1. Finally, taking this average value of atom density as true value, cross section at any wavelength could be back-calculated from the experimentally recorded absorption signal.

Table-1 Atom densities in ground & metastable states of uranium at ~6kw e-beam power

State (cm^{-1})	Wavelength (nm)	Ratio (I_t / I_0)	Cross Section (10^{-13} cm^2)	Atom density (10^{10} no./cm^3)	Average Atom density (10^{10} no./cm^3)
0	591.5	0.69	7.67 (7.8 [a])	4.4	
0	436.2	0.70	7.70	4.2	4.3
0	439.3	0.75	6.33	4.1	
0	381.2	0.72	6.45	4.6	
620	400.5	0.94	3.58	1.56	
620	435.5	0.87	8.16	1.54	1.55
620	365.9	0.78	14 [a]	-	
3800	422.2	0.97	8.17	0.34	0.35
3800	383.9	0.94	15.5	0.36	

[a] Back calculated cross section taking average no. density as the true density

CHAPTER - 5

Convective heat transfer in melt pool generated by electron beam heating

5.1 A new proposition for evolution of convection in melt Pool:-

At first, we identify the mechanism of convection in a liquid metal pool generated by a concentrated energy flux hitting on the surface of a target and then, propose a model for evolution of the convection in melt pool. There may be three types of driving forces behind the convection in molten pool viz. temperature dependant surface tension (or Marangoni flow) [13-14,65-66], buoyancy due to spatial variation of density depending on temperature and finally, concavity of the melt pool due to backward pressure of the emitted vapor on the surface of the liquid.

As metals have a negative temperature coefficient of surface tension [67], the central portion of liquid on the surface has low surface tension as compared to the value at the pool boundary. So, hot fluid on the surface flows outward from the e-beam spot area as shown in figure 5.1, thereby increasing the heat loss. Again in principle, as the density decreases with temperature, the liquid at the central portion of the pool is lighter than the liquid at the pool boundary. So, due to buoyancy effect, the hot liquid on the surface flows from the center to the melt pool boundary. Thus, the combined effect of surface tension and buoyancy gives rise to a outward convective current in the molten pool from center to pool boundary. However for liquid metals, many researchers [13-14] have both experimentally and numerically proved that the contribution of buoyancy effect on the convection is negligible as compared to the surface tension effect. So in this thesis for quantitative analysis of the data, we have considered that only the surface tension effect is responsible for the outward flow in melt pool.

When the beam power is increased resulting in significant generation of metal vapor from central region of the melt pool, the emitted vapor exerts a downward pressure at the center of the target. Thus, the surface of the melt pool attains a concave shape as shown in figure 5.1-b and at very high powers a crater (or keyhole) is formed. So, liquid metal particles at the boundary tend to flow from outer region to the center by gravity and mixing of the colder fluid with the hot fluid at center occurs. However, there is a major difference of this type of flow with flow caused by surface tension. While the driving force for convection by surface tension is outward, the force due to concave surface of the fluid is inward. At lower powers, former force is dominant where as at higher powers the latter force is dominant. At some intermediate powers, the two forces may cancel each other and flow rate may attain a minimum value leading to minima in convective heat transfer.

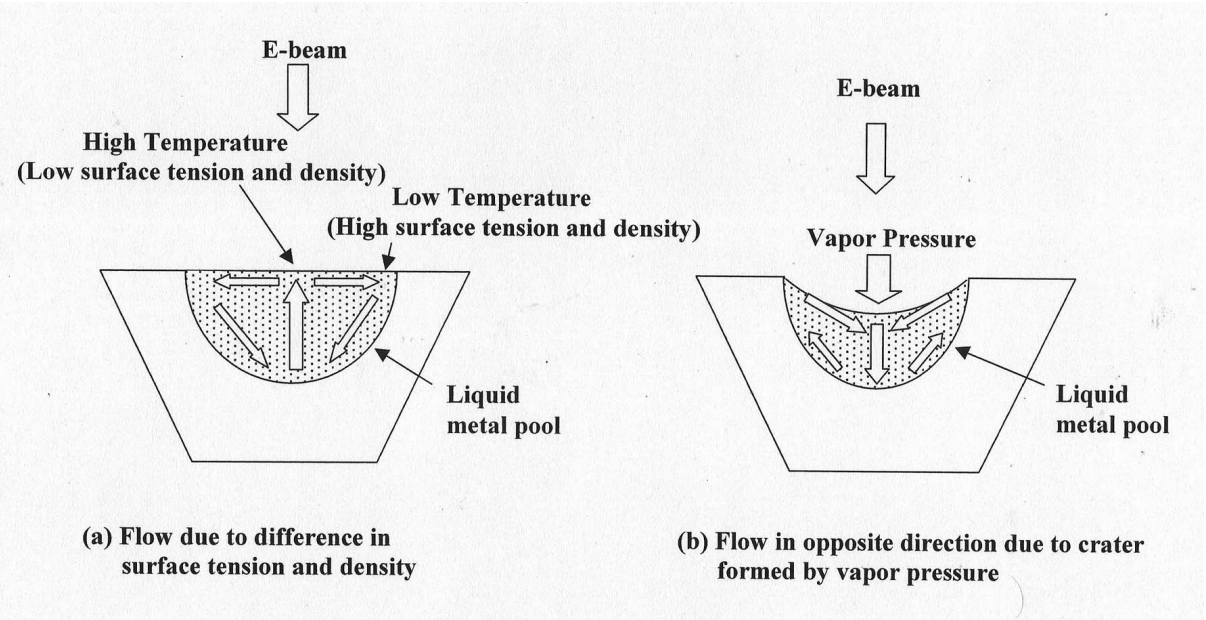

Figure 5.1 Driving forces for flow in melt pool (a) due to surface tension and density (b) due to crater generated by vapor pressure

Thus, evolution of the flow (or heat transfer) in the molten pool of metal with e-beam power can pass through the following three stages,

Stage I – Flow on the surface is *outward* and *increasing* with beam power, and it is mainly governed by surface tension forces (crater effect is negligible).

Stage II – Flow on the surface is *outward,* but *decreasing* with beam power due to gradual onset of the crater effect which opposes the flow by surface tension forces.

Stage III – Flow on the surface is *inward* and *increasing* with beam power, as it is mainly governed by crater effect (surface tension effect is negligible).

Between the stage II and III, flow reversal occurs and minima in flow rate (or heat transfer) is expected to be observed. However, to observe this point of flow reversal (and stage-III), the maximum possible of e-beam power in the experiment has to be sufficient so that surface tension forces are completely overcome by the crater effect. Similarly, in the opposite extreme, if the vapor pressure (or crater) effect is significant as compared to the surface tension forces right from the beginning of experiment (i.e. near melting point), stage-I may not be observed at all for some metals.

Therefore, experimental measurements are needed to confirm and characterize the evolution of convective heat transfer in a liquid metal pool with increase in incident power. Our experimental results and analysis on these aspects are given below.

5.2 Experiment for evaluation of Nusselt number:

The experimental system (Fig. 5.2) consists of a vacuum chamber in which background pressure is maintained at a level ~10^{-5} mbar throughout the process. A transverse e-gun (10 kV, 0.8 A) was used to bombard the metal target placed in a water-cooled copper crucible. Due to the presence of the water-cooled crucible, the outer portion of the target remains solid and acts as a skull surrounding the liquid metal pool at the center. However, the

inside surface of the crucible is corrugated for having minimal surface contact with the metal target. The e-beam spot on the target is an elliptical area of ~7 mm × 5 mm. The temperature steeply decreases from ~2500K at the e-beam spot area to melting point of the target material at the melt pool boundary. As the vapor pressure is a sensitive function of the temperature, evaporation of the metal occurs mainly from the center of the melt pool.

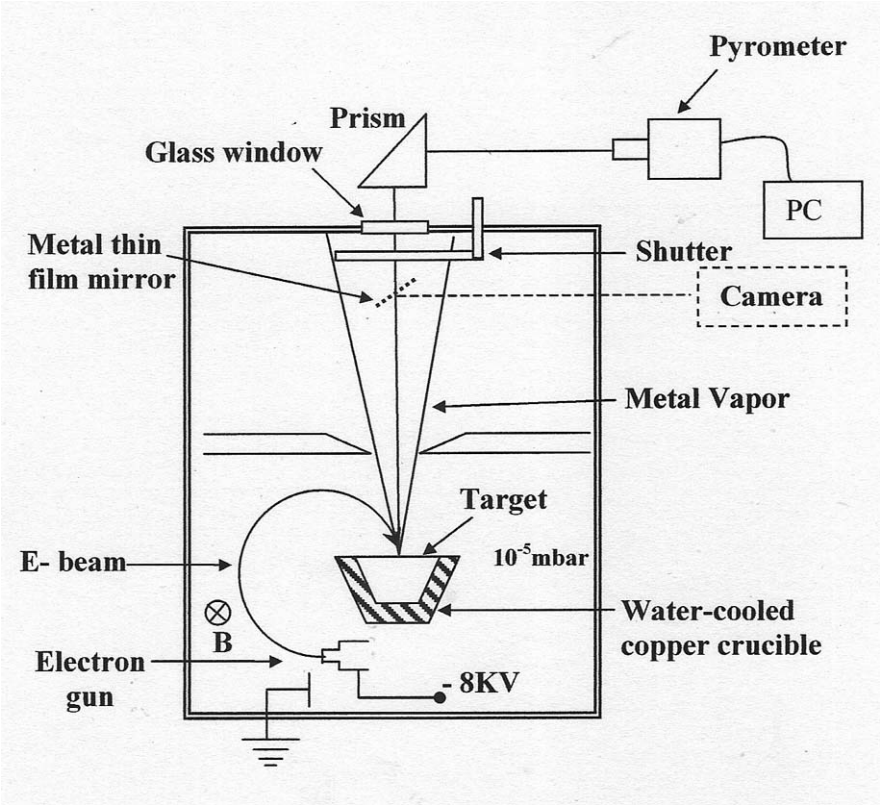

Figure 5.2 Experimental set-up for monitoring of thermal parameters for evaluation of Nusselt number

The temperature of the center of melt pool was measured by a TCP (Model PZ40, Keller GMBH, Germany) and a quartz prism turned the light coming from the hot zone towards the pyrometer. The shutter just before the vacuum glass window was opened for few seconds and the digital signal of the temperature coming from the pyrometer was recorded in a computer. We have avoided the use of periscopic mirror formed by deposition of metal vapor on an inclined glass for temperature measurement due to its dynamically changing spectral

reflectivity. Details of these uncertainties are given in earlier section. However to measure the area of melt pool, photograph of the target was taken by a digital camera using the periscopic mirror. From the photograph, the area of the melt pool could be determined by drawing a polygon along the periphery of melt zone offline after the experiment. Thus, measurement of the center temperature of target and area of melt pool at different e-beam powers was carried out for different metals viz. Al, Cu and Zr. These results are given in Figs. 5.3, 5.4 and 5.5. The bars shown in Figs. 5.3 and 5.4 are the transient fluctuations in temperature as recorded online by the computer (these are not errors of measurement). These fluctuations may be due to instability of flow inside the melt pool.

The physical reason for observation of significantly high temperature in case of Zr in Fig. 5.4 may be as follows. Because of the very low thermal conductivity of Zr as compared to Al and Cu (less by an order of magnitude), temperature gradient in the solid part of target is higher for transfer of same amount of heat by conduction. Since the temperature at the crucible boundary is clamped by cooling water, the temperature as we go towards the center increases sharply. Thus, highest temperature is obtained with Zr as target material.

Regarding melt pool area in Fig. 5.5, the pool area at any beam power depends upon both thermal conductivity (k) and melting point (T_m) of the material. This is due to the fact that slope of the temperature profile in solid part of the target is decided by thermal conductivity and melt pool boundary is positioned where temperature equals the melting point of material. Thus, the requirements for a large melt pool are lower thermal conductivity and also lower melting point. Experimental observation of decreasing order of the area of the melt pool for Zr (k = 22.6 $W.m^{-1}K^{-1}$, T_m =1852^{0}C), Al (k=238 $W.m^{-1}K^{-1}$, T_m =660^{0}C) and Cu (k=397 $W.m^{-1}K^{-1}$, T_m =1084^{0}C) in Fig. 5 indicates that thermal conductivity, which decides the spatial temperature profile, is the most dominant factor in deciding the melt pool size.

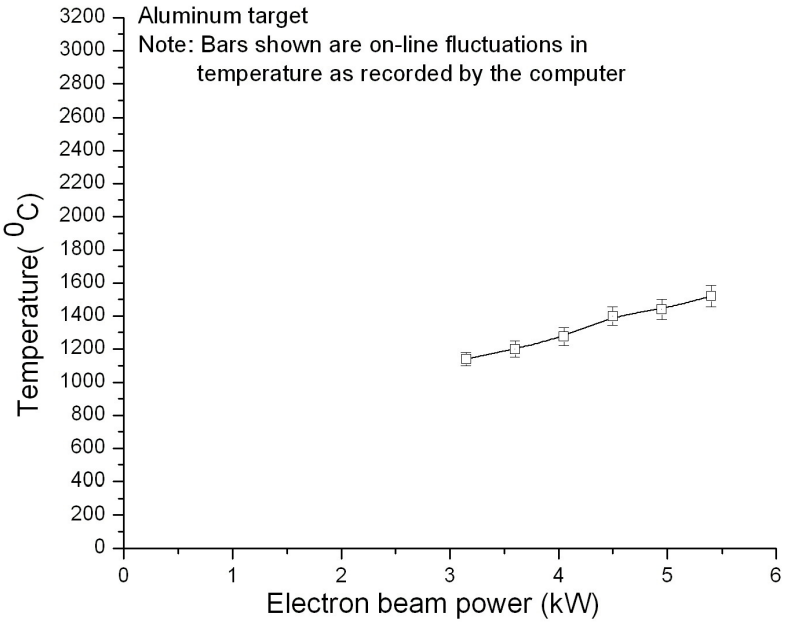

Figure 5.3 Experimentally measured temperature at the center of melt pool as a function of e-beam power for Al target

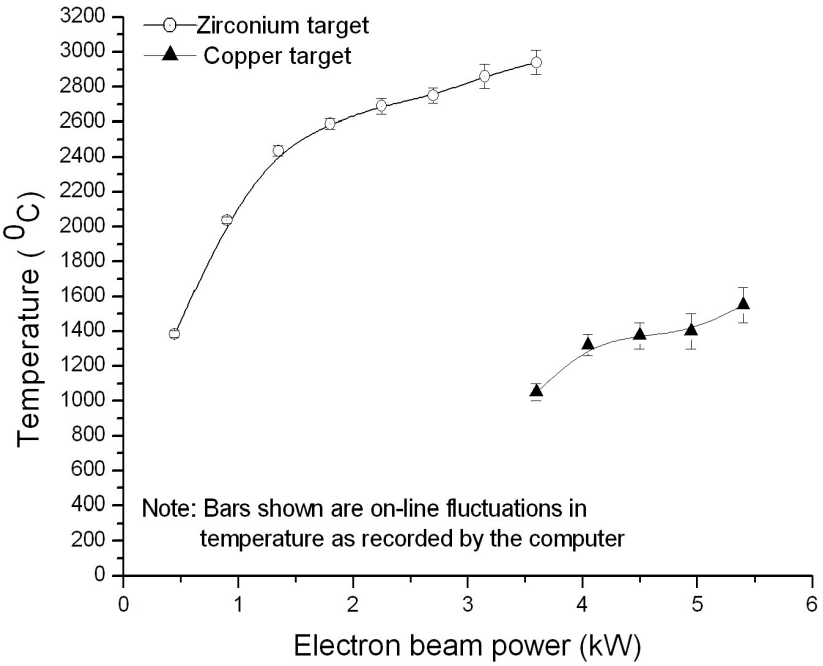

Figure 5.4 Experimentally measured temperature at the center of melt pool as a function of e-beam power for Cu and Zr targets

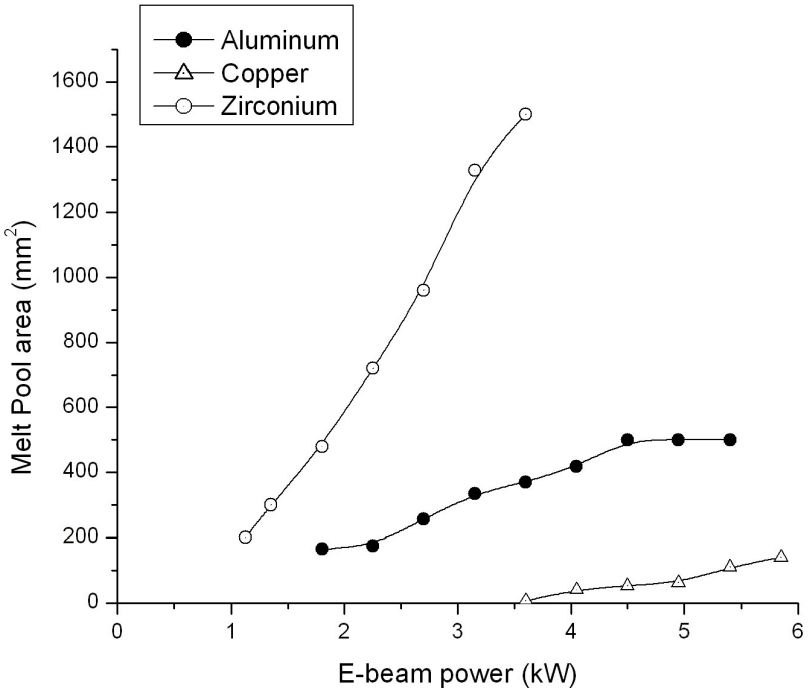

Figure 5.5 Experimentally measured top surface area of the melt pool as a function of e-beam power for Al, Cu and Zr targets

5.3 Calculation of Nusselt Number (N_u) From Experimental Data:-

Next, we determined the Nusselt Number which represents the convective heat transfer in a fluid from the observed experimental data. By definition [14], Nusselt Number (N_u) is given by,

$$N_u = \frac{\text{Total heat transfer (Q) in fluid including convection}}{\text{Conductive heat transfer } (Q_c) \text{ required to maintain same temperature difference in stagnant fluid}} \quad (5.1)$$

If Q_i is the value of incident e-beam power in experiment, numerator in Eq. (5.1) i.e. total heat transfer in the fluid can be calculated by,

$$Q = (1-\alpha)Q_i \quad (5.2)$$

Where α is the fraction (40-50%) of the incident power reflected from the target by backscattered electrons depending upon atomic number of the target material [1]. The fraction

of total power lost from the melt pool by radiation is less [1] than 2% as the area of the hot zone is very small (~6mm diameter) and so, can be neglected in Eq. (5.2).

The denominator in Eq. (5.1) i.e. conductive heat transfer (Q_c) in a hypothetical stagnant fluid (devoid of any bulk motion) required to maintain same temperature difference between center of hot zone and melt pool boundary was calculated by feeding the experimental data of center temperature and melt pool area on top surface in a axis-symmetric thermal model of target. The procedure was as follows.

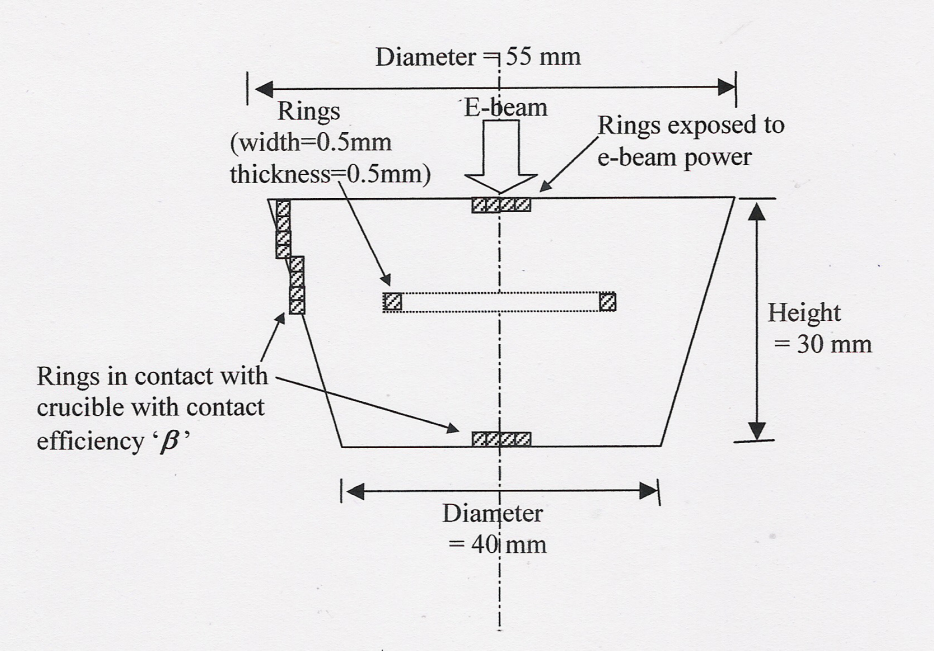

Figure 5.6 Geometrical dimensions of the target and elemental rings considered in thermal simulation of conductive heat transfer

In the first step, geometry of the solid/liquid interface was required to be calculated. It was noted that whatever heat is transferred by convection inside the melt pool, same heat is transferred by conduction from melt pool boundary to the outer surface of the solid target. So, one convenient way of finding the melt pool geometry is to solve the thermal equations in the solid part of the target only where convection is absent. For this, the target was imagined to consist of a large number of thin rings whose numbers at any plane gradually increased with

height so that it dimensionally matched with the actual target used (Fig. 5.6). The e-beam spot where power is dumped was taken to be a circle of diameter ~6mm. Due to rotational symmetry, time and resources for computation were reasonable. Steady state finite difference equations for energy balance considering conduction and radiation loss from each element were solved. Heat transfer through any ring within the target occurred by conduction where as heat transfer for a ring positioned at outer surface occurred by both conduction and radiation. If the exposed area of a ring on the outer surface of the target was '*a*' and contact efficiency between target and water-cooled copper crucible was 'β', then active area for conduction was taken as 'βa' and area for radiative heat transfer to the crucible was '$(1-\beta)a$'. In this calculation, the parameters that affected the geometry of solid/liquid interface were melting point of metal, total power transferred through solid part of target, thermal conductivity of solid target, contact efficiency between target and water cooled copper crucible 'β' and crucible temperature. Out of the above parameters, only contact efficiency between target and water-cooled copper crucible 'β' is unknown. However, as we already knew the area of the top surface of the melt pool experimentally, we set the value of contact efficiency such that area from calculation also matched with that of experiment. Thus, the contact efficiency was calculated which was found to increase with e-beam power as shown in figure 5.7. The increase may be due to thermal expansion of the target leading to better contact of target surface with the inner wall of crucible. The absolute values of contact efficiency for different materials may not be compared with each other as it depends upon the mechanical fitting of the target within the crucible which may be significantly different depending upon fabrication accuracy. Now, using the contact efficiency for a specific target at a specific power, geometry of the solid/liquid interface or depth of the melt pool with radial distance could be calculated.

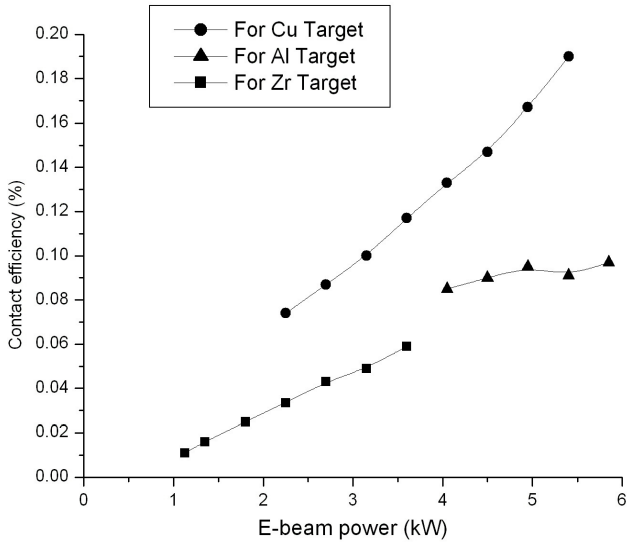

Figure 5.7 Variation of contact efficiency 'β' with e-beam power

Although the calculated temperature distribution for solid part of the target in this step was correct (and hence the position of melt pool boundary is also correct), temperature in liquid part was overestimated, as we have not considered the convective heat transfer. However, our purpose of simulating the melt pool geometry was achieved by considering conduction in the solid part. If the heat is dumped on a slightly deformed melt pool surface in a very small area and convection is assumed to be equally strong along both radius and depth with flow circulation as shown in Fig.5.1, then shape of the pool geometry will not be affected by convection in melt pool.

In the second step of calculation, temperature of all the elements at the melt pool boundary were fixed at melting point of target material thereby fixing the shape and size of the melt pool in the simulation program. Again fluid was imagined to be stagnant and heat loss could occur from each element by conduction and radiation. The conductive power was gradually increased in the simulation program and elemental temperatures up-to melt pool boundary were calculated. Only when the calculated center temperature of the hot zone was

same as the experimentally measured value, that conductive power was taken to be the required value Q_c as given in denominator of Eq-5.1. Although slight deformation of the surface of the melt pool gives rise to changes in convective flow, we are interested in calculation of conductive heat transfer (Q_c) in a hypothetical stagnant fluid as given in Eq-5.1. So, if the depth of crator is small as compared to the size of the melt pool, then thermal calculations for conduction that ignores deformation can be taken as valid.

Above procedure was followed for different e-beam powers and for each of the metals viz. Al, Cu and Zr. The Nusselt numbers thus calculated from Eq-5.1 are given in Fig.5.8 to 5.10. As this simulation program takes the experimentally measured data as its input, the output i.e. calculated Nusselt number also contains this experimental uncertainty which in our case is less than 3%. We have used temperature dependent thermal conductivity for both solid and liquid metals in our simulation program. For solid metals, temperature dependent thermal conductivity was taken from reported data [67-69]. For liquid Al and Cu, values of temperature dependent thermal conductivity were taken from Giordanengo et al [70] who have calculated k from experimental value of electrical resistivity by using Wiedemann-Franz (W-F) law as for liquid metals electronic thermal conductivity is about 99% of total thermal conductivity [70-71]. For liquid Zr, we have used the same W-F law and the reported value of electrical resisivity by Korobenko et al [71] of liquid Zr.

5.4 Discussions:

For all the metals viz. Al, Cu and Zr, it was seen from Figs. 5.8-5.10 that experimentally measured Nusselt number varies from 2.5 to 4 in the range of our e-beam power density which is normally used in e-beam evaporation of metals. As the value of N_u would have been '1' in case of pure conductive heat transfer, this proves that convective heat transfer is significant in the liquid metal pool generated by e-beam heating.

To comment on the type of flow inside the melt pool, we need to compare it with theoretically predicted value of Nusselt number for laminar and turbulent flow. According to Pumir et al. [14] if the upper surface of the melt pool is assumed perfectly flat, Nusselt number (N_u) is given by,

For laminar flow, $$N_u = Ma^{1/4}.\,Pr^{1/2} \tag{5.3}$$

For turbulent flow, $$N_u = Ma^{1/3}.\,Pr^{1/3} \tag{5.4}$$

where Ma = Marangoni Number = $\dfrac{\gamma Q \rho C_p}{\eta k^2}$ (using expression from Karcher et al [13])

Pr = Prandtl Number = $\dfrac{\eta C_p}{k}$, γ =Temperature coefficient of surface tension,

Q = Heat transferred, ρ = Density, C_p = Specific heat,

η = Dynamic viscosity, k = Thermal conductivity.

To calculate theoretical N_u from Ma and Pr at different e-beam powers using Eq. (5.3) and (5.4), temperature dependent thermo-physical properties were taken from reported values [70-72,65] and fluid temperature was taken to be the average of the experimentally measured hot zone temperature and melting point of target material. The theoretical values of N_u for both types of flow are plotted in Figs. 5.8-5.10 for comparison with experimental values and values of Ma and Pr are plotted in Figs.5.11 and 5.12.

For Al and Cu, it is clear that experimental N_u initially increases towards the value for turbulent flow with increase in e-beam power. This is expected as the force due to difference in surface tension is more at higher temperatures.

However, at 3.6kW for Al and at 5.2 kW for Cu in Figs. 5.8-5.9, N_u is found to decrease. This may be due to surface of the melt pool being made concave (or formation of a key hole) by the backward pressure of the emitted vapor which becomes more and more

significant with the increase of the temperature of the hot zone. Due to this concavity, fluid particles on the surface tend to flow inward (by gravity) against the surface tension forces and the flow which was originally due to surface tension tends to reduce ultimately decreasing the Nusselt Number. Thus, we observed the stage-I and II as explained in section-5.1 for both Al and Cu. The fact that Stage-III was not observed for Al & Cu indicates that the flow on the surface was always outward within the range of powers in our experiment. A quantitative justification for initiation of this vapor pressure effect or starting of stage–II at different e-beam powers for Al and Cu will be given in later part of this section.

For Zr in Fig. 5.10, the decreasing part of the N_u (or stage-II) starts right from the first experimental point at ~1kW indicating that effect of the depression on the surface (or keyhole) due to vapor pressure comes into play much earlier than in the case of Al and Cu. However, the direction of flow is still outward up-to 1.6kW due to surface tension and the outward flow velocity continuously decreases by concavity of surface resulting in decrease in N_u. For an e-beam power larger than 1.6kW, the depression is so deep that flow has changed its direction from outward to inward and transforms itself from stage-II to stage-III. Then, in this stage-III, inward flow rate goes on increasing with beam power ultimately resulting in increase in N_u in this region of power. Thus, we have observed the stage-II and III while evaporating Zr. The fact that Stage-I was not observed for Zr indicates that the crater effect was affecting the flow on the surface for the whole range e-beam power.

After having understood the increasing/decreasing trend of the N_u with beam power, we tried to find a quantitative reason for initiation of the stage-II (or beginning of decrease in N_u that reflects the onset of crater effect) at different powers for different metals. The depth of crater 'h' caused by vapor pressure of evaporating metal is given by,

$$h = \frac{p}{\rho g}$$

Where p = vapor pressure [67] of metal corresponding to the measured temperature of the hot zone, ρ = density and g = acceleration due to gravity

The value of h with e-beam power is plotted in Fig. 5.13 for Al, Cu and Zr. It was found that with increase in e-beam power, depression on the surface of the melt pool of Zr occurs much earlier than that for Al and that for Al occurs earlier than that for Cu. This explains the initiation of stage-II (or decreasing N_u) in Figs. 5.8-5.10 at less than 1 kW for Zr, at 3.6kW for Al and at 5.2kW for Cu. Absence of stage-I (where crater effect is negligible) in case of Zr in contrast to the case of Al and Cu is also due to the fact that h is more important for Zr than for other two metals.

The fact that experimental Nusselt number (N_u) curve for Zr is more close to the theoretical value of N_u for laminar flow as compared to the cases for Al and Cu can be understood from the following. There may be two reasons for this. First is the crater effect. The crater effect is most dominant in case of Zr, as for same e-beam power estimated crater depth for Zr is more than that of Al and Cu by an order of magnitude (Fig. 5.13). So, the flow which is originally outward due to surface tension can become inward by the crater effect and we have in fact observed the point of flow reversal in case of Zr (see Fig. 5.10). Thus, the velocity of fluid must be minimum during flow reversal and consequently, experimental N_u must touch the theoretical value of N_u for laminar flow. The small discrepancy observed at the point of flow reversal in Fig. 5.10 may be due to experimental inaccuracy or may be due to invalid assumption of perfectly flat surface in theoretical prediction of N_u for laminar flow or the flow reversal might not be global i.e. simultaneously occurring in all parts of the melt pool. Other reason for the measured N_u being significantly above the theoretically predicted value for steady laminar flow in case of Cu (and not in case of Zr) may be the instability of flow that causes enhanced heat transfer. This is confirmed by the fact that maximum fluctuation in temperature in percentage was observed in case of Cu and fluctuation in case of

Zr was minimum indicating higher instability in the melt pool of Cu as compared to Zr. Consequently, the experimental value of the Nusselt number for Cu is much above the laminar value and for Zr experimental N_u is close to laminar value.

Lastly, as we found that effect of the crater was significant enough in deciding the dynamics of flow in the molten pool of metals and consequently evolution of the convective heat transfer, it was concluded that assumption of perfectly flat surface by Pumir et al [14] was in fact an important limitation of their theory.

5.5 Conclusions:

In the study undertaken by us, a novel model is first proposed for evolution of convection in melt pool as a function of e-beam power considering all the driving forces. Then, we took our experimental results, which after feeding into a numerical thermal model, helped us in inferring the magnitude of convective heat transfer in liquid metal pool while evaporating Al, Cu and Zr targets. The procedure for estimation of the key parameter in convective heat transfer i.e. Nusselt number is outlined in detail. Experimentally observed evolution of Nusselt number with e-beam power is plotted. This experimental value is compared with the theoretically predicted values of Pumir et al [14] to test the validity of assumptions behind their theory and to know about the type of flow in the melt pool. Finally, roles of surface tension and curvature of the evaporating surface caused by back-pressure of the emitted vapor on the evolution of convective heat transfer in melt pool were identified for different metals and physical picture of the fluid flow in melt pool was inferred.

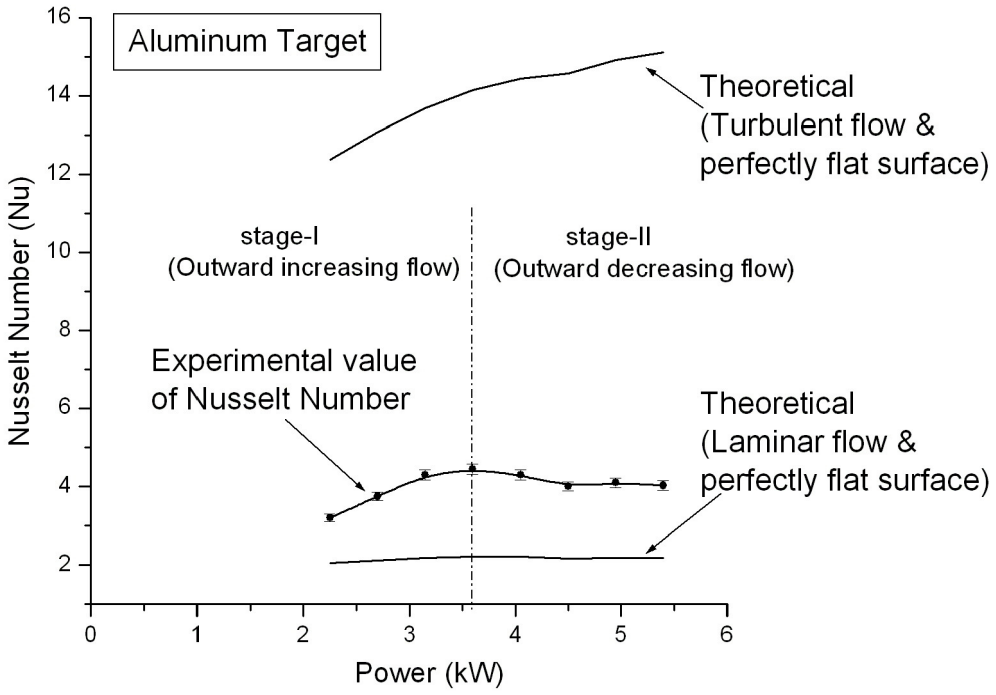

Figure 5.8 Experimental and Theoretical Nusselt number for Al target

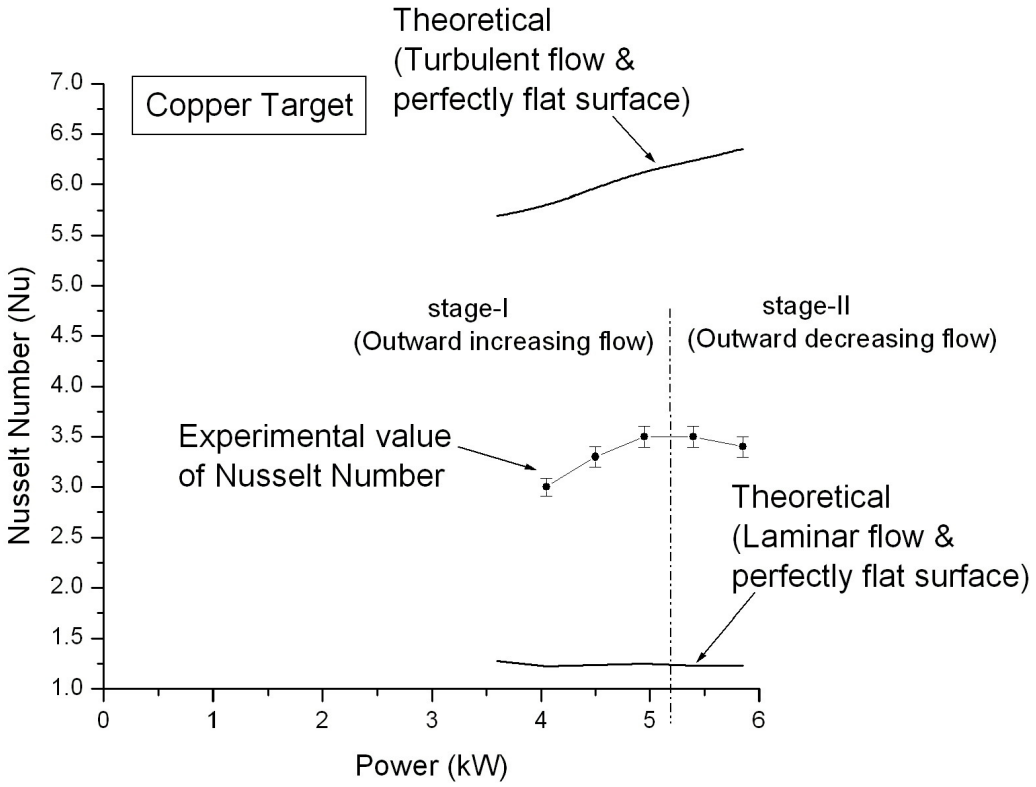

Figure 5.9 Experimental and Theoretical Nusselt number for Cu target

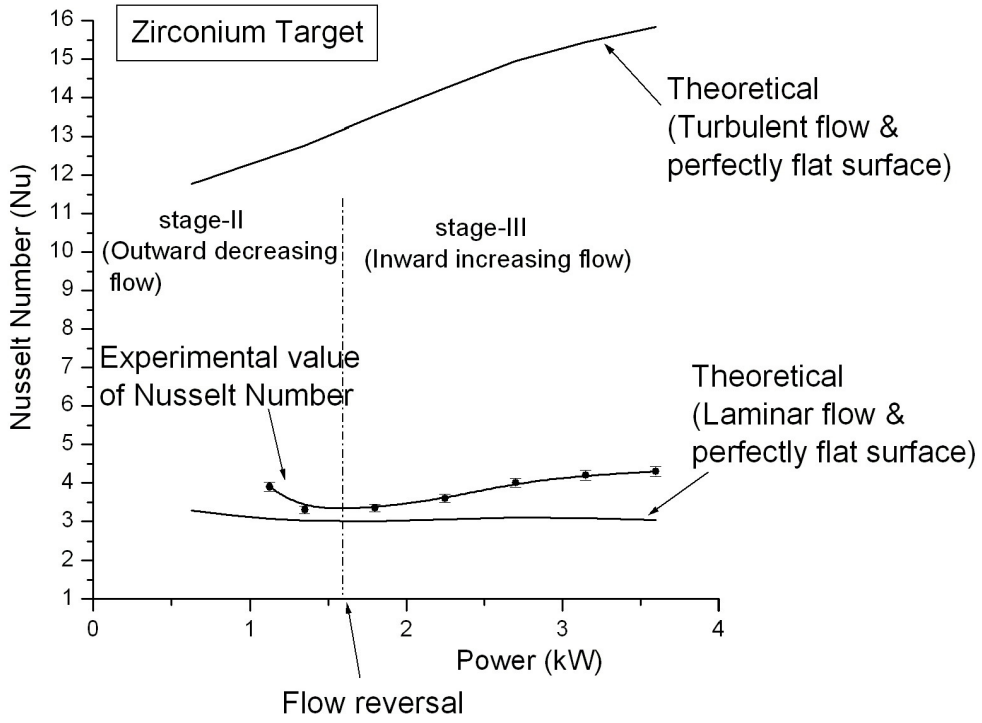

Figure 5.10 Experimental and Theoretical Nusselt number for Zr target

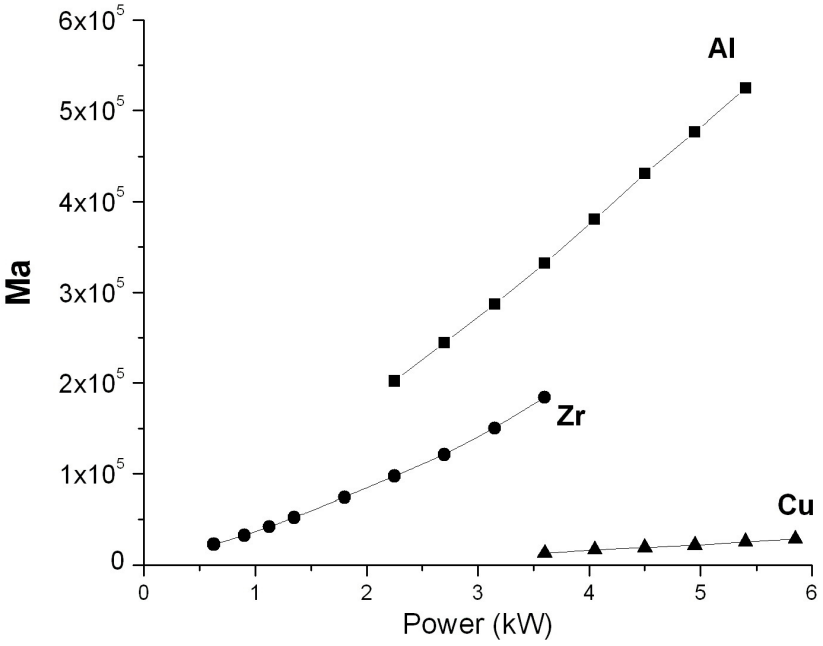

Figure 5.11 Variation of Marangoni number with e-beam power

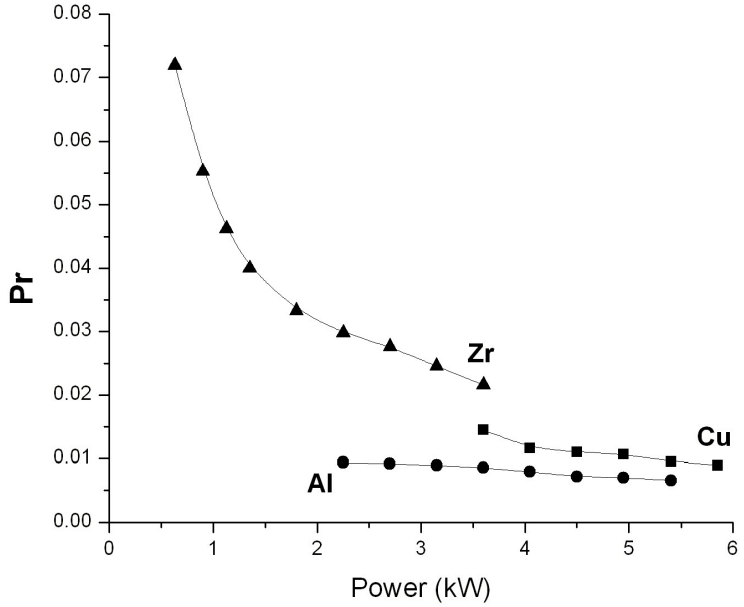

Figure 5.12 Variation of Prandtl number with e-beam power

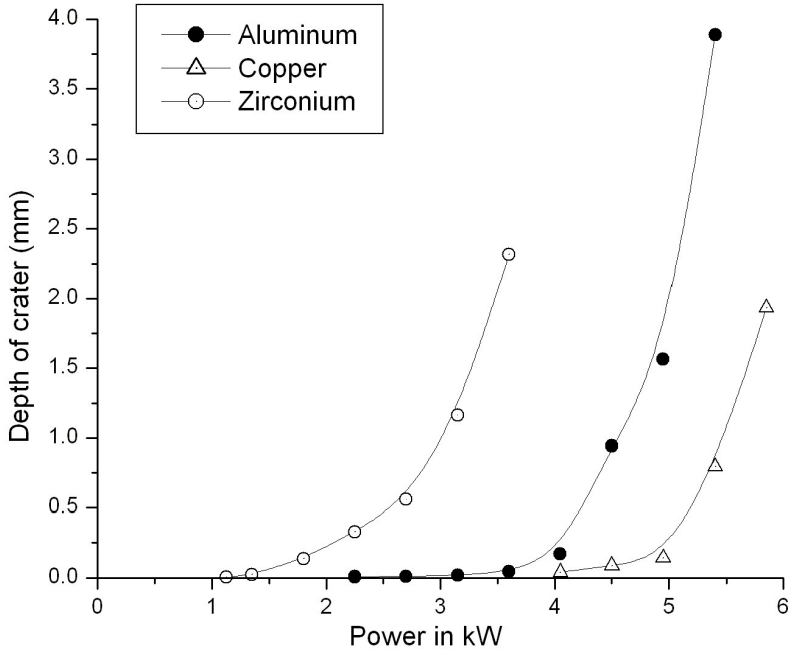

Figure 5.13 Estimated depth of crater with e-beam power for different metals calculated from measured temperature and vapor pressure data

CHAPTER - 6

Collisional effects on excitation temperature of the vapor generated by electron beam heating

In atomic vapor generated by e-beam heating, excitation temperature of the vapor is normally different from the source temperature due to collision phenomena that occur during the expansion of vapor from the hot zone along with the process generated plasma. Quantitative expressions are derived to estimate the effect of atom-atom and atom-electron collisions on the excitation temperature of uranium vapor at different source temperatures. This is compared with the experimental data recorded by spectroscopic absorption technique using a hollow cathode discharge lamp and dominance of each type of collision on the cooling/heating of the vapor is quantified.

6.1 Experimental measurement of excitation temperature

The experimental system used in this study is explained in section 4.2.2 and set-up is given in figure 4.8. A pierce-type e-gun of 8 kW capacity (32 kV, 250 mA) is mounted on the vacuum chamber at an angle of 45 degrees with the horizontal. The e-beam is turned through another 45 degrees by an external magnetic field so as to ensure normal incidence of e-beam on the evaporant surface. By increasing the e-beam power, very high temperature is generated at the e-beam impact point giving rise to copious evaporation of the target material from surface. In this study, uranium block has been used as target of the e-beam. Uranium vapor was allowed to expand freely up-to a distance of ~30cm. The vapor was collimated through two slits (1 cm × 10 cm) located at heights ~10cm and ~25cm from the source to create a vapor column in which spectroscopic investigations were carried out. The atom density was calculated from the ratio of transmitted signal to the incident signal by applying Lambert-

Beer's Law as explained in section 4.2.2 and cross sections were taken from table-1 in the same section.

The e-beam power was changed over a range of values from 3 kW to 6 kW, which affected the atom densities and relaxation parameters (collisions). Recording the absorption signals at 591.5nm and 365.9nm transitions at different e-beam powers, variations in excitation temperature was recorded (figure 6.2). The reason for choosing the above two transitions is their high value of absorption cross section. The excitation temperature 'T_e' of vapor at the distance of ~30cm from source was calculated on the basis of measured ratio 'R' of populations in 620 cm^{-1} and 0 cm^{-1} states by using the Boltzmann's expression,

$$R = \frac{n_{620}}{n_0} = \left(\frac{11}{13}\right) e^{-\left(\frac{893}{T_e}\right)} \tag{6.1}$$

where 'n_{620}' and 'n_0' are populations in 620cm^{-1} and 0cm^{-1} states respectively and factor (11/13) is due to difference in degeneracy.

Simultaneously, the source temperature of the e-beam spot was measured by a TCP at various e-beam powers (given in Fig. 6.1) to calculate the equilibrium population distribution in the vapor just above the source. The uncertainty in excitation temperature is shown by error bars in the graph and maximum error in vapor source temperature is less than ~20K. In addition to this, to measure the electron density in the plasma co-expanding with the vapor, a disc type Langmuir probe (diameter~7mm) was kept at a height of 30cm from the vapor source and V-I characteristics of probe was recorded at ~5kW e-beam power (figure 6.2). Based on the method described in reference [73], the value of ionization yield 'α' was calculated and found to be ~ 0.3%.

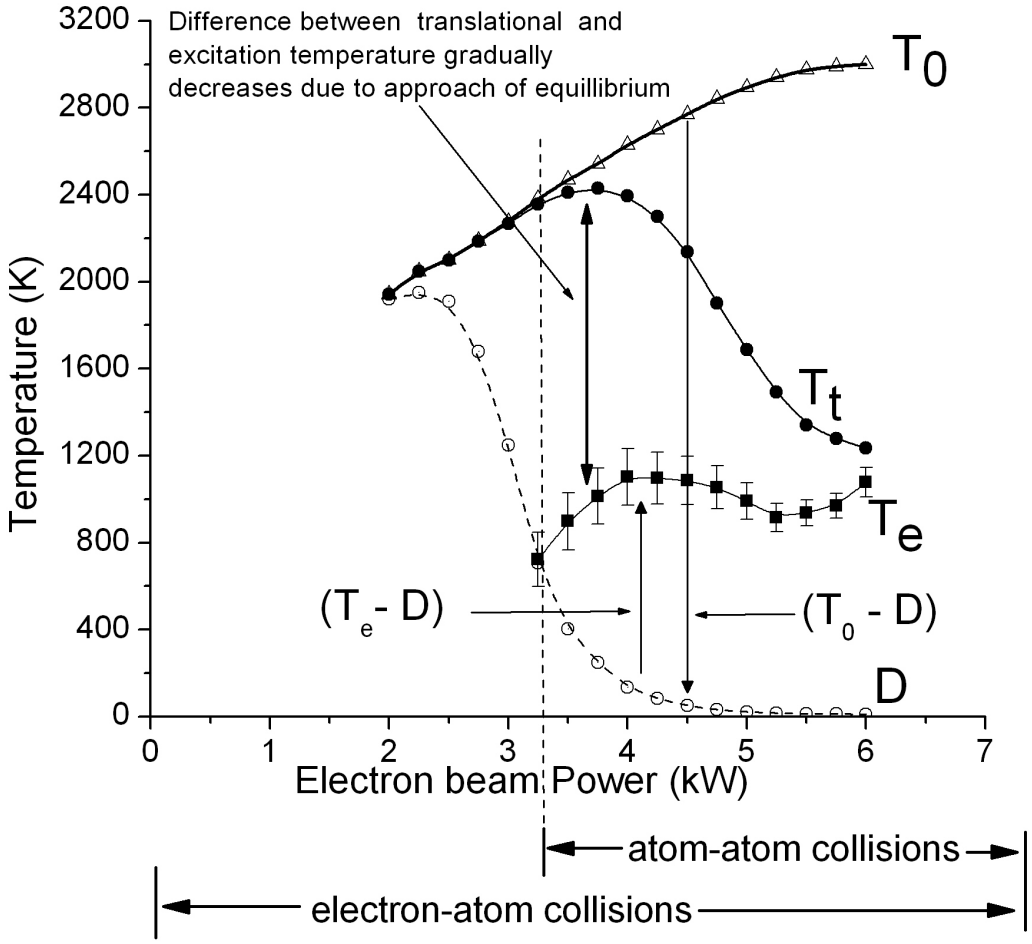

T_0 —△— Experimentally observed Source temperature

T_t —●— Translational temperature of atoms after cooling by adiabatic expansion
(Same as equilibrium excitation temperature if ONLY atom-atom collisions exist)

T_e —■— Experimentally observed excitation temperature

D -⊖- Excitation temperature if cooled ONLY by electrons assuming $\sigma = 10^{-14} cm^2$

(T_0 - D) : Cooling by low energy Plasma electrons

(T_e - D) : Heating due to coupling with translational temperature

Figure 6.1 Variation of Excitation, Translational and Source Temperature with e-beam power

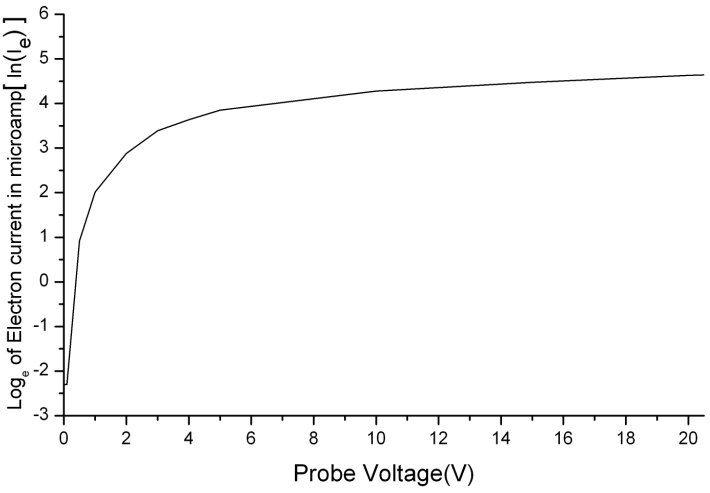

Figure 6.2 V-I characteristics of Disc type Langmuir Probe in plasma co-expanding with vapor

6.2 Theory for collisional effects on excitation temperature of atomic vapor:

The excitation temperature of the vapor after free expansion from the source is expected to be different from the source temperature due to atom-atom and electron-atom collisions.

The mechanism of the atom-atom collisional effect can be understood as follows. Initially just above the melt pool created by the e-beam, the translational (or kinetic) temperature and excitation temperature of the atomic vapor are the same as the source temperature. But, during adiabatic free expansion of the vapor, translational temperature decreases due to atom-atom collisions which reduce the velocity spread among the atoms and increase the bulk velocity of vapor. The translational temperature 'T_t' of the vapor may be calculated by using the reference [74] i.e.

$$T_t = \frac{T_0}{1+(\gamma-1)M^2/2} \tag{6.2}$$

Where, γ = Ratio of specific heats (C_p/C_v), M= Mach number= $K\,K_n^{-\beta}$

and K_n= Knudsen number

The values of constants 'γ', 'K' and 'β' are 5/3, 0.527 and 0.545 respectively for an ideal mono-atomic gas [74].

In addition to this, atom-atom collisions also tend to establish equilibrium between the translational temperature and excitation temperature of the vapor. If excitation temperature is more than the translational temperature (which is normally the case), just after the onset of atom-atom collisions, excitational cooling of the vapor will occur so that former approaches the latter. In the opposite case, if due to certain reasons such as presence of a plasma in the vapor, the excitation temperature is already far below than the translational temperature before onset of atom-atom collisions in vapor, the atom-atom collisions will lead to a rise in excitation temperature so as to equalize both the temperatures.

In case of electron-atom collisions, the electrons in principle can raise (heat) or lower (cool) the population of metastable atoms by different processes as described in figure 6.3. In heating, an atom in ground state is excited to higher excited states by electron-atom collisions followed by emission of radiation and relaxation to metastable state. In case of cooling, atoms in metastable state are excited to higher excited states followed by radiation and relaxation to ground state [20]. In addition to this, atoms in metastables states can also relax to the ground state by super-elastic collisions [75-76] in which electrons colliding with the atoms directly take away the internal energy of atom without emission of any radiation.

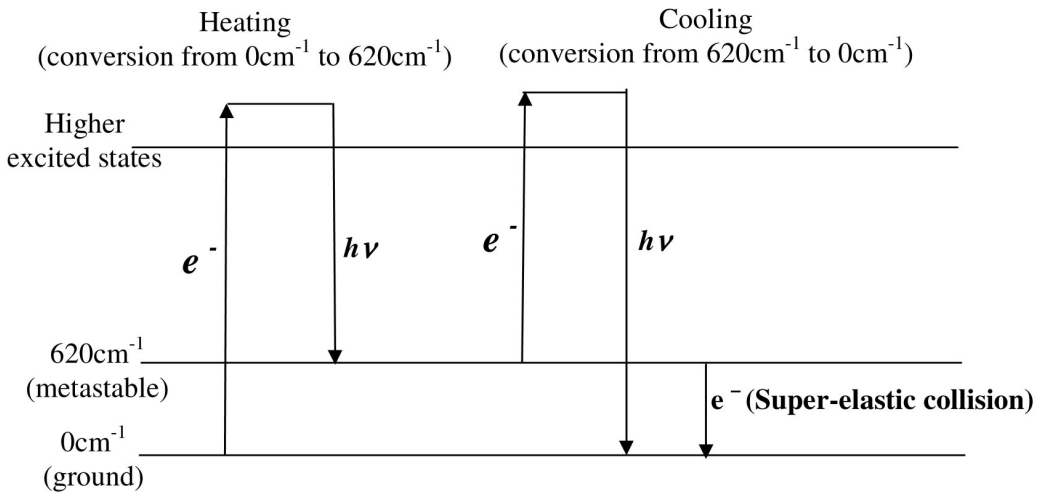

Figure 6.3 Transitions between 0 cm^{-1} and 620cm^{-1} states of uranium due to electron-atom interaction

The electrons which interact with the atoms during e-beam heating can be devided into two groups viz.

a) high energy electrons (keV to few eV) i.e. primary, backscattered and secondary electrons and
b) low energy electrons (~0.2eV) of the e-beam generated plasma co-expanding with the vapor.

It was estimated that at a typical e-beam power of ~ 4kW at 30kV, each atom is subjected to a high energy electron flux of 0.3A/cm^2 for a beam diameter of ~7mm, taking backscattered and secondary yield data from [1]. But, the low energy electron flux is ~3A/cm^2, taking atom density of uranium ~3 $\times 10^{14}$ /cm^3 near the source corresponding to the source temperature in our case, typical ionization yield [3-4] that was seen be ~0.3% in our set-up and electron temperature same as the source temperature. Thus, as the high energy electron flux is less by an order of magnitude than the low energy electron flux and its cross section for interaction is also less than that of the low energy group, we have neglected the interaction of high energy

electrons. So, in this thesis, the effect of electron-atom interaction on excitation temperature is studied by estimating the net change in ratio of population of 620cm^{-1} to 0cm^{-1} state due to interaction only with low energy plasma electrons.

Although uranium has a large number of metastable states (with decreasing populations at higher states), for the sake of simplicity, only the ground and first metastable (620 cm^{-1}) states are considered. In addition to this, since the atoms in 620 cm^{-1} state can relax to 0cm^{-1} state through both the paths viz. super-elastic collisions (whose cross section can be as high as 3×10^{-14}cm^2 [75]) and radiative processes whereas the atoms in 0cm^{-1} can be raised to 620 cm^{-1} state only through radiative process, we will neglect the rise in population of 620cm^{-1} state as compared to the decrease in population of this state due to interaction with low energy plasma electrons. Thus, in this analysis, we have idealized the system as a two state atomic system interacting with low energy electrons (0.2eV) and considered that vapor expands radially from the e-beam spot.

Let, I_0 = Rate of flow of atoms from the vapor source within a small solid angle $d\theta$,

I_{mx} = Rate of flow of meta-stable atoms at a distance of 'x' from source

within same solid angle $d\theta$,

n_e = Electron density in plasma at the distance of 'x' from source,

v_e = Average velocity of electrons, v_a = Average velocity of atoms,

σ = Net de-excitation cross section of meta-stable atom in 620cm^{-1} state for relaxation to ground state through super-elastic and indirect radiative processes due to interaction with low-energy plasma electrons,

Then, change in I_{mx} within a small distance 'dx' is given by,

$$dI_{mx} = -n_e v_e \sigma . \left(\frac{dx}{v_a} \right) . I_{mx}$$

Integrating above expression from x=0 to height 'h' when I_{mx} varies from I_{m0} to I_{mh},

$$\frac{I_{mh}}{I_{m0}} = e^{-\int_0^h \frac{n_e v_e \sigma}{v_a} dx} \tag{6.3}$$

Since, v_e and v_a correspond to same temperature (assuming plasma is in thermodynamic equilibrium with vapor source), $v_e / v_a = (m_a/m_e)^{0.5}$

where m_a and m_e are mass of the atom and electron respectively.

During e-beam evaporation of metals, the region within the e-beam spot of radius 'r' is intensely heated. So, evaporation from this region is analyzed assuming that density of atoms within the hemisphere of radius 'r' is constant 'n_{a0}' and it evolves as a point source (obeying inverse square law) outside this region. If 'α' is the ionization fraction in vapor which is normally ~0.2% to 0.5% [3-4], electron density of the plasma generated from vapor will be given by ,

$$n_e = \alpha \times n_{a0} \times (r^2 / x^2) \quad , \quad \text{for } x>r$$

$$= \alpha \times n_{a0} \quad , \quad \text{for } x<r$$

Putting above expression in equation (6.1) and then by integration we get,

or
$$\frac{I_{mh}}{I_{m0}} = e^{\sigma \alpha n_{a0} \sqrt{\frac{m_a}{m_e}}\, r\left[\frac{r}{h} - 2\right]} \tag{6.4}$$

If R_0 and R_h are the ratio of populations in 620cm^{-1} state to ground state near the vapor source and at the height 'h' respectively, then

$$R_0 = \frac{I_{m0}}{I_0 - I_{m0}} \quad \text{and} \quad R_h = \frac{I_{mh}}{I_0 - I_{mh}}$$

So,
$$\frac{I_{mh}}{I_{m0}} = \frac{R_h}{R_0}\cdot\left(\frac{1+R_0}{1+R_h}\right) \tag{6.5}$$

Comparing equation (6.4) and (6.5),

$$\frac{R_h}{R_0}\cdot\left(\frac{1+R_0}{1+R_h}\right) = e^{\sigma\alpha n_{a0}\sqrt{\frac{m_a}{m_e}}\, r\left[\frac{r}{h}-2\right]} \tag{6.6}$$

The initial value 'R_0' is given by Boltzmann equation (Eq. (6.1)) by taking excitation temperature same as the source temperature 'T_0'. Knowing the other parameters, R_h at any height can be estimated from equation (6.6). Then, putting this value of R_h again in Boltzmann equation, final excitation temperature when interaction occurs only with plasma electrons can be estimated.

6.3 Discussions

The experimentally observed excitation temperature 'T_e' calculated from the ratio of populations and source temperature 'T_0' measured by TCP as a function of e-beam power are shown in figure 6.1. We have calculated and plotted in the same figure 6.1, the translational temperature 'T_t' attained by the vapor after adiabatic free expansion in vacuum, calculated using Eq. (6.3) taking the e-beam spot size as ~7mm in diameter. For Knudsen number, atom density near the source was calculated using relation, $n=P/kT_0$, where 'P' is vapor pressure. The vapor pressure data for uranium with temperature was taken from the reports of Das et.al. [39].

It is seen that for the whole range of power, the excitation temperature T_e is lower than the translational temperature T_t of the vapor and onset of atom-atom collisions is indicated by beginning of deviation of T_t from T_0 at ~3.2kW e-beam power. So, any approach towards

equilibrium between the two temperatures T_e and T_t due atom-atom collisions which begins after 3.2kW will lead to increase in excitation temperature T_e of the vapor. In other words, atom-atom collisions in this case will cause heating of the vapor in excitation mode and whatever excitational cooling of the vapor has occurred, must have been due to electron-atom interaction. As with increase in e-beam power (or atom density), more atom-atom collisions occur, the coupling between the excitation and translational temperature becomes stronger and the difference between the two temperatures is expected to gradually decrease ultimately leading towards merging of these two temperatures with each other. This is what we experimentally observe in figure 6.1. Although the increasing part of the curve for excitation temperature with power can be clearly understood from above explanation, the region with negative slope for e-beam power between 4 kW to 5kW needs further elaboration. In this region, the translation temperature which is the very cause for rise of excitation temperature, itself falls very sharply due to free expansion. So, even if the coupling between the two temperatures becomes stronger, as the real cause of heating has become weak, the excitational heating of the vapor also drops. In other words, for power between 4 kW to 5kW, the heating is relatively less as compared to other regions in the curve and this gives rise to apparent decrease in excitation temperature with e-beam power.

We have concluded above that the electron-atom interaction was responsible for cooling of the vapor in excitation mode. These electrons are the low energy electrons of the plasma expanding with the vapor as described in previous section. For quantification of the extent of cooling by using Eq. (6.6), total de-excitation cross section 'σ' is required. However, due to lack of consistent data of 'σ' in literature [75], we used the experimentally measured value of R_h at low e-beam power to calculate the cross section. The data point at the lowest e-beam power was taken, as at this power atom-atom collisions can be neglected since translational temperature is seen to be nearly equal to source temperature (see figure 6.1).

Thus, the Eq. (6.6) can be readily applied as it considers only electron-atom collisions. The value of total de-excitation cross section by low energy electrons thus found out was $\sigma \sim 10^{-14}$ cm^2 which was of the same order as reported in reference [75]. With this value of 'σ' and R_0 as calculated from measured source temperature at different e-beam powers, R_h and then, excitation temperature 'T_e' were determined using Eq. (6.6) and Eq. (6.1) respectively when only electron-atom interaction is present. This excitation temperature is shown by curve D in figure 6.1. So, the difference between the source temperature 'T_0' and curve D in figure 6.1 represents the extent of excitational cooling of the vapor only by electron-atom interaction at different e-beam powers. The difference between the final measured excitation temperature 'T_e' and curve D in figure 6.1 represents the extent of excitational heating of the vapor due to atom-atom collisions.

Thus, we see that electron atom collisions *cools the vapor* by an amount varying between 0-3000K and atom-atom collisions *heats the vapor* by about 0-1000K depending upon e-beam power incident on the target.

6.4 Conclusions:

Excitation temperature of the metal vapor was measured and found to be much lower than both the source temperature and estimated translational temperature of the vapor. Theoretical expressions were derived to estimate the excitation temperature of the atomic vapor as affected by atom-atom and atom-electron collisions. Total de-excitation cross section for relaxation of 620 cm^{-1} state by interaction with low energy electrons could be calculated from our experimental data and it was about $\sim 10^{-14}$ cm^2. Finally using this value of cross section, extent of excitational cooling/heating by electron-atom and atom-atom collisions was estimated.

CHAPTER - 7

Spatial evolution and characterization of a two-temperature plasma generated by electron beam heating

At first, theoretical expressions for the effect of different interactions such as electron-electron coulomb collisions and electron-atom inelastic collisions on the evolution of electron temperatures of the two-temperature plasma are derived. Then, a procedure is evolved for inferring the electron temperatures of a two-temperature plasma from experimentally recorded V-I characteristics of Langmuir probe. Finally, spatial variations both from theory and experiment are compared to get an idea about the relative magnitude of the various physical processes.

7.1 Theory for evolution of electron temperature in a two-temperature plasma

Due to very high temperature of the vapor source, atoms very near to the hot zone collide with each other resulting in partial ionization of the vapor forming a weakly ionized plasma. The ionization yield due to this atom-atom collisions is given by Saha ionization equation [3] and the temperature of the electrons released in this process is normally same as the temperature of the vapor source. Another source of low energy electrons that have same temperature as the vapor source is the thermionic emission of electrons from the hot zone during e-beam evaporation. Thus, there are two sources for generation of low energy group of electrons that has a temperature of about 0.26eV (corresponding to source temperature of ~3000K).

Sources for generation of the high-energy group of electrons in the plasma are the secondary electrons emitted from the surface when the primary beam of ~9keV energy hits the target and the electrons released during impact ionization of the vapor (by collision with

the primary, backscattered and secondary electrons). The secondary electrons mentioned here include the electrons escaping from surface due to collision cascade inside the solid originated by impinging primary electrons, Auger effect and photoelectrons by absorption of bremsstrahlung x-ray [3]. Average energy of the electrons released due to both these sources varies from about ~10eV to 50eV [1, 77-81].

As the primary and backscattered electrons have energy of few tens of keV and they move in a confined circular path near the source due to magnetic field (i.e. they don't expand along with the plasma), they don't have significant effect on the evolution of the plasma although they are partially responsible for origin of this plasma. In other words, these keV electrons move as individual particles in magnetic field without being affected by its own space charge. This can be confirmed by the fact that maximum potential difference between central axis of the beam and periphery is given by,

$$\Delta V = \int_0^{r_0} E.dr = \int_0^{r_0} \left(\frac{ner}{2\varepsilon} \right).dr = \frac{ner_0^{\,2}}{4\varepsilon}$$

Where E =Electric field at any radial distance r from the axis of the beam, r_0 = radius of cross section of the primary beam

n =Electron density of primary beam (~10^9 /cm^3),

e = electronic charge, ε = permitivity of space

Putting numerical values in above equation, ΔV=41V. As this potential energy 41eV is much less than the kinetic energy (9keV) of the primary electrons, these primary electrons are not expected to be affected by the self-generated electric field. So, we will not consider them in our analysis of evolution of plasma with distance from vapor source.

Thus in the present study, the high-energy group of electrons in the expanding plasma referred here has energy of only few eV (~10 to 50eV). If distribution of electrons in this high energy group conform to Maxwell-Boltzmann statistics (which has been experimentally

verified in our case and is given in section 7.3), temperature of the group can be defined such that average energy is (3kT/2). Assumption of Maxwellian distribution for fast electrons in the expanding plasma was experimentally confirmed by the fact that Langmuir probe characteristics *ln I* vs *V* curve could be fitted with two ***straight lines*** implying Maxwellian energy distribution in each group of electrons. In addition to this, reported experimental data [77,79-80] in the literature for energy spectra of secondary electrons were found to have the shape which approximately resembles Maxwellian distribution. This is possible because just after escaping from the surface of the target (where density is highest), the electrons in the plasma may suffer numerous coulomb collisions as a result of which the distribution approaches the most probable distribution given by Maxwel-Boltzmann.

With passage of time during expansion of the plasma, the electrons in the high-energy group will loose energy to the low energy group by coulomb collisions. However, if the density of high energy group of electrons is much less than the density of low energy group of electrons, then the decrease in average energy of the electrons in high energy group will be very much significant while increase in average energy of the electrons in low energy group will be negligible. Using the expressions derived by Spitzer [82], the rate of change of temperature T_h of the high energy electrons due to coulomb collisions with low energy electrons of temperature T_l is given by,

$$\frac{dT_h}{dt} = \frac{T_l - T_h}{t_{eq}} \tag{7.1}$$

In the above expression, T_l remains almost constant for reasons stated in the above paragraph and t_{eq} (in S.I. units) is given by,

$$t_{eq} = \frac{3\sqrt{2m}(\pi k)^{3/2}\varepsilon^2}{e^4 \ln\Lambda} \times \frac{(T_l + T_h)^{\frac{3}{2}}}{n_l}$$

Where, m = mass of electron, k = Boltzmann constant,

ε = Permitivity of free space, e = charge of electron,

n_l =Low energy electron density at any distance r from vapor source,

$ln\ \Lambda$ = Coulomb integral,

$$\Lambda = \frac{\text{Debye length}}{\text{distance of closest approach}} = \sqrt{\frac{kT_l}{4\pi\, e^2 n_l}} \times \frac{4\pi\varepsilon\left[\frac{3}{2}k(T_l + T_h)\right]}{e^2}$$

As the above mentioned coulomb integral '$ln\ \Lambda$' is an extremely slowly varying function [82], it can be taken as constant during the process of establishment of thermodynamic equilibrium and its value in our case is 25 (as the measured source temperature is 3050K, So, T_l ~ 0.26eV, T_h ~20eV from literature [1,75-79] and n_l ~2.9×10^{10} /cm^3). Assuming inverse square dependency of the low energy electron density on the distance from vapor source, n_l will be given by, "$n_l = n_{l0} \times r_0^2/r^2$" where r_0 is radius of source and n_{l0} is low energy electron density at source.

Although the speed of both the groups of electrons is very much higher than the speed of ions, they are coupled to the ions due to plasma effect. Thus, electron motion is almost random while ion motion is directional so that drift velocity of the electrons is same as that of the ions which we call plasma drift velocity. The time elapsed dt for drift of the plasma through a vertical distance of dr is then given by, $dt = dr/v_i$ where v_i is ion velocity which is approximately equal to the velocity of atoms corresponding to the source temperature. This time is also same as the time available for the high-energy group of electrons to interact with the low energy electrons and atoms. Using the expressions for dt and t_{eq}, Eq. (7.1) can be rewritten as,

$$dT_h\big|_{\text{coulomb}} = \frac{e^4 \ln\Lambda\, n_{l0} r_0^2}{3\sqrt{2m}(\pi k)^{3/2}\varepsilon^2 v_i}\ \frac{T_l - T_h}{(T_l + T_h)^{3/2}}\left(\frac{dr}{r^2}\right) \qquad (7.2)$$

Now let us consider the effect of inelastic processes i.e. electron-atom collisions on the cooling of high energy group of electrons. The energy dependant excitation cross section σ can be taken as BE-scaled (Binding Energy-Excitation Energy scaled) Born cross section [83-85] given by,

$$\sigma = \sigma_{Born} \times \frac{E}{E_b + E_{th} + E}$$

(where E_b is binding energy of electron which can be taken same as ionization energy and E_{th} is the threshold energy for excitation)

or $$\sigma = \beta \frac{\ln\left(\frac{E}{E_{th}}\right)}{(E/E_{th})} \times \frac{E}{E_b + E_{th} + E}$$

(Where β is constant of proportionality for Born cross section)

Or $$\sigma = \beta E_{th} \frac{\ln\left(\frac{E}{E_{th}}\right)}{E_b + E_{th} + E} \qquad (7.3)$$

σ in Eq. (7.3) can represent the total excitation and indirect ionization cross section through auto-ionization route [86]. Although the BEB (Binary Encounter Bethe) model [87] is more appropriate for direct ionization cross section of valence electron, for simplicity, we assume that energy dependence of direct ionization is also governed by Eq. (7.3). Ionization by direct removal of core electrons is neglected as their binding energy is high [86]. Thus, σ in Eq. (7.3) finally becomes the total inelastic cross section which constitutes both excitation and ionization.

Suppose there are N number of high energy electrons of which dN electrons have energy between E and $E+dE$. The loss of total energy δE_{total} of these dN number of electrons in time dt due to inelastic collision with the neutral atoms is given by,

$$\delta E_{total} = E_{th} n_a \left(\sigma \sqrt{\frac{2E}{m}} \right) dt \; dN$$

$$= E_{th} \frac{n_{a0} r_0^2}{r^2} \left(\sigma \sqrt{\frac{2E}{m}} \right) dt \times \frac{2N}{\sqrt{\pi} (kT_h)^{3/2}} \sqrt{E} \exp(-E / kT_h) dE$$

(Assuming inverse square dependency of the atom density on the distance from vapor source and Maxwellian distribution of electrons with energy which has been experimentally verified and is given in section-7.3)

Where, n_{a0} is atom density near source and r_0 is radius of vapor source.

Above loss of energy by the electrons ultimately causes cooling of the high energy group of electrons by an amount $-dT_h$. So, for the N number electrons, we get,

$$- N \frac{3}{2} k \; dT_h = E_{th} \frac{n_{a0} r_0^2}{r^2} \left(\sqrt{\frac{2}{m}} \right) dt \times \frac{2N}{\sqrt{\pi} (kT_h)^{3/2}} \int_{E_{th}}^{\text{infinity}} \sigma \; E \exp(-E / kT_h) dE \tag{7.4}$$

Putting equation (7.3) in equation (7.4) and using $dt = dr / v_i$ as used in equation (7.2), we get

$$dT_h \big|_{\text{inelastic}} = - \frac{4\sqrt{2} \; E_{th}^2 \beta \; n_{a0} r_0^2}{3\sqrt{\pi m} \; k^{5/2} v_i} \times \frac{1}{T_h^{3/2}} \left[\int_{E_{th}}^{\text{infinity}} \frac{E \ln\left(\frac{E}{E_{th}} \right)}{E_b + E_{th} + E} \exp(-E / kT_h) dE \right] \times \left(\frac{dr}{r^2} \right) \tag{7.5}$$

If both the processes of cooling of the high energy electrons are simultaneously present in the system, net change in temperature when plasma drifts through a distance of dr is given by adding the equation (7.2) and (7.5) i.e.

$$dT_h = \left(\frac{dr}{r^2}\right)\times$$

$$\left[\begin{array}{l} \dfrac{e^4 \ln\Lambda\, n_{l0} r_0^2}{3\sqrt{2m}(\pi k)^{3/2}\varepsilon^2 v_i}\,\dfrac{T_l - T_h}{(T_l + T_h)^{3/2}} \\ \\ -\dfrac{4\sqrt{2}\; E_{th}^2 \beta\, n_{a0} r_0^2}{3\sqrt{\pi m}\; k^{5/2} v_i}\,\dfrac{1}{T_h^{3/2}}\times\left(\displaystyle\int_{E_{th}}^{\text{infinity}} \frac{E \ln\left(\dfrac{E}{E_{th}}\right)}{E_b + E_{th} + E}\exp(-E/kT_h)dE\right) \end{array}\right] \qquad (7.6)$$

Above integro-differential equation can be numerically solved to estimate the extent of cooling of the high energy electrons during expansion of the plasma along with the neutral atomic vapor.

Lastly, due to the very high mass difference between the electrons and ions, energy transfer between them by coulomb collisions will be negligible [82] during the transit time of plasma.

7.2 Experimental measurement of parameters of a two-temperature plasma

The experimental system (figure 7.1) consists of a vacuum chamber in which background pressure is maintained at a level ~10^{-5} mbar throughout the process. A transverse type e-gun (10 kV, 0.8 A) was used to bombard the Zr target placed in a water-cooled copper crucible. The e-beam spot on the target is an elliptical area of 8 mm × 5 mm. The temperature steeply decreases from the e-beam spot area towards the melt pool boundary of the target and as the vapor pressure is a very sensitive function of the temperature, evaporation of the metal occurs mainly at the e-beam spot. At the e-beam power of about ~2.7 kW, temperature of the e-beam spot at the center of target surface reached a value of ~3050 K. This temperature was measured by using a TCP (Model PZ40, Keller GMBH, Germany) and a quartz prism turned the light coming from the hot zone towards the pyrometer. The shutter just before the vacuum

glass window was opened for few seconds and the digital signal of the temperature coming from the pyrometer was recorded in a computer.

In addition to this, we installed a disc type Langmuir probe of diameter ~7mm to measure the parameters of the plasma generated during e-beam evaporation of the target. The height of the probe from the vapor source could be varied on-line from out side by using the screw-rod arrangement as shown in figure 7.1. The current was recorded by an electrometer amplifier. Thus, V-I characteristics of probe were recorded at different heights at an e-beam power of ~2.7 kW and a sample of this is given in figure 7.2a. V-I characteristics at other heights are given in figures 7.2b to 7.2c.

We have used a disc type probe (backside of which was covered with Teflon) to achieve directional similarity of charge collection all over the surface of the probe with respect to the plasma motion, which is upwards. If we had used a cylindrical probe in this flowing plasma, half surface would have been in contact with the plasma where as the shadow region would have collected the charge particles from plasma at varying distances. In addition to this, by covering the backside of disc probe, we could isolate the active surface of probe from coatings of the evaporated metal elsewhere. Material of the probe was stainless steel. As we have applied less than 5V on the probe in our experiment and ambient temperature was less than 100 ^{0}C, no secondary or thermionic effects were expected which could affect the measurements.

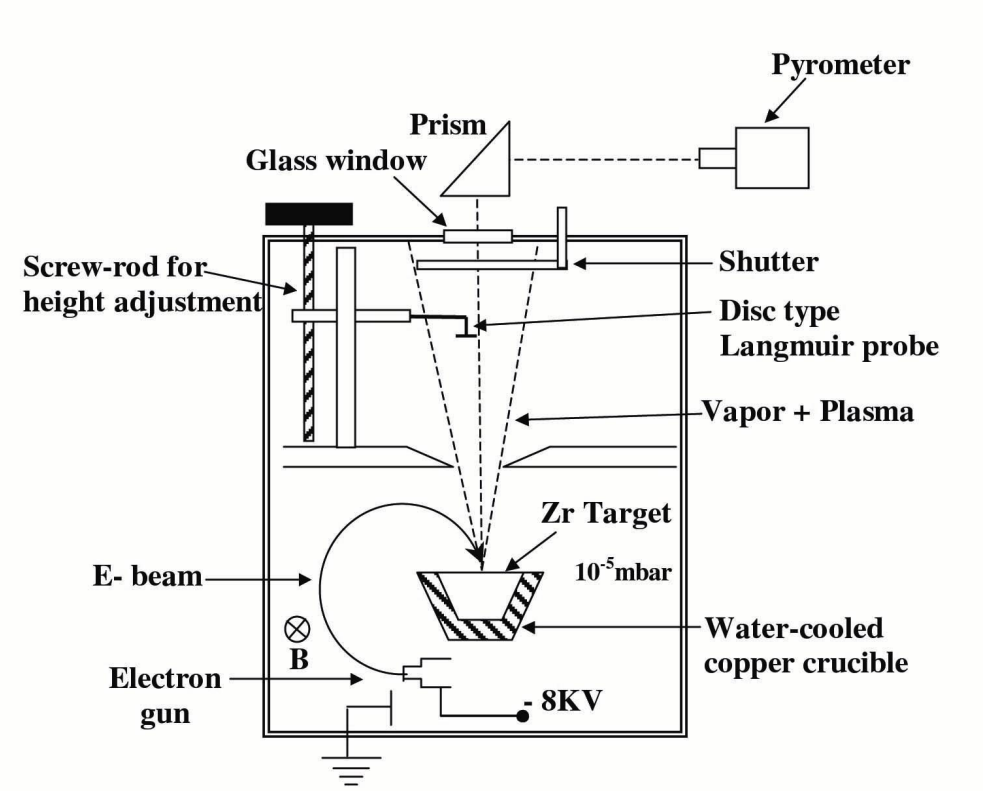

Figure 7.1 Experimental set-up for the study of evolution of two-temperature plasma

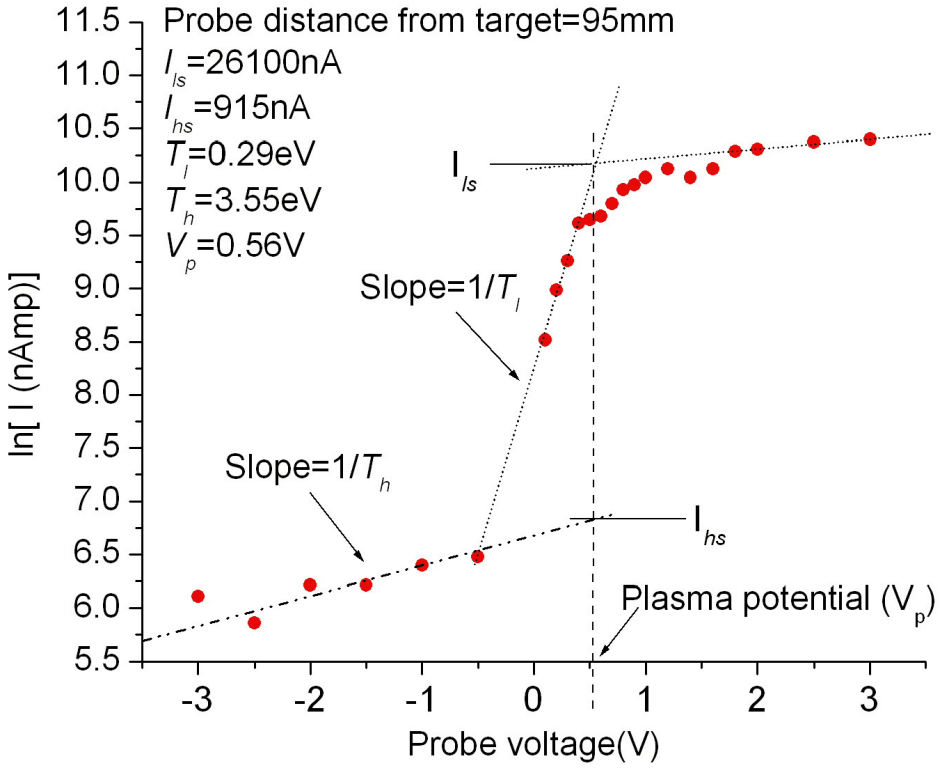

Figure 7.2a V-I characteristics of Disc type Langmuir probe at a distance of 95mm from e-beam impact point

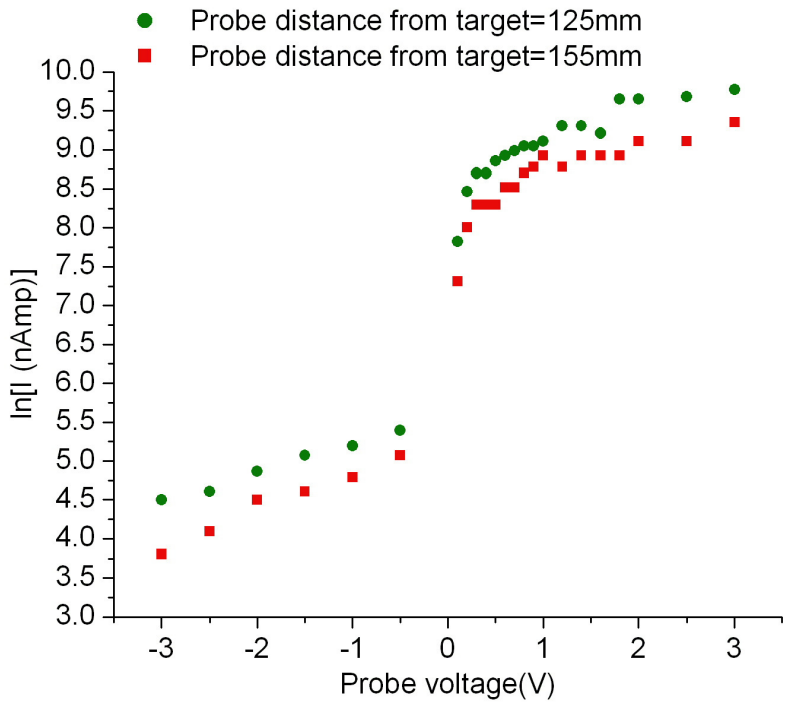

Figure 7.2b V-I characteristics of Disc type Langmuir probe at distance of 125mm and 155mm from e-beam impact point

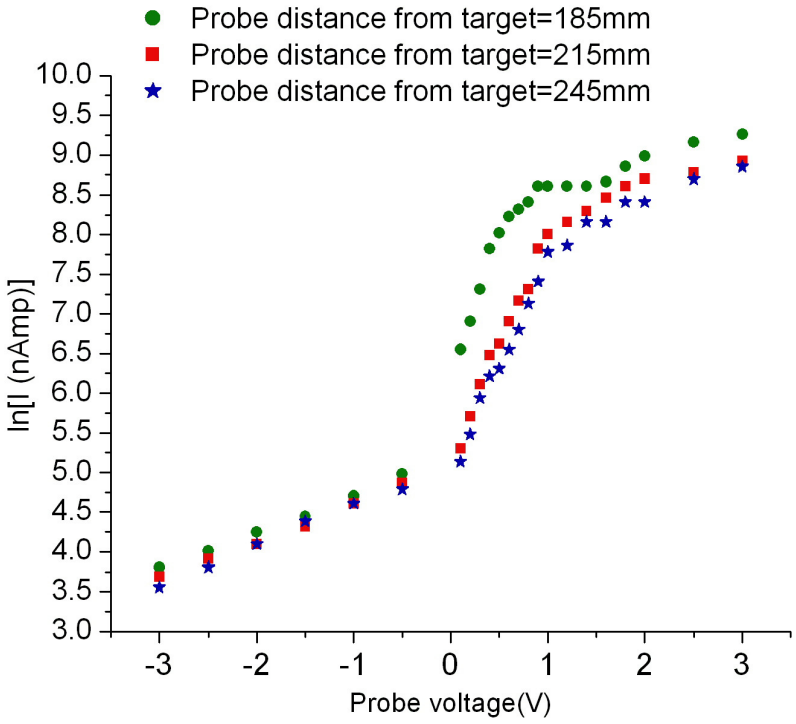

Figure 7.2c V-I characteristics of Disc type Langmuir probe at distance of 185mm, 215mm and 245mm from e-beam impact point

7.3 Results & Discussions

In the Langmuir probe characteristics, the probe current above the floating potential (i.e. when current is zero) is from the dc power supply to the probe, which we take as positive by convention. In this region, electron current is always more than the ion current so that we record a positive current. In our experiment, it was found that probe current did not change sign even if we changed the polarity of voltage and applied up to -3V on the probe (figure 7.2a). By increasing the negative bias on the probe still further during recording of figure 7.2a, floating probe potential was found to be ~ -7V. This indicated that there must be few high-energy electrons, which could not be repelled by the applied negative bias of the probe at lower magnitude of biasing voltages. Again, the probe current can be taken to comprise mainly of electron current as in our case, we have estimated ion current and found it to be less than the probe current by an order assuming quasi-neutrality of the plasma.

Within the range of floating potential and plasma space potential, the *ln I* vs *V* curve of figure 7.2a could be fitted with two straight lines of different slopes indicating that plasma consists of two groups of electrons of different energies. The fact that *ln I* vs *V* curve could be fitted with two *straight lines* also implies Maxwellian energy distribution in each group of electrons. So, each group can be represented by a temperature.

For quantitative interpretation of the experimental data, we proceed in following manner. Mathematically, electron current is given by,

$$I = I_{ls} e^{\frac{V - V_s}{T_l}} + I_{hs} e^{\frac{V - V_s}{T_h}} \qquad (7.7)$$

Where, I_{ls} & I_{hs} = Electron saturation currents due to low and high energy groups of electrons respectively

T_l & T_h = Temperatures of the low and high energy groups of electrons respectively in eV

V_s = Plasma space potential

V = Probe voltage

When V is nearly equal to or just less than V_s , exponential multiplicative factors will be nearly unity and so, the value of I will be dominated by I_{ls} and I_{hs}. Again, if the density of low energy group of electrons is much higher than the density of high energy group of electrons (which will be proved later on), then $I_{ls} >> I_{hs}$. Thus, near V_s ,

$$I \approx I_{ls} e^{\frac{V - V_s}{T_l}}$$

Or $$\ln I \approx \ln I_{ls} + \frac{V - V_s}{T_l} \qquad (7.8)$$

Thus, inverse slope of the curve *ln I* vs. *V* near V_s provides the temperature of low energy group of electrons.

However, when probe is highly negative with respect to V_s i.e. $V << V_s$, effect of the exponential factors will be significant in deciding the magnitude of 1st and 2nd terms of Eq. (7.7). As $T_l << T_h$, 1st term of Eq. (7.7) decays very fast and so, magnitude of I is decided by the 2nd term of Eq. (7.7). Thus, for the portion far from Vs,

$$I \approx I_{hs} e^{\frac{V - V_s}{T_h}}$$

$$\ln I \approx \ln I_{hs} + \frac{V - V_s}{T_h} \qquad (7.9)$$

Thus, inverse slope of the curve *ln I* vs. *V* far away from V_s (but of course above floating potential) gives us the temperature of high energy group of electrons.

Temperatures of the two groups of electrons were inferred as above from the experimental data of figure 7.2. Asymptotic straight lines when extended up-to plasma space

potential, yielded the low and high-energy electron saturation currents as is evident from Eq. (7.8) and (7.9). Finally from these saturation values, we calculated the electron density n_e using the standard formulae [21] given by,

$$I_e = n_e eA \left(\frac{kT_e}{2\pi m} \right)^{1/2} \tag{7.10}$$

where T_e = Electron temperature, I_e = Electron saturation current, A = Probe area, m = mass of electron, k = Boltzmann constant, e = charge of electron,

Above analysis was carried out for each of the six V-I characteristics recorded at different heights of the probe. The experimental values of electron temperatures and electron densities thus measured are given in figure 7.3 and 7.4 respectively.

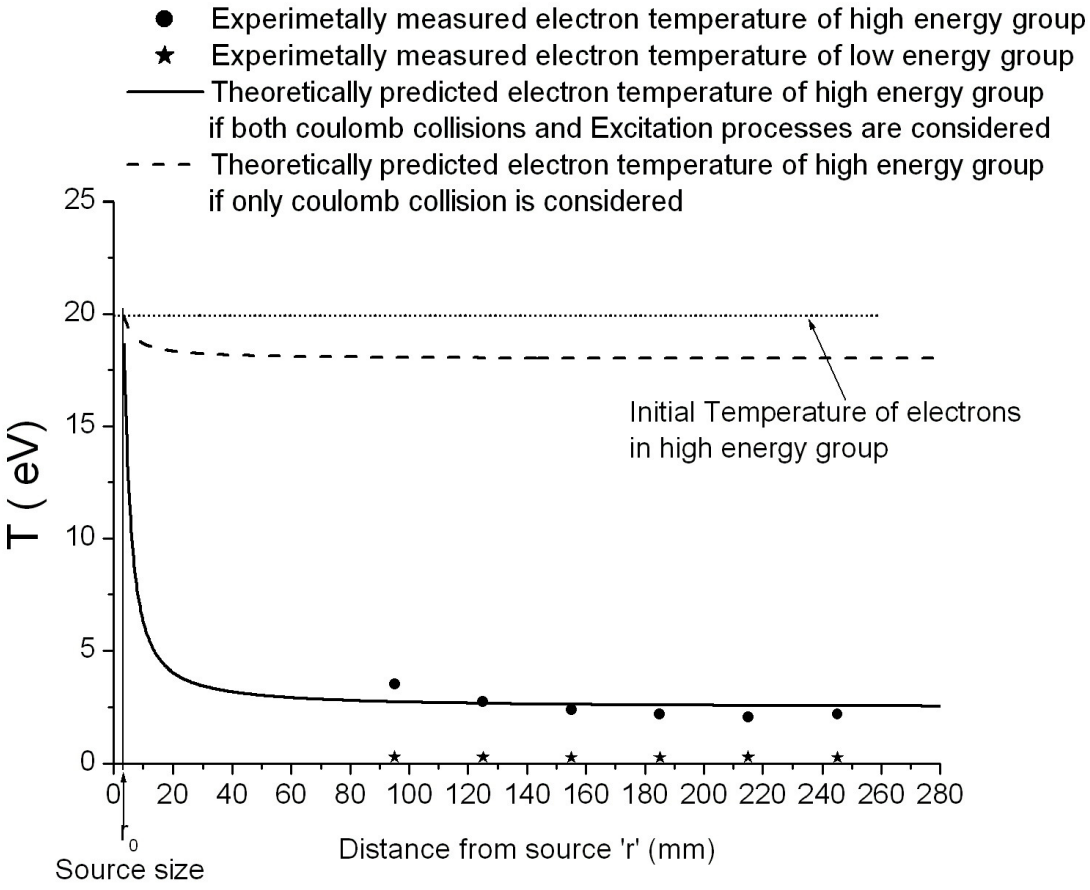

Figure 7.3 Spatial variation of electron temperature with height from vapor source

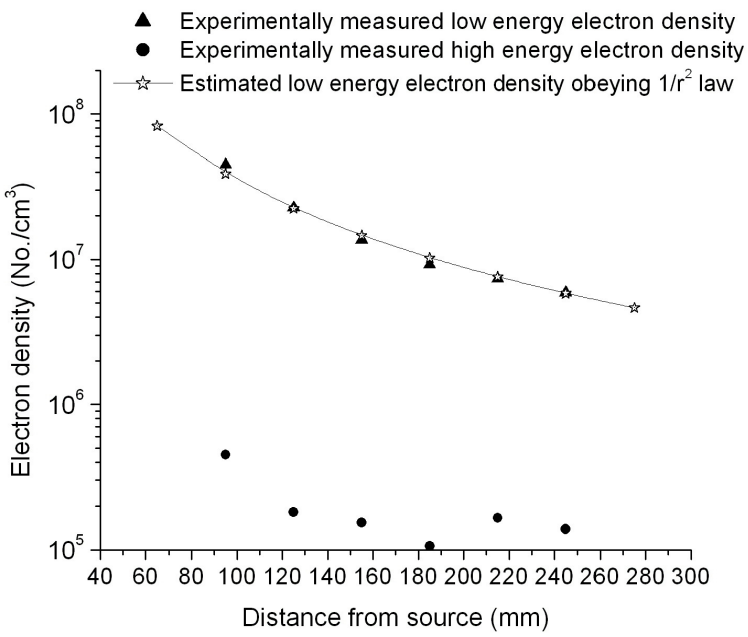

Figure 7.4 Spatial variations of electron densities of the low and high energy electrons with height from vapor source

It was not possible to use the ion current for plasma density measurement as we have to increase the negative bias on the probe beyond plasma floating potential i.e. –7V to get the ion current. At this high negative bias, significant plasma sheath appears near the probe as reported by Johnson et al. [87] and this ultimately introduces the uncertainty in area considered for ion collection. Regarding effect of directed velocity of the plasma on probe measurements, speed of electrons is higher than the speed of ions by few orders of magnitude and they are coupled to the ions due to plasma effect. So, ions have the directed velocity while directed velocity of electrons is negligible as compared to its own random motion. So, for electron current measurement, directed velocity of the plasma has negligible effect. Although ion current is affected by the directed velocity of the plasma, measurement of this ion current in our experiment was already ruled out for reasons explained before.

It is seen from figure 7.4 that high-energy electron density is less than ~1% of the low energy electron density. So, Eq. (7.2) and (7.6) can be utilized for estimation of the cooling of

high-energy electrons with distance from vapor source. The value of electron density at source n_{l0} required in Eq. (7.4) was found out by fitting the function "$n_l = n_{l0} \times r_0^2/r^2$" to low energy electron density data of figure-7.4. The value of n_{l0} thus found out was ~ 2.9×10^{10} /cm^3. The required value of atom density at source n_{a0} was found out by using the expression $n_{a0} = P/kT$, where T is temperature of the source (3050K) and P is vapor pressure at that temperature as reported in literature [88]. Initial temperature of the high energy group of electrons was taken to be 20eV (As mean energy = (3/2)×kT & mean energy is ~30eV i.e. average of lowest 10eV and highest 50eV [1,77,79-81]). In Eq. (6), threshold excitation energy was taken to be average of the excitation energy of all resonance levels as taken by other researchers [81] and it was ~3.42 eV for zirconium [89]. The constant of proportionality for Born cross section β was taken as a parameter, and it was found that for $\beta = 1.1\times 10^{-16}$ cm^2, the theoretically predicted spatial variation of the temperature of high energy group of electrons agreed well with the experimentally observed values. Taking this value for β, peak value of total inelastic cross section was found to be, $\sigma_p = 2.2\times 10^{-17}$ cm^2 . Although the instances of experimental value of σ_p for Zirconium could not be found in literature for comparison, we have compared the order of it with the orders of peak cross sections reported for various other elements [90-93]. The order of cross section was in good agreement with the reported values.

Finally, spatial variation of the electron temperature of high energy group was plotted in figure 7.3 using Eq. (7.2) in which only coulomb collisions are considered so that it can be compared with the plot of Eq. (7.6) where both coulomb and inelastic electron-atom interaction are considered. It was found that electron-electron coulomb collisions are responsible for about ~10% reduction of temperature where as rest 90% cooling was due to inelastic processes.

7.4 Conclusions

Theoretical treatment for estimation of the effect of electron-electron coulomb collisions and electron-atom inelastic processes on the evolution of electron temperatures of the two-temperature plasma generated during e-beam evaporation has been developed. A method to quantitatively interpret plasma parameters from the Langmuir V-I characteristics of a non-equilibrium plasma is given and then, it has been applied to study the experimentally observed data of zirconium plasma generated by e-beam heating. Evolution of the electron temperature with distance from the source both from theory and that observed in experiment are compared. Taking the initial temperature of the plasma at the source of vapor, total cross section for electron-atom inelastic processes could be calculated, the order of which agreed well with the reported values. Finally, contributions of each type of interaction (electron-electron and electron-atom) on the cooling of high temperature group of electrons in plasma were quantified.

CHAPTER - 8

Summary and future Directions

Summary

i - Effects of asymmetry introduced by bending and geometrical errors on the e-beam spot quality (compactness, shape and shift) have been studied by numerical simulation of the e-beam trajectory in a spatially varying magnetic field.

ii - A novel scheme for ideal distortion-less focusing of a bent non-paraxial e-beam is analytically derived. The theory is shown to be valid for any angle of bending of the beam and relativistically correct. Theoretical expressions are modified so that same principle can be used in accelerators (betatrons) where kinetic energy of the electron gradually increases during its motion.

iii - By use of theoretical calculations and experimental validations, it was established that instability of the e-gun (hysteresis) arises due to energetic metal ion bombardment on the electron-emitting area of filament in the e-gun. Finally, a practical way to check the uncontrollability arising due to bombardment of ions was experimentally demonstrated. Desirable features in a HVDC power supply circuit used in e-gun for evaporation of metals that are protected against discharges are presented.

iv - It was experimentally found that errors in temperature measured in periscopic method can be as high as 35% especially for reactive metals and it can be in both directions (positive or negative). The direction of errors could be theoretically explained. Finally, for continuous and accurate measurement of temperature of hot zone, a novel method was proposed and it was mathematically proved that this method can avoid errors experienced in the periscopic method and yet can extend the continuous monitoring time by a factor of ~1000 from few seconds to few hours. Procedure and results on the measurement of other important process

parameters viz. atomic vapor flux and (atomic) state sensitive densities by use of piezoelectric sensor and spectroscopic absorption technique respectively are presented.

v - A detailed procedure is developed to calculate the key parameter in convective heat transfer (i.e. Nusselt number 'N_u') in the melt pool generated by e-beam heating from experimental data on temperature of the e-beam spot and size of the melt pool. Then, a novel proposition was made about the evolution of convection in melt pool generated by e-beam heating with increase in e-beam power considering various driving forces for flow viz. surface tension and depression of the evaporating surface by back pressure of the emerging vapor from hot zone. This theoretical proposition could be substantiated by the experimental observations.

vi - Excitation temperature of the metal vapor was measured and found to be much lower than both the source temperature and estimated translational temperature of the vapor. Theoretical expressions were derived to estimate the excitation temperature of the atomic vapor as affected by atom-atom and atom-electron collisions. Total de-excitation cross section for relaxation of 620 cm^{-1} state by interaction with low energy electrons could be calculated from our experimental data and it was about $\sim 10^{-14}$ cm^2. Finally using this value of cross section, extent of excitational cooling/heating by electron-atom and atom-atom collisions was estimated.

viii - A procedure supported by mathematical justification is presented for inferring the electron temperatures of a two-temperature plasma from V-I characteristics of Langmuir probe. Theoretical expressions are derived for the first time to get an idea about the process of attaining thermodynamic equilibrium between two groups of electrons when such a two-temperature plasma expands along with neutral atomic vapor as in case of e-beam evaporation of metals. Theoretical and experimental results are compared.

Future Directions

For distortion-less bending of the electron beam, the theory has been elaborated in this thesis. The physical realization, that is a magnet pole face to generate radially decreasing magnetic field as given by Eq. (2.6) can be carried out. Further the effect of space charge can be taken into consideration in the theory for use in applications where e-beam needs to be focused to extremely small size. The novel method for continuous monitoring of temperature of e-beam spot proposed in this thesis may be verified by implementation of the technique. As convective heat transfer in liquid metal pool is a sensitive function of temperature dependent material properties, the experiment can be repeated in some more metals and the difference/similarities can be identified. In this thesis, we have studied only the atom density in ground and lowest metastable state (620 cm^{-1}) of uranium. However, evolution of the other metastable states with e-beam power due to atom-atom and electron-atom collisions can be studied. This will help in generation of a model that can be used to tailor the population in various metastable states. Although the theory of evolution of a plasma containing two electron temperatures generated by e-beam heating has been developed and experimentally verified in this thesis, this can be repeated for some more metals as rate of cooling of high temperature electron group strongly depends upon the total inelastic cross section for electron-atom interaction which is material dependant and the phenomena may be significantly different for different materials.

To conclude, the work discussed in the present thesis leads to several channels which if pursued can lead to further improvements in the field of Electron beam Physical Vapor Deposition.

REFERENCES

[1] Siegfried Schiller, Ullrich Heisig and Siegfried Panzer, *Electron Beam Technology*, New York: J. Wiley, 1982

[2] M S Bhatia, "Studies in High-Rate Physical Vapour Deposition", PhD Thesis, IIT Delhi, 1994

[3] Nishio R., Tuchida K., Tooma M. and Suzuki K., "Origins of charged particles in vapor generated by electron-beam evaporation", *J. Appl. Physics,* 72 (10), 4548-4555, 1992

[4] B. Dikshit and M.S. Bhatia, "Hysteresis in electron emission current of an axial electron gun used for evaporation of metals", *IEEE Transactions on Plasma Science*, 35 (2), 396-401, 2007

[5] A. B. El-Kareh and J. C.J. El-Kareh, Electron beams, lenses and optics, Academic press, London, 1970

[6] O. Klemperer, Electron optics, Cambridge University press, London, 1953

[7] P.W. Hawkes and E. Kasper, Principles of electron optics, vol-2, Academic press, London, 1989

[8] F. Schwirzke, M.P. Hallal Jr. and X.K. Maruyama, "Ion formation on the surfaces of electrodes", *Nucl. Instr. and Methods in Physics Research B*, 67, 554-559, 1992

[9] M.S. Bhatia, U.K. Chatterjee and G.L. Sharma, "A Simple Temperature Sensor for Diagnostic Use in E-Beam Evaporators", Rev. Sci. Instrum. 64(8), 1993, 2371.

[10] Thakur K B and Sahu G K , "Spatial distribution of copper vapour flux during strip electron beam evaporation",*J. Phys. D. Appl.Phys*. 35, 1812-1820, 2002

[11] Bhatia M S, Joshi A, Patel K and Chtterjee U K , "Observation of nonlinearity in e-beam evaporation from a water-cooled crucible", *J. Appl. Phys.* 66 (3), 1159-1162, 1989

[12] Hironori, Ohba and Takemasa Shibata, "Generation of vapor stream using a porous rod

in an electron beam evaporation process" *J. Vac. Sc. Technol. A* 16(3), 1247-1250, 1998

[13] Ch Karcher, R Schaller, Th Boeck, Ch Metzner, A Thess, "Turbulent heat transfer in liquid iron during electron beam evaporation", *International journal of Heat and Mass Transfer,* 43, 1759-1766, 2000

[14] Alain Pumir and Laure Blumenfeld, "Heat transport in a liquid layer locally heated on its free surface", *Physical review E*, 54 (5), R4528-R4531, 1996

[15] V. K. Mago, B. Lal, A.K. Ray, P.R.K. Rao and S.D. Sharma, "Single-color photoionization studies in uranium I" , *J. Phys. B* 20, 6531, 1987

[16] P. T. Greenland, "Laser Isotope Separation", *Contemporary Physics* 31 405, 1990

[17] P. R. K. Rao , *Current science* 85 (5), 615, 2003

[18] E.C. Jung, Kwang-Hoon Ko, S. P. Rho, C. Lim, Cheol-Jung kim, "Measurement of the populations of metastable levels in gadolinium vapor by diode laser-based UV and near-IR absorption spectroscopy", *Opt. Commun*., 212, 293, 2002

[19] A. Nishimura, H. Ohba, K. Ogura, T. Shibata, *Opt. Commun*. 110, 561, 1994

[20] Hao-Lin Chen, Ray Bedford, C. Borzileri, W. Brunner and M. Hayes, "Relaxation of neodymium in a weakly ionized expanding plasma", 1978 *J. Appl. Phys*. 49, 6136

[21] Besuelle E. and Nicolai J. P., "Study of expansion of a plasma generated by electron-beam evaporation", *J. Appl. Physics,* 84 (8), 4114- 4121, 1998

[22] S B Song, C S Chang and Duk-In Choi, "Effect of two-temperature electron distribution on the Bohm sheath criterion", *Physical Review E*, vol. 55 (1), pp. 1213-1216, 1997

[23] P Seuferling, J Vogel and C Toepffer, "Correlations in a two-temperature plasma", *Physical Review A* ,.40 (1), pp. 323-329, 1989

[24] Keiichi Nishimura, "Velocity dependence of the Coulomb logarithm and the temperature equalization of electrons and ions in a plasma", *Physical Review*, vol. 152 (1), pp. 177-

181, 1966

[25] J P Hansen and I R Mcdonald, "Thermal relaxation in a strongly coupled Two-Temperature plasma", *Physics Letters*, vol. 97A (1,2), pp. 42-44, 1983

[26] S A Mairov, "Electron Distribution function in a Two-Temperature Plasma with cold ions", *Plasma Physics Reports*, vol. 26 (10), pp. 914-916, 2000

[27] Y. Zhang, J.E. Barth and P. Kruit, *J. Vac. Sci. Technol., B* 26(2), 655-660, 2008

[28] Helmut Wiedemen, Particle accelerator physics vol. I, Springer-Verlag, Berlin, 1999, 60

[29] M Conte, "Resonant extraction from an ideal circular weak focusing synchrotron", 62 (1968), 269-275

[30] C C Iliescu, "Ideal pole faces for weak-,strong-, and FFAG-focusing particle accelerators and other nuclear instruments", Nuclear Instruments and Methods, 21 (2008), 145-154

[31] Stanley Humphries Jr., "Principles of high current electron beam acceleration", Nuclear Instruments and Methods in Physics Research A, 258 (1987), 548-565

[32] Teng Chen and Luis R Elias, "Generation of low-emittance electron beams in electrostatic accelerators for FEL applications",
Nuclear Instruments and Methods in Physics Research A, 354 (1995), 575-583

[33] Yuichiro Yamazaki, Osamu Nagano, Susumu Hashimoto, Atsushi Ando, Kazuyoshi Sugihara, Motosuke Miyoshi and Katsuya Okumura, "Electron optics using multipole lenses for a low energy electron beam direct writing system", *J. Vac. Sci. Technol.*, B 20(1), 25-30, 2002

[34] J.I.M. Botman, T. Bates and H.L. Hagedoorn, *Nucl. Instr. and Methods in Physics Research B*, 10/11, 796-798, 1985

[35] Peter T. Kirstein, Gordon S. Kino, William E. Waters, *Space-charge flow*, New York: McGraw- Hill, 1967, p 491.

[36] Hiroyuki Kawano, Seiji Matsui, Hajime Kobayashi and Yongfa Zhu, "Effective work functions for thermal positive-ionic and electronic emissions from tantalum heated in a high vacuum", *Vacuum*, 48 (7-9), 629-631, 1997

[37] Shelton, Haywood, "Thermionic Emission from a Planar Tantalum Crystal", *Physical Review*, 107, Issue 6, 1553-1557, 1957

[38] R. E. Taylor, W. D. Kimbrough and R. W. Powell, " Thermophysical properties of tantalum, tungsten, and tantalum-10 wt. per cent tungsten at high temperatures", *J. of the less-common metals*, 24, pp 369-382, 1971

[39] D. Das, S.R. Dharwadkar and M.S. Chandrasekharaiah, "Thermodynamics of liquid uranium vaporization", *J. of Nuclear Materials,* 130, p 217, 1985

[40] C.K. Birdsall and A.B. Langdon, "*Plasma Physics via Computer Simulation"*, 1st ed., New York: McGraw-Hill, 1985

[41] K. Ohya, "Comparative study of target atomic number dependence of ion induced and electron induced secondary electron emission", *Nuclear Instruments and Methods in Physics Research B*, vol. 206 , pp 52–56, 2003

[42] E. Hantzsche, "Theory of cathode spot phenomena", *Physica*, 104C, 3-16, 1981

[43] W D Westwood, N Waterhouse, P S Wilcox, "*Tantalum Thin films",* London: Academic Press, 1975

[44] P. B. Coates, "Multi-Wavelength Pyrometry", *Metrologia,* 17, 103-109, 1981

[45] Technov Ch, Mitev V A and Simeoniva D S "Measurements of the temperature profile on the surface of niobium during electron beam evaporation" *Vacuum* 44 (11-12), 1127-1129 , 1993

[46] Shankar Krishnan, J.K. Richard Weber, Collin D. Anderson and Paul C. Nordine "Spectral Emissivity and Optical Properties at λ = 632.8 nm for Liquid Uranium and Zirconium at high temperatures", *J. of Nuclear Materials* 203, 112-121, 1993

[47] C. Cagran, G. Pottlacher, "Normal spectral emissivities of liquid copper, liquid gold and liquid silver at 684.5 nm", *J. of Non-Crystalline Solids,* 353, 3582–3586, 2007

[48] Hironori Ohba and Takemasa Shibata, "Production of Stable Atomic Beam in Electron Beam Evaporation Process",*Jpn. J. Appl. Phys.* 38, 4258-4259, 1999

[49] Tsotridis G., Rother H. and Hondros E.D. , "Marangoni flow and the shapes of laser-melted Pools", *Naturwissenschaften* 76, 216-218, 1989

[50] Ch. Karcher, R Schaller, Th. Boeck, Ch. Metzner, A. Thess, "Turbulent heat transfer in liquid iron during electron beam evaporation**",**
Inter. J. Heat and Mass Transfer 43, 1759-1766, 2000

[51] (physics.nist.gov/PhysRefData/) published by NIST Physics Laboratory, USA.

[52] Jeurgens L.P.H., Lyapin A, Mittemeijer E.J. , "The mechanism of low-temperature oxidation of zirconium", *Acta Materialia* 53, 4871–4879, 2005

[53] C. J. Rosa , "Evaluation of oxidation rates for alpha zirconium", *Journal of the Less-Common Metals* 15, 35-41, 1968

[54] Tanabe T. and Tomita M , "Surface oxidation of zirconium above room temperature", *Surface Science* 222, 84-94, 1989

[55] Benka O, Steinbatz M , "Oxidation of aluminum studied by secondary electron emission", *Surface Science* 525, 207–214, 2003

[56] Popova I, Zhukov V, J.T. Yates Jr , "Comparative study of Al(1 1 1) oxidation with O_3 and O_2", *Surface Science* 518, 39–48, 2002

[57] Atkins P. W. 1998 *Physical Chemistry* (Oxford: Oxford University Press) 220, 923,925

[58] R. Arroyave, Larry Kaufman, and Thomas W. Eagar , "Thermodynamic modeling of the Zr---O system", *Calphad* 26 (1) 95-118, 2002

[59] Leon J. Radziemski, Richard W. Solarz, Jeffrey A. Paisner 1987 *Laser spectroscopy and its applications* (New York : Marcel Dekker Inc.) p 191.

[60] G. F. Kirkbright and M. Sargent, 1974 *Atomic absorption and fluorescence spectroscopy* (London : Academic Press Inc.) p 44.

[61] W. Demtroder 1998 *Laser spectroscopy* (New York : Springer-Verlag), p 69, p 519

[62] J. Z. Klose and P. A. Voight 1977 *Phys. Rev. A*, 16 (5), 2032

[63] C.H. Corliss, *J. Res. Natl. Bur. Stand. Sec-A*, 80A, No. 1, 1,(1976).

[64] M. Szynarowska and R. Papaj, *Physica Scripta* 25, 485 (1982)

[65] A Thess, D Spirn and B. Jüttner, "A two-dimensional model for slow convection at infinite Marangoni number", *J. Fluid Mech.*, 331, 283-312, 1997

[66] G. Tsotridis, H. Rother and E.D. Hondros, "Marangoni Flow and the Shapes of Laser-melted Pools", *Naturwissenschaften,* 76, 216 ,1989

[67] E. A. Brandes and G B Brook, Smithells Metals Reference Book, (Butterworth Heinemann, OXFORD) 1999

[68] J K Fink and L Leibowitz, "Thermal conductivity of zirconium", *Journal of Nuclear Materials* 226 , 44-50, 1995

[69] C C Bidwell and C L Hogan, "Thermal conductivity of Aluminum; Solid and Liquid States", *Journal of Applied Physics,* 18, 776-779, 1947

[70] B Giordanengo, N Benazzi, J Vinckel, J G Gasser, L Roubi, "Thermal conductivity of liquid metals and metallic alloys", *Journal of Non-Crystalline Solids*, 250-252, 377-383, 1999

[71] V N Korobenko and A I Savva timskii, "Temperature Dependence of the Density and Electrical Resistivity of Liquid Zirconium up to 4100 K", *High Temperature*, 39(4), 566-572, 2001

[72] P F Paradis, T Ishikawa and S Yoda, "Non-Contact Measurements of Surface Tension and Viscosity of Niobium, Zirconium, and Titanium Using an Electrostatic Levitation Furnace", *International Journal of Thermophysics*, 23 (3), 825, 2002

[73] B. Dikshit, G. R. Zende, M. S. Bhatia and B. M. Suri , "Electron beam evaporation of aluminium with a porous tantalum rod in melt pool", *J. of Phys. D: Applied Phys*. 38, 2484-2488, 2005

[74] Takashi ASANO, Naohito UETAKE and Kazumichi SUZUKI , "Mean Atomic Velocities of Uranium, Titanium and Copper during Electron Beam Evaporation" *J. of Nuclear Sc. and Tech*., 29 12, 1194-1200, 1992

[75] J.B.Hasted 1964 *Physics of Atomic Collisions* (London : Butterworth & Co. Ltd), p 464

[76] Marcus Jacka, Jennifer Kelly, Birgit Lohman and Stephen J Buckman, "Superelastic electron scattering from metastable helium**",** *J. Phys. B: At. Mol. Opt. Phys*. 28 , L361-L366, 1995

[77] E. J. Scheibner and L. N. Tharp, "Inelastic scattering of low energy electrons from surfaces", *Surface Science,* vol. 8, pp. 247-265, 1967

[78] S. Thomas and E B Pattinson, "Range of electrons and contribution of back-scattered electrons in secondary production in aluminium", *J. Phys. D: Appl. Phys*, vol. 3, pp 349-357, 1970

[79] A Hoffman and R Brener, "Origin of the extended fine structure in the secondary-electron-emission spectrum of graphite", *Physical Review B*, vol. 51(3), 1817-1822, 1995

[80] M Rosler, "First principles calculation of ion induced kinetic electron emission from nearly free-electron metals below the plasmon threshold", *Nucl. Instr. and Methods in Physics Research B*, vol. 164-165, pp. 873-878, 2000

[81] Dayashankar, "Ionization yield in Krypton due to electron impact", *Physica*, vol. 111C, pp. 134-140, 1981

[82] Lyman Spitzer Jr., *Physics of fully Ionized Gases*, New York: Interscience Publishers, John Wiley & Sons, 1962, p 135, 127

[83] J B Hasted, *Physics of Atomic Collisions,* London : Butterworths & Co., 1964, p 55-56

[84] Yong-Ki Kim, "Scaling of plane-wave Born cross sections for electron-impact excitation of neutral atoms", *Physical Review A,* vol. 64, 032713, 2001

[85] http://physics.nist.gov/PhysRefData/Ionization/intro.html (website of National Institute of Standards and Technology, USA)

[86] Young-Ki Kim and Philip M Stone, "Ionization of boron, aluminum, gallium, and indium by electron impact", *Physical Review A*, vol. 64, 052707, 2001

[87] J D Johnson and A J T Holmes, "Edge effect correction for small planar Langmuir probes", *Rev. Sci. Instrum.*,vol. 61 (10), pp 2628-2631, 1990

[88] E. A. Brandes and G. B. Brook, *Smithels metals reference book*, Oxford : Butterworth-Heinemann, 1992, p 8-55

[89] http://aphysics2.lanl.gov/cgi-bin/ION/runlanl08d.pl (website of Los Alamos National Laboratory, USA)

[90] H H Brongersma F W E Knoop, C Backx, "Total electron-impact excitation cross sections of helium", *Chemical Physics letters*, vol. 13 (1), pp 16-19, 1972

[91] D H Winicur and E L Knuth, "A method for the measurement of the electron-impact excitation cross section of argon", *Chemical physics Letters*, vol. 12 (2), pp 261-263, 1971

[92] P S Ganas, "Electron impact excitation cross sections for carbon", *Physica,* vol. 104C, pp 411-415, 1981

[93] V N Mileev, V I Safin and S I Strakhova, "Inelastic scattering of electrons from inert gas atoms in the Eikonal distorted-wave approximation", *Physics letters,* vol. 55A (6), pp 333-334, 1976